Assessing Future Sediment Dynamics under Climate and Anthropogenic Drivers in the Song Hau Distributary, Mekong Delta

F.J.C. Machielse

Delft University of Technology

Assessing Future Sediment Dynamics under Climate and Anthropogenic Drivers in the Song Hau Distributary, Mekong Delta

by

F.J.C. Machielse

in partial fulfilment of the requirements for the degree of

Master of Science
Environmental Engineering

at the Delft University of Technology,
to be defended publicly on 12 November, 2025, at 12.00 PM.

Student number:	5064872
Thesis committee:	Dr. A. Baar
	Prof. Dr. T.A. Bogaard
Project Duration:	April - November 2025
Faculty:	Faculty of Civil Engineering and Geosciences, Delft University of Technology

Cover: Google Earth satellite image of the Song Hau distributary, processed in QGIS (November 2025).

TU Delft

Preface

In this report, I present the findings of my research on the anthropogenic and climate drivers of sediment dynamics in the Song Hau distributary, located in the Vietnamese Mekong Delta. This thesis was written to conclude my Master of Science in Environmental Engineering, with a specialization in Water Resources and Regional Hydrology, at Delft University of Technology. The research was conducted as part of the Mekong Delta Living Lab, a partnership between TU Delft and institutions in Vietnam, among which the Institute of Coastal and Offshore Engineering (ICOE).

First of all, I would like to thank my supervisors, Anne Baar and Thom Bogaard, for their insightful guidance and support throughout this research. In particular, I am thankful to Anne Baar for her intensive supervision during the research period. She taught me essential modelling skills and consistently provided an approachable and supportive atmosphere. I also thank Thom Bogaard for his guidance, which encouraged me to look critically at my work and helped shape the direction of this research. I greatly appreciate his role in creating the opportunity to collaborate internationally, which enriched my experience both academically and personally.

Next to that, I would also like to express my appreciation to Hung and all colleagues at ICOE in Ho Chi Minh City. It was a great pleasure to conduct research at the institute, where I experienced not only academic support but also a warm welcome and generous care. The introduction to many aspects of Vietnam's rich culture made the two months truly memorable.

Finally, I would like to thank my family for their endless support throughout my studies, which has been crucial to my achievements. I am equally thankful to my friends for always being there to motivate me and help me unwind.

F.J.C. Machielse
Delft, November 12 2025

Abstract

Rivers play a crucial role in delivering sediment to the oceans, with deltas acting as key zones for sediment deposition that support ecosystems, human populations, agriculture, and industry. The Vietnamese Mekong Delta, one of the world's most important and densely populated river deltas, faces increasing stress as human interventions such as dam construction and sand mining disrupt natural sediment supply, intensifying subsidence, sea-level rise, and erosion. These pressures are further amplified by climate change, which contributes to extreme discharge events, saltwater intrusion, and coastal erosion. While considerable research addresses short-term changes, long-term projections remain limited. This study examines how human- and climate-driven factors shape sediment transport and bifurcation behaviour in the Song Hau distributary over 30 years, by evaluating branch flow partitioning (symmetry) and the system's ability to remain in equilibrium (stability).

A Delft3D 2D depth-averaged model, simulating both water flow and sediment movement, is used to examine how climatic and human drivers shape sediment transport and bifurcation behaviour in the tidally influenced Song Hau distributary. Scenarios of altered precipitation (AP), sea-level rise (SLR), sand mining (SM), and hydropower-induced discharge flattening (HD) reveal how changes in upstream discharge, downstream water levels, and bed lowering influence the system. The model performs well, with water flow results showing high accuracy (NSE = 0.90–0.94; RMSE = 0.07–0.21 m) and sediment transport reproduced within 10–20% of observed values, indicating good agreement with observed concentrations.

The results show that climate forcing, through altered precipitation and sea-level rise, generally reduces local extremes of sedimentation and erosion, leading to a more uniform distribution of sediment and flow across the bifurcation and faster stabilisation of sediment partitioning. Altered precipitation increases the system's export capacity, while sea-level rise increases symmetry by reducing the effect of tides on flow partitioning. This helps maintain throughflow, ensuring consistent export of water and sediment to the sea through both branches. In contrast, human interventions such as sand mining and hydropower-induced discharge flattening increase asymmetry between the Dinh An and Tran De branches. Tran De becomes more dominant in exporting water and sediment, while Dinh An is prone to extreme sedimentation near the river mouth, reducing export capacity. Sand mining has nonlinear effects, with increasing extraction rates indicating a threshold beyond which the system responds differently. Fluctuations in sediment and flow persist over time, preventing the system from reaching an unchanged sediment distribution. Discharge variability, moderated by hydropower dams, plays a key role in maintaining balanced flow and sediment distribution. Overall, climate change tends to stabilise the system, while anthropogenic interventions lead to more unpredictable outcomes, with sediment distribution being more sensitive than water flow.

The impacts of both human and climate drivers extend beyond the study area, influencing sediment export to the ocean. Ecosystems such as mangroves, which are vital for coastal protection, are highly vulnerable to sediment fluctuations. Effective regulation of human activities, including sand mining and discharge management, is crucial to maintain sediment balance and support the resilience of the delta and its ecosystems under increasing environmental pressures.

Contents

1

Introduction

1.1. Context

Rivers are the dominant suppliers of sediment to the oceans, exporting approximately 37,000 km^3 of water and 13–19 Gt of sediment annually [31, 72, 48]. A river transitions into a delta as it approaches the coast, where flow decelerates and sediment is distributed across distributary channels and the delta plain. River deltas grow when sediment delivery exceeds the combined effects of wave and tidal removal, sea-level rise, and subsidence: otherwise, they stagnate or degrade [28]. In many deltas worldwide, this sediment-supply mechanism is disrupted by human interventions, subjecting them to multiple stresses. This is particularly concerning because, although deltas cover less than 0.5% of the global land area, they sustain over 5% of the world's population through their fertile soils and their importance for agriculture and urban development [28, 73, 88].

The Vietnamese Mekong Delta reflects these global dynamics. As the world's third-largest delta and home to around 20 million people [17, 44], it is undergoing rapid environmental change driven by natural processes and human activities, leaving it increasingly vulnerable to multiple, interacting stresses. These stresses manifest in several ways. Upstream, the construction of large dams traps sediment that would otherwise replenish the delta, reducing its natural capacity to keep pace with subsidence and climate-driven sea-level rise. The annual silt and clay load has already decreased by approximately 80% compared to pre-dam conditions and is projected to decline further: from 26 ± 9 Mt/year in 2020 to just 4–8 ± 3–5 Mt/year by 2040 [21]. Within the delta, excessive sand mining deepens the channels and destabilises the riverbanks, further depleting the sediment budget. Extraction rates range between 8.5 and 58 Mm^3/year across the Vietnamese Mekong Delta [14, 85, 12, 25, 37]. Much of this activity is poorly regulated or illegal, and its impact remains largely uncertain, yet it strongly affects local conditions. At the same time, natural subsidence caused by the compaction of deposited sediments is intensified by groundwater exploitation [91], thereby accelerating the effects of climate-driven sea-level rise. Subsidence rates across the Mekong Delta are severe. At Tran De, one of the river mouths, a relative sea-level rise of 1.045 cm/yr was recorded over 2000–2024, of which 0.653 cm/yr was due to subsidence [34]. This relative sea-level rise drives saltwater intrusion further inland, stressing freshwater supplies for urban and agricultural sites [73].

Along the coast, reduced sediment delivery and rising sea levels contribute to severe erosion. Mangrove forests, which provide vital natural coastal protection, strongly depend on sufficient sediment input to sustain and grow. Within the Mekong Delta Living Lab project, research and pilot interventions are carried out to restore and strengthen Vietnam's mangrove forests [51]. While much of this research focuses on coastal areas, the underlying drivers of change often originate inland. It is therefore highly valuable to investigate the future impacts driving changes in sediment supply. This thesis contributes to that aim by studying the Song Hau tidally influenced zone, by assessing the impact of anthropogenic and climatic drivers on future sediment transport and bifurcation behaviour, system mechanisms that are critical for the sustainability of mangrove ecosystems.

1.2. Research gap

This research aims to address the growing need to understand how climate and human drivers influence sediment dynamics in the Song Hau distributary system over the coming decades, particularly as climate change and human interventions continue to evolve. While the Vietnamese Mekong Delta, including its coastal areas and mangrove forests, has been extensively studied, most existing research focuses on present-day conditions and short-term changes, without fully considering their long-term development. The loss of mangroves, which are crucial for coastal stability, highlights the need for a more comprehensive understanding of sediment transport from upstream sources. By applying long-term scenarios, this study provides valuable insights into how altered precipitation, sea-level rise, sand mining, and hydropower-induced discharge changes affect future sediment transport and bifurcation behaviour with respect to symmetry and stability, an aspect that remains underrepresented in current literature.

1.3. Research questions

The main objective of this study is to assess long-term sediment transport and bifurcation behaviour in the Song Hau distributary over a 30-year simulation, focusing on processes driven by human activities and climate change. The main research question is:

What are the relative impacts of primary climatic and anthropogenic drivers on sand-dominated sediment transport through the Dinh An and Tran De channels of the Song Hau distributary over a future 30-year simulation period?

To support this research question, two sub-questions are formulated:

1. How do projected anthropogenic and climatic drivers affect the magnitude and spatial distribution of erosion and deposition within the Song Hau distributary over the next 30 years?
2. How does the bifurcation, in terms of symmetry and stability, respond under different drivers over the next 30 years?

1.4. Methodology

To answer these research questions, a Delft3D 2D depth-averaged model is developed to simulate the water flow and sediment transport in the Song Hau distributary. Four scenarios are applied to assess their relative impacts on sediment and bifurcation dynamics over a 30-year simulation.

1.5. Reading guide

This thesis begins with a literature review in Chapter 2, which outlines the regional setting of the Vietnamese Mekong Delta (VMD) and the Song Hau distributary channel. It also discusses the key drivers of sediment dynamics and the influence of the bifurcation point on sediment transport within the distributary system. Chapter 3 describes the setup of the Delft3D model, including all aspects of its construction using the Delft3D-FLOW and SED modules, as well as the scenario design. Chapter 4 presents the model verification results, while Chapter 5 outlines the simulation results for both the base and future scenarios. Chapter 6 discusses the results, including uncertainties and limitations. Finally, the conclusion and recommendations are presented.

2

Literature review

2.1. Regional setting

The Mekong River (Figure 2.1) is one of the largest rivers in the world, it originates in the Tibetian Plateau in China and flows through five countries in southeast Asia: Myanmar, Thailand, Laos, Cambodia and Vietnam. It has a total catchment area of 795000 km^2 with a length of 4800 km [18]. As the Mekong river transitions into the Mekong Delta in Southern Vietnam, it enters a region that has been steadily prograding over the last 4000 years. This land growth occurred at a rate of approximately 13–14 m/year due to continuous sediment deposition, forming sediment layers of typically 18–25 m thick and reaching up to 45 m in ancient incised channels [91].

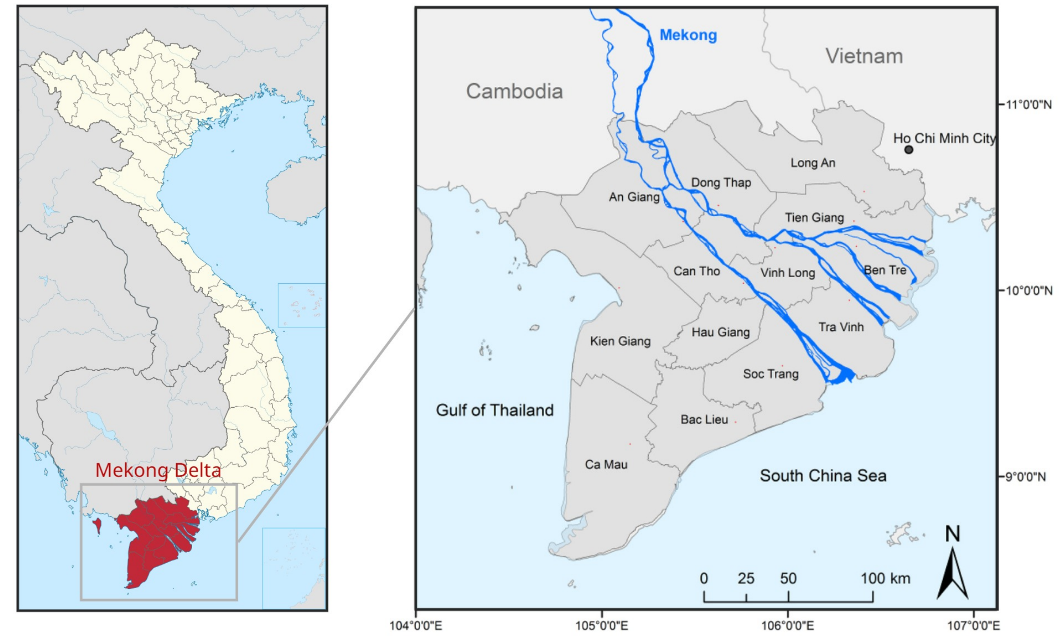

Figure 2.1: The Mekong Delta in Vietnam (based on [87]).

The Mekong Delta receives an annual average discharge of approximately $1.5 \times 10^4\ \mathrm{m}^3/\mathrm{s}$ [5, 60], with the Song Hau carrying 40-50% of this discharge [53]. The total sediment load at the Mekong mouth was estimated to be 140 ± 40 Mt/year before drastic human interventions, like hydropower dams [21, 75]. However, sediment delivery by the delta has been estimated to be reducing, with reductions ranging over a wide range of 60 to even 96% compared to this initial total sediment load [40].

The Song Hau distributary channel, also known as the Bassac River, is one of the two main branches of the Mekong River in Vietnam and forms part of the Mekong Delta. It separates from the Mekong near the Cambodia–Vietnam border, where the river divides into the Song Hau and Song Tien. Further downstream, the Song Hau bifurcates into the Tran De and Dinh An distributaries, separated by Cu Lao Dung Island (Figure 2.2).

Various bars and islands are located within the Song Hau distributary downstream of Can Tho. These typically form in alluvial rivers with a high sediment load, strong seasonal flow variation, and broad, tidally influenced channels. Such conditions reduce flow velocities, stimulate sediment deposition, and allow for the formation of mid-channel bars that may stabilize over time through vegetative colonization [13, 38]. In the Song Hau, many of these islands have since been protected by dikes and no longer flood during high-water conditions.

The bathymetry of the Song Hau reflects its dynamic nature and multi-channel structure. Main channels generally reach depths between −10 and −25 m, with average depths of around −15 to −20 m across much of the system. Shallower zones (−5–0 m) occur along riverbanks and in side channels. Between islands, bathymetric profiles often reveal deep, scoured channels formed by concentrated flow, while shallower side channels develop in low-energy zones. These observations are based on bathymetric datasets from surveys conducted between 2008 and 2023 by national and provincial agencies, coordinated by the Institute of Coastal and Offshore Engineering (ICOE) [3, 4, 19, 20, 66, 67, 68, 69].

Island surface elevations are generally above +0 m VNES (Vietnam National Elevation System), ranging up to 11 m, with higher elevations concentrated in the central parts of the islands [30]. Lower-lying outer zones indicate transitional areas at the land–water interface. VNES corresponds to the long-term mean sea level at Hon Dau, Do Son District, Hai Phong City [86].

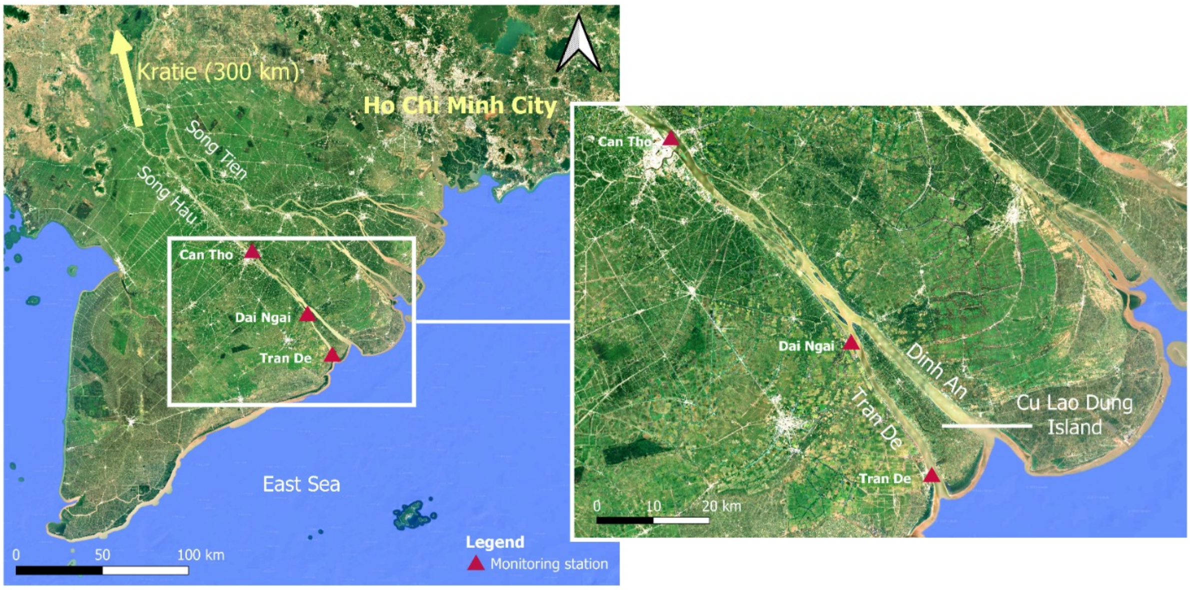

Figure 2.2: Study area (right) within the Mekong Delta (left), showing monitoring stations and key river features

The distribution of water and suspended sediment to the South China Sea is strongly influenced by a tropical monsoon climate. The wet season, dominated by the southwest monsoon winds, occurs from May to October, with the high-flow season in the delta spanning approximately June to December. In contrast, the dry season, driven by the northeast winds, spans from November to April, with the low-flow season in the delta from January to May [18].

Earlier research on the lower Song Hau distributary demonstrates strong seasonal variability in water and sediment partitioning, focusing on short-term seasonal differences. During the high-flow season, the Dinh An distributary carries approximately 73% of the total river discharge of the Song Hau River, accounting for 90% of the suspended sediment concentration (SSC). In contrast, during the low-flow season, it transports 96% of the total discharge, while the SSC flux is directed inwards from the ocean [89]. The high-flow season discharge is 20–30 times larger than that of the low-flow season [57].

The tide also plays an important role in the sediment dynamics of the lower Song Hau distributary. The tidal system is a combination of semi-diurnal and diurnal tides, with a notable imbalance between the two. There is a distinct asymmetry between the flood and ebb tides, with the flood tide lasting significantly shorter than the ebb tide. The maximum tidal range is approximately 3.5 m at the river mouth, while the average tidal range is about 2.2 m. At Can Tho, located approximately 90 km upstream from the river mouth, the tidal range varies from around 2 m in the low-flow season to 0.7 m in the high-flow season [76, 77, 78].

In the low-flow season, particularly when flow decreases to less than 70% of the average discharge, saltwater intrudes much further upstream. Salinity levels of 6 PSU are recorded 45 km upstream [29]. In contrast, during the high-flow season, freshwater reaches the river mouth. The extent of the intrusion is partly due to the elevation range of the tidal and coastal region, which has a relatively flat terrain, ranging from 0.3 to 0.7 m [61]. High subsidence rates caused by anthropogenic influences, such as groundwater extraction and infrastructure loading, also allow saltwater to intrude further during the dry season. According to Eslami (2021), by 2050, the area affected by saltwater intrusion increases by 10–27% compared to 2021 due to anthropogenic influences, with an additional 6–19% increase caused by sea-level rise. Saltwater then reaches as far upstream as Can Tho [26].

Seasonal and tidal variations strongly influence sediment transport in the Song Hau distributary. During the dry season, the riverbed in the estuary is mostly made up of mud. Estuarine circulation pushes sediments upstream, depositing finer particles near the river mouth. Bed load transport of sand becomes more significant during high discharge, especially in the Dinh An channel, which is more efficient at exporting sand to the continental shelf compared to the Tran De channel [5]. The Dinh An channel is ebb-dominated, whereas the Tran De channel is flood-dominated. Studies reveal that sand is transported towards the sea during the ebb phase, especially with stronger tidal currents [89].

These seasonal transport dynamics are reflected in the spatial and temporal variation in sediment composition along the distributary. Detailed morphological and sediment studies [5, 13, 56] report consistent downstream fining trends and seasonal shifts in grain size and composition. Upstream near Can Tho and before the bifurcation, sediments are sand-dominated, with 60–75% sand during high discharge and 40–60% in low flow, while clay remains below 30%. Grain sizes range from fine to medium sand (190–250 μm), with coarse sand (>500 μm) present in low amounts (<10%). Just downstream of the bifurcation, sediment composition shows the greatest seasonal shift: sand exceeds 80–90% during high discharge but drops to 30–50% in low flow, while clay increases up to 40%. Near the river mouths, particularly in the dry season, sediments are finest, dominated by clay (40–70%) and reduced sand content (10–25%). Sand grains are mostly fine (150–190 μm), with more medium sand during low flow. This downstream fining and seasonal variability reflect the influence of saltwater intrusion and density-driven layering, which reduce flow velocities and stimulates the settling of fine suspended particles.

2.2. Drivers influencing sediment dynamics in the Mekong Delta

2.2.1. Overview of sediment dynamics drivers

The flow regime and sediment movement in the Mekong Delta are influenced by a complex interaction of human, climatic, and natural stressors. The stability of the delta depends on a balance between sediment supply, deposition, and redistribution. In recent decades, intensified human activities and the growing impacts of climate change increasingly disrupt this balance [26]. Figure 2.3 provides a schematic overview of the main drivers and their effects on sediment and water fluxes within the system.

To ensure a broad and representative analysis, the following key drivers are selected for further exploration: excessive sand mining, hydropower dam construction, groundwater exploitation linked to (natural) subsidence, sea-level rise, and altered precipitation patterns. These drivers form the focus of the analysis presented in this study and are discussed in the following sections. A summary of the scenarios is provided in Table 2.1.

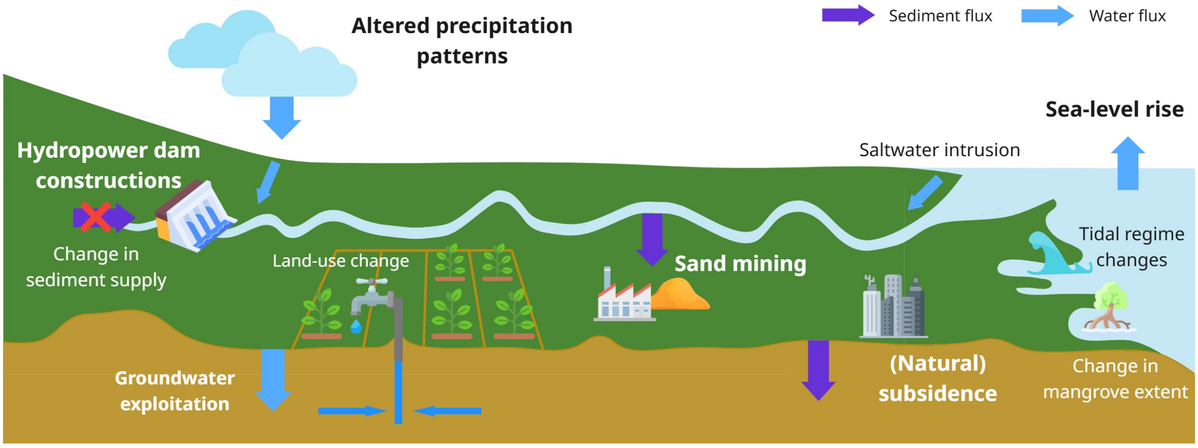

Figure 2.3: Schematisation of drivers influencing the Mekong Delta (modified from Minderhoud (2019) [49])

Table 2.1: Description of the future Climate and Anthropogenic scenarios

Code	Scenario	Description
Altered precipitation	AP	Higher discharge in both wet and dry seasons.
Hydropower dams	HD	Upstream sediment trapping and a flattened hydrograph.
Sand mining	SM	Increased sediment extraction at active mining sites.
Sea-level rise	SLR	Elevated downstream water levels due to sea level rise and subsidence.

2.2.2. Altered precipitation

A global increase in precipitation due to climate change is expected. Over the VMD, annual rainfall is projected to increase by 5–12% by 2050 under the RCP4.5 scenario, and up to 18% under the RCP8.5 scenario, compared to the 1986–2005 baseline [48]. Recent research by Ly et al. [42] linked altered precipitation patterns under climate change to projected increases in river discharge throughout the Mekong River system. Under the SSP2-4.5 scenario, discharge is expected to increase by approximately 9% in the near future (2021–2050), by 18–20% in the mid-century period (2041–2070), and up to 27–33% by the end of the century (2071–2100).

Seasonally, the wet season (May–October) is projected to experience more pronounced increases in discharge, while the dry season (November–April) is expected to show more moderate changes. However, an overall increase in annual discharge is expected, with the most significant rises occurring in the latter half of the century, particularly under high-emission scenarios. Figure 2.4 presents the percentual changes per season due to altered precipitation under various climate projections.

2.2.3. Hydropower dam constructions

An enormous increase in hydropower dam placements has taken place in the Mekong River Basin. Since 1996, 131 operational dams have become operational [16], serving multiple purposes: electricity generation, expanded irrigation, climate change adaptation, and improved navigation. To meet the growing energy demand of 6–7% per year, many more dams are planned in the coming decades [43, 59].

These dams have a high impact on both water and sediment dynamics. By flattening flood peaks and modifying downstream discharge, they significantly alter the hydrological regime of estuarine systems like the Song Hau distributary. Peak flows are projected to decrease by 5–24%, while dry-season flows may rise by 25–160% [39]. Ly et al. [42] found similar trends, reporting a −11% reduction in wet-season flows and a +30% increase during the dry season in the Lower Mekong Basin. The impact of hydropower dams on discharge is illustrated in Figure 2.4.

Research by Cornielje (2023) shows that the annual load of silt and clay has dropped from 140 ± 40

Mt/year before major dam construction to just 26 ± 9 Mt/year by 2020. With more dams planned, this load is expected to decline even further, to just 4–8 ± 3–5 Mt/year by 2040 [21].

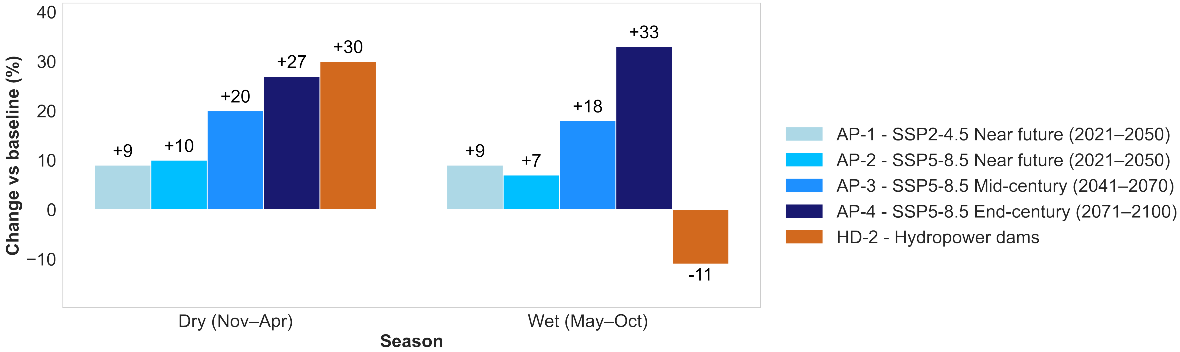

Figure 2.4: Relative change per season for the discharge modification scenarios: Altered Precipitation (AP) and Hydropower Dams (HD)

2.2.4. Sand mining

Sand mining in the Mekong delta has expanded significantly since the early 1990s, driven by growing global demand for construction materials. Historically, the Mekong River carried around 160 Mt of sediment annually before dam construction [47], much of which was deposited across the delta [13, 54]. This sediment supply is increasingly exploited. Although regulations exist, enforcement is weak, and licenses are often granted or renewed despite violations [65]. Licensing is managed provincially, without cross-provincial coordination, leading to unregulated and potentially unsustainable extraction [52, 90].

Several studies quantify sand mining across the delta, showing substantial and growing extraction rates. Brunier et al. (2014) [14] estimate a net loss of 110.5 Mm^3 from the Hau River (1998–2008). Across both the Tien and Hau channels, the net loss is around 190 Mm^3, or 20 Mm^3/yr. Extrapolated to the whole delta, this gives 35.5 Mm^3/yr. Vasilopoulos et al. (2021) [85] report similar values for that period and an increase to 58.4 Mm^3/yr from 2008 to 2018. Other estimates vary: 28 Mm^3/yr in 2015 [25], 17.77 Mm^3/yr in 2018 [37], and 8.5 Mm^3/yr in 2012 [12]. Figure 2.5 shows the results, reflecting regional and methodological differences.

ICOE [34] identified sand mining sites in the study area from 2014 to 2025 (Figure 3.6). Exact coordinates and characteristics of each site are provided in Appendix D.2. According to official licenses, a cumulative extraction volume of at least 37.5 Mm^3 of sediment was allowed over this period [1, 7, 8, 9, 10, 70, 79, 82, 80, 81]. However, additional unreported mining likely increases actual volumes, and weak monitoring suggests extraction often exceeds licensed limits.

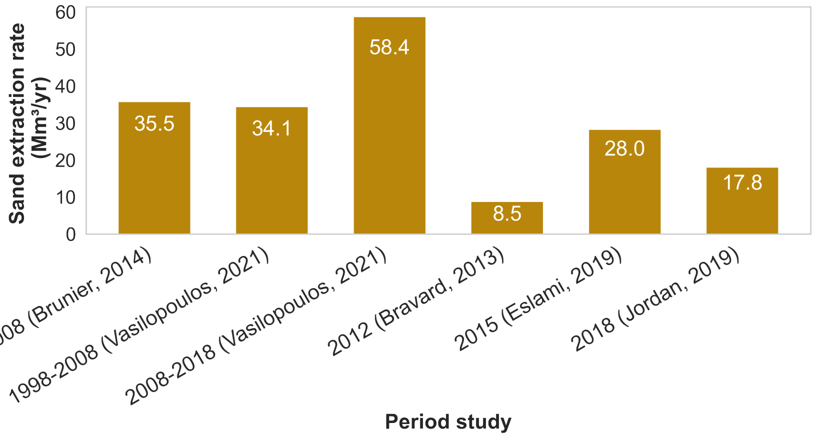

Figure 2.5: Extraction rates of Sand Mining Activities in the VMD of various studies

2.2.5. Sea-level rise

Groundwater exploitation is one of the main causes of severe subsidence in the Mekong delta. However, natural subsidence also occurs due to the compaction of fine-grained (clayey) sediments deposited during the second half of the Holocene. These sediments undergo high rates of consolidation over time. Other human activities such as infrastructural loading, sand mining, and dam construction further exacerbate the effects of natural compaction [91].

The Institute of Coastal and Offshore Engineering (ICOE) conducted research on sea-level rise and delta subsidence rates in the Mekong Delta. The monitoring stations and their respective rates are shown in Figures 2.6 and 2.7. At the Tran De station, located at the river mouth of the Tran De distributary, a water level change rate of 1.045 cm/yr is reported for the period 2000–2024. This rate of water level change, also referred to as relative sea-level rise (RSLR), consists of two components: sea level rise (SLR) and land subsidence, as expressed in Equation 2.1.

$$\Delta H_{\text{RSLR}} = \Delta H_{\text{SLR}} + \Delta H_{\text{subsidence}} \tag{2.1}$$

with ΔH the relative change in water level.

At Tran De, these components are valued at 0.392 cm/yr for SLR and 0.653 cm/yr for subsidence. The SLR component is based on the assumption that no subsidence occurs at the Vung Tau station, a monitoring location situated just south of Ho Chi Minh City. Therefore, the RSLR measured at Vung Tau is considered equal to the regional SLR.

Figure 2.6: Location of monitoring stations in the Mekong Delta used in the ICOE study on Relative Sea Level Rise [34].

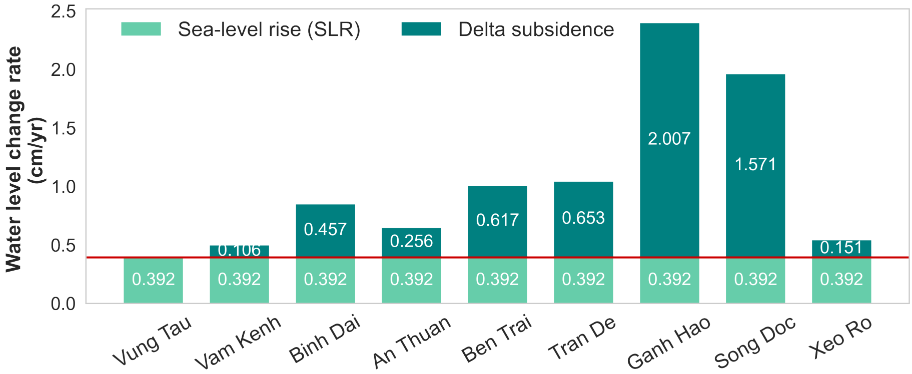

Figure 2.7: Relative Sea Level Rise trends (2000–2024) based on ICOE observations at the monitoring stations [34].

2.3. Sediment transport and bifurcation behaviour in the Song Hau distributary

2.3.1. Sediment transport

In rivers and deltas, sediment moves mainly in two ways: as bedload or as suspended load. Bedload consists of heavier sand and gravel that stay close to the riverbed. When the flow reaches the threshold of motion, these grains start to move by rolling, sliding, or hopping along the bottom. As the flow velocity increases, more grains move at higher speeds.

Suspended load consists of finer material that is lifted from the bed by turbulent motion in the water. These small grains can remain suspended for a long time before slowly settling. Depending on their origin, two types of suspended material can be distinguished: bed material load, which comes from the riverbed itself and moves in and out of suspension as part of the bedload, and wash load, which comes from upstream erosion and consists of very fine particles that stay suspended almost continuously. The amount of wash load depends more on the sediment entering the river than on flow strength [36]. Figure 2.8 shows the classification of sediment transport in terms of both mechanism and origin.

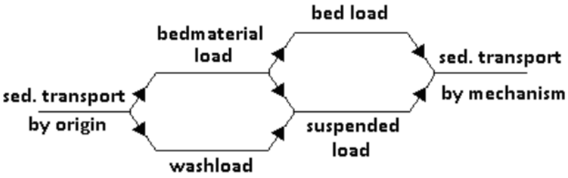

Figure 2.8: Classification of sediment transport according to origin and transport mechanism (based on conceptual scheme of [36]).

The balance between bedload, suspended load, and wash load depends on factors such as grain size, flow velocity, bed slope, and turbulence. Together, these processes shape the riverbed and control how sediment spreads through the delta [84].

2.3.2. Tide-influenced bifurcation

The Song Hau distributary contains a tide-influenced bifurcation where the flow splits between the Dinh An and Tran De channels. This bifurcation plays a central role in distributing both water and sediment throughout the system and strongly affects downstream morphology. Tidal forces influence the flow, leading to periods when the flow direction reverses in one or both channels. As a result, sediment transport patterns differ from those in river-dominated bifurcations, where flow generally occurs in one direction and downstream channels compete for discharge.

Throughout the tidal cycle, the bifurcation may behave either as a true bifurcation during ebb, or as a confluence during flood, depending on the relative timing and strength of tidal forcing in each branch. This tidal influence reduces the probability of channel abandonment that is commonly observed in river-dominated systems [35]. In those cases, one downstream channel often captures most of the discharge, while the other gradually silts up. In contrast, in tide-influenced systems, the flow reversal caused by tides keeps both channels open by allowing water and sediment to move back and forth between them [33]. Figure 2.9 illustrates the six flow regimes that can occur during a tidal cycle, showing how the bifurcation shifts between acting as a bifurcation and a confluence under different tidal and river flow conditions.

To characterise a bifurcation, two key terms need to be considered: stability and symmetry. These terms are indicators for describing the state and long-term behaviour of a bifurcation [35, 33]. Below, both terms are defined.

- **Stability:** A bifurcation is considered *stable* when interactions between tides, river flow, sediment transport, and morphology maintain a balance between the branches, keeping both channels open and active over time. An *unstable* bifurcation amplifies small differences in geometry, flow, or sediment load. When one branch receives less sediment than its transport capacity, it tends to erode, while the other accumulates excess sediment and gradually silts up. This feedback can ultimately cause one branch to become dominant or close entirely.

- **Symmetry:** A bifurcation is *symmetric* when discharge and sediment are approximately equally divided between the branches. It is *asymmetric* when one branch persistently carries a larger share of discharge or sediment than the other.

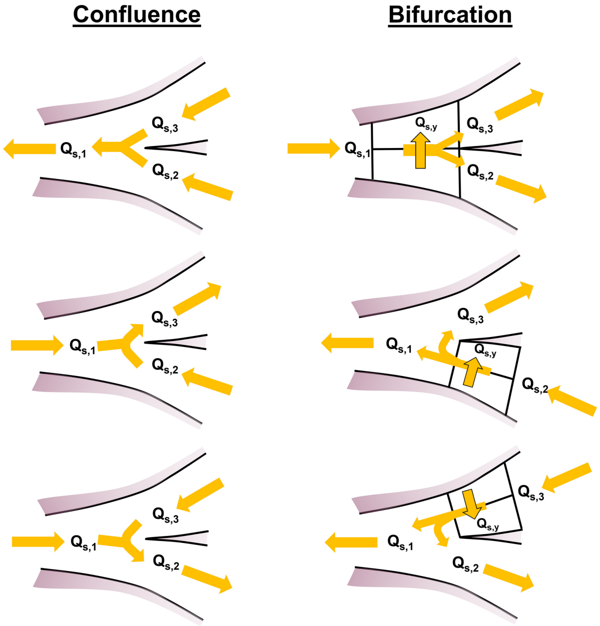

Figure 2.9: Flow regimes of a tidal-influenced bifurcation. Illustration by Iwantoro (2022) [35]. Q_s indicates the along-channel sediment transport, whereas $Q_{s,y}$ indicates the transverse sediment transport.

To quantify symmetry and identify the dominant branch at a tidally influenced bifurcation, several asymmetry indices have been used in prior studies [35, 33]. In this study, an asymmetry index for discharge and sediment load is adopted following Buschman et al. (2010) [15], which is widely used in literature. In this study, the indices are defined as in Eq. (2.2).

$$\Psi_Q = \frac{|Q_{\mathrm{TD}}| - |Q_{\mathrm{DA}}|}{|Q_{\mathrm{TD}}| + |Q_{\mathrm{DA}}|}, \qquad \Psi_S = \frac{|S_{\mathrm{TD}}| - |S_{\mathrm{DA}}|}{|S_{\mathrm{TD}}| + |S_{\mathrm{DA}}|}. \tag{2.2}$$

with:

- Q is water discharge (m^3/s) and S is total (bed + suspended) sediment transport rate (m^3/s)
- Range: $\Psi \in [-1, 1]$
- $\Psi > 0 \Rightarrow$ Tran De (TD) dominates
- $\Psi < 0 \Rightarrow$ Dinh An (DA) dominates
- $\Psi = 0 \Rightarrow$ symmetric

The stability and symmetry of a bifurcation are influenced by several interacting factors, including the tidal regime, variability in river discharge, sediment transport processes near the bifurcation point, and the evolution of channel bed levels and cross-sectional geometry. Together, these factors determine whether small perturbations are damped out or amplified, ultimately controlling the long-term evolution of the bifurcation system. The influence of the main factors are explained below.

- **Tidal regime:** Tidal forcing has a non-monotonic influence on bifurcation behaviour. Low tidal ranges can increase asymmetry and promote instability, intermediate ranges tend to stabilise the junction and balance partitioning, very high ranges can destabilise the system again through intensified flood–ebb asymmetry and stronger morphodynamic feedbacks [35]. Over a tidal cycle, during flood, phase and head differences can drive inflow from the deeper/faster branch into the shallower branch, stimulating transverse exchange and increasing asymmetry. During late ebb, sediment is preferentially redistributed from the deeper to the shallower branch, damping asymmetry. The net effect depends on the balance of these processes over the tidal cycle [35, 33, 15].

- **River discharge variability:** When river flow is high, tidal forcing is pushed back: the bifurcation behaves more river-dominated, with mostly seaward flow and little switching during the tidal cycle. When river flow is low, tidal forcing penetrates further, the junction switches more between bifurcation and confluence during the tidal cycle, and water/sediment partitioning fluctuates more [33, 35]. This increased variability in flow can lead to asymmetry as one branch may receive more discharge and sediment than the other, depending on the tidal phase. The more frequent switching between bifurcation and confluence also increases the instability, as the channels become more sensitive to changes in flow and sediment transport, potentially causing one branch to dominate over time.
- **Sediment transport processes:** Stability depends on how much sediment is supplied relative to how much the flow can carry at the junction. If supply exceeds capacity, sediment accumulates and one branch can silt up. if it is lower, the other branch tends to erode and deepen. Thresholds for grain movement are set by grain size and flow strength [15, 35].
- **Geometry and bathymetry:** Geometric features determine how sensitive the junction is to asymmetry: the width–depth ratio (w/h), the junction angle, overall convergence, and bars near the junction. A large w/h or an unfavourable angle makes an even split unlikely. In addition, bars and bed-level differences push more flow into one branch and change the shear, also leading to an imbalanced split [35].

2.3.3. Hypothesis on scenario outcomes

All four scenarios are hypothesised to affect the stability and symmetry of the bifurcation point by altering the incoming discharge (Q), incoming and outgoing sediment load (Q_s) and downstream tidal forcing. A summary of the hypothesised effects for each scenario is provided in Table 2.2

An overall increase in discharge is likely to improve the stability and symmetry of the bifurcation point, as expected under altered precipitation patterns due to climate change [74]. A stronger river signal can reduce the influence of tides, suppressing backflow and sediment redistribution, which supports more symmetrical flow division [33, 35].

Morphological differences between downstream branches, as in the case of sand mining, can disrupt the bifurcation balance and promote asymmetry. Bed lowering deepens one branch, reducing hydraulic resistance and head loss at the node, thereby favouring that branch in terms of discharge (Q) and sediment load (Q_s) [62, 63, 23]. However, bed lowering also decreases the local width–depth ratio (w/h) because depth increases. A lower w/h can stabilise a symmetric partition if both branches are similar, but deepening only one branch is likely to promote asymmetry.

Relative sea-level rise elevates downstream water levels and strengthens backwater effects. Its implications for bifurcation dynamics, however, are not yet fully understood. Higher downstream levels extend backwater reaches, reduce tidal dominance and flow velocities, and may stabilise discharge and sediment routing [41, 27]. Conversely, sea-level rise can also deepen channels and enhance flood dominance. When deposition occurs unevenly between branches, asymmetry may increase [35].

Hydropower development tends to flatten the natural discharge signal by reducing peak flows and raising base flows. During high-flow events, increased discharge stimulates sediment transport and temporarily alters flow partitioning between branches. The dominant branch tends to receive more flow and sediment, promoting local deposition and reducing its hydraulic advantage, which helps stabilise the bifurcation over time. Dampening high-flow events suppresses sediment pulses and reduces bed-load transport, thereby limiting the system's capacity to redistribute sediment between branches and making it more vulnerable to asymmetry [64, 24]. Furthermore, hydropower dams trap sediment upstream, reducing the downstream sediment supply. This can lead to sediment starvation in the branches and long-term morphological imbalance [21].

Table 2.2: Hypothesised effects of each scenario in terms of discharge Q and sediment transport Q_s

Scenario	Effect on discharge (Q)	Effect on sediment (Q_s)	Asymmetry likelihood
AP	Higher Q in both wet and dry seasons, with a relatively stronger increase during the dry season	Q_s increases proportionally with Q	Decrease (↓)
HD	Higher Q in the dry season, lower Q in the wet season	Q_s reduced by upstream trapping	Increase (↑)
SM	More Q routed to the deepened branch	More Q_s through the deepened branch	Increase (↑)
SLR	Higher downstream resistance due to backwater, reducing the river discharge influence	Promoting sedimentation near the river mouths due to backwater effects	Unclear (↔)

3

Delft3D Model Setup

3.1. Modelling framework

In Figure 3.1, the modelling framework of this study is presented. The Delft3D-FLOW and SED modules are used to simulate hydrodynamics and sediment transport in the Song Hau distributary channel. The figure illustrates the sequence of modelling steps, the input data required for each step, and the corresponding outputs.

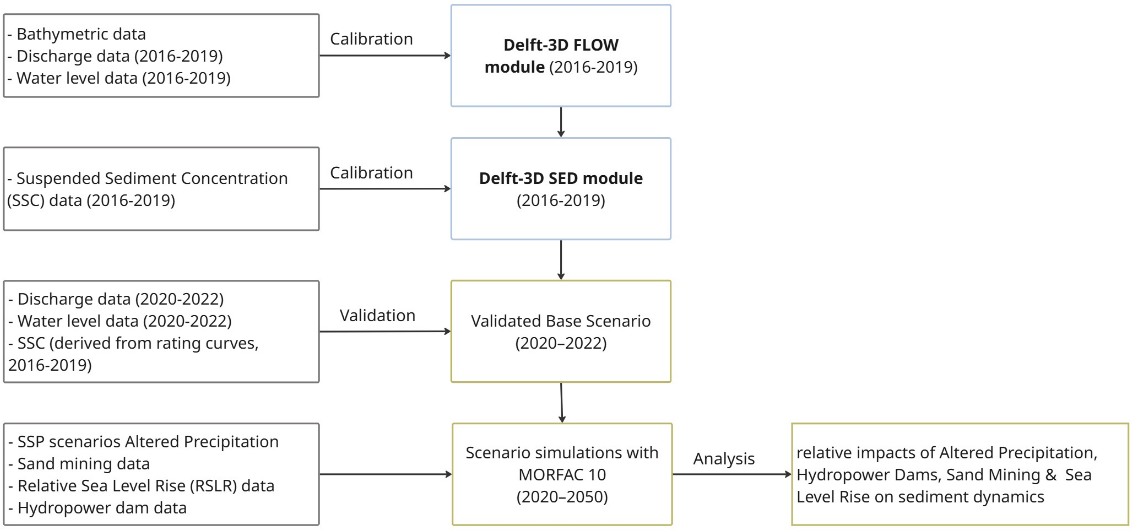

Figure 3.1: Schematic overview of the modelling framework used in this study.

In this chapter, the steps of this framework are discussed in detail, beginning with the Delft3D-FLOW characteristics, followed by the Delft3D-SED characteristics, and concluding with the scenario design.

3.2. Delft-3D FLOW

3.2.1. Computational grid

A curvilinear structured grid is generated in Delft3D using the RGFGRID tool to accurately represent the geometry of the Song Hau distributary. The model domain extends from Can Tho to the river mouths of the Dinh An and tran De channels. Figure 3.2 shows the Delft3D model domain, including the monitoring cross-sections, the upstream discharge boundary, and the downstream water level boundaries.

The grid is projected in VN-2000 UTM Zone 48N using Cartesian coordinates and consists of 551 rows

(M-direction) and 62 columns (N-direction). A two-dimensional depth-averaged configuration is applied, meaning no vertical layers are included. The model latitude is set to 9.7° decimal degrees.

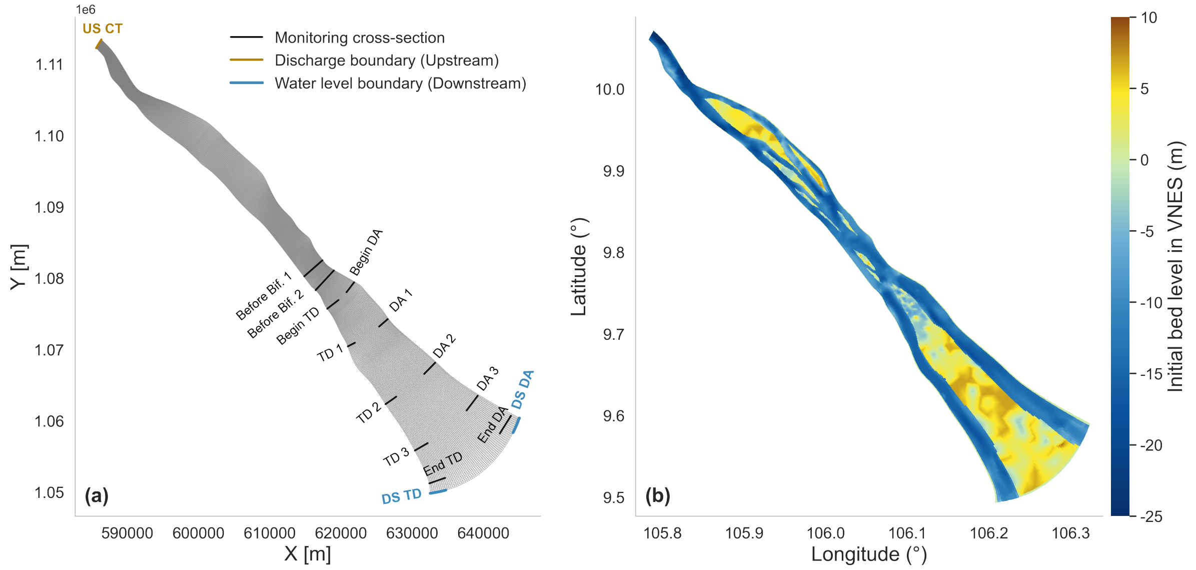

Figure 3.2: Delft3D input: (a) locations boundaries and monitoring cross-sections, (b) initial bed level/bathymetry

3.2.2. Bathymetry and Elevation

The bathymetric dataset is created with results from national and provincial survey projects conducted between 2008 and 2023, provided by the Institute of Coastal and Offshore Engineering (ICOE). These include sedimentation and erosion monitoring programs led by the Ministry of Agriculture and Rural Development (MARD, 2008–2011, 2019) [3, 4], the Ministry of Science and Technology (MOST, 2009–2013, 2016, 2017–2020, 2020) [66, 67, 68, 69], and Tra Vinh province (2014, 2023) [19, 20]. The bathymetric data are referenced to the WGS84 coordinate system, with the vertical datum defined by the Vietnam National Elevation System (VNES), which corresponds to the long-term mean sea level at Hon Dau, Do Son District, Hai Phong City [86].

Elevation data for the islands within the study area are derived from Google Earth, with coordinates also referenced to the WGS84 system (epoch 6172, most recent: 2005) [30]. The vertical datum in Google Earth is relative to the WGS84 ellipsoid. A Helmert transformation is applied to convert the coordinates from the WGS84 ellipsoid to the VN-2000 reference frame. The transformation parameters and methodology used for the vertical datum conversion are provided in Appendix A, based on [71].

Interpolation of the bathymetric and elevation data over the grid is conducted using the QUICKIN tool in Delft3D. The steps of the approach are summarized below:

1. Triangular interpolation of the islands within the study area.
2. Bathymetric interpolation over the full model domain using only the bathymetric data points.
3. Smoothing of the land–water interface in selected areas by reapplying triangular interpolation over the bathymetric data points.

3.2.3. Flow conditions

The model runs with a time-step of 0.5 minutes, and the time is referenced to the local time zone (LTZ) of UTC +7, which aligns with GMT (GMT = Local time - LTZ). For calibration purposes, the reference date is set to 01 January 2016, and for validation to 01 January 2020. Both simulation periods have a duration of three hydrodynamic years.

Three open boundaries are implemented in the model: one upstream discharge boundary at Can Tho (m^3/s) and two downstream water level boundaries at the river mouths of the Dinh An and Tran De channels (m). These boundaries are defined using hourly time series, with no tidal time lag applied at the downstream boundaries, as the distance between the river mouths is small (±20 km) and can therefore be neglected. Given that the study focuses on long-term sediment dynamics, short-term temporal offsets, such as tidal time lags, are considered irrelevant. The initial water level in the model is set to the average of the downstream water level time series.

3.2.4. Model parameters

Roughness is used as a calibration parameter for the hydrodynamics of the model. According to a MIKE 21 model of the coastal region provided by ICOE [34], the Manning's roughness coefficient typically ranges between 30 and 37 $m^{1/3}/s$. A best fit is obtained using a Manning coefficient of 30 $m^{1/3}/s$.

Wetting and drying conditions are enabled in the model with the following parameters: `ExtDry` = 0.05 (threshold for transitioning from wet to dry cells), `LimDry` = 0.10 (limit for dry cell conditions), and `MinDepth` = 0.01 (minimum water depth for cells to remain wet). These settings ensure accurate simulation of areas with fluctuating water levels.

Hydrodynamic constants, such as gravity, water density, and a constant related to turbulent flow resistance (`beta_c`), are kept at their default values. Viscosity and diffusivity are also set to default values, with uniform horizontal eddy viscosity of 1 m/s^2 and horizontal eddy diffusivity of 10 m^2/s.

3.3. Delft3D-SED

3.3.1. Characteristics SED-module input

Suspended sediment concentrations (SSC) at the upstream boundary are divided into two non-cohesive sand classes, representing fine to medium grain sizes: 87 μm (70%) and 175 μm (30%) [55], as these are considered the most representative classes for the developed Delft3D model of the Song Hau distributary. For simplicity, the same grain-size proportions are applied under both flood and ebb tide conditions.

The riverbed is defined with a total sediment thickness of 10 m, with 70% (7 m) of 87 μm sand and 30% (3 m) of 175 μm sand. Only sand-dominated transport is considered to reduce model complexity and computational run time, so cohesive sediments are excluded [89]. Coarser sediment classes are also excluded, as these are not transported under the hydrodynamic conditions. Specific density and dry bed density are kept at their default values for both classes, respectively: 2650 kg/m^3 and 1600 kg/m^3. Initial sediment concentrations are set based on the average values from the time series for both sediment classes: 0.00891 kg/m^3 for 87 μm and 0.023175 kg/m^3 for 175 μm.

3.3.2. Transport conditions

A time series of suspended sediment concentration (SSC) values, along with daily flood and ebb tide measurements at Can Tho, is provided by ICOE [34] for the period 2016–2018. Positive flow velocity is defined as the ebb tide (outflow to the sea), and negative velocity as the flood tide (inflow from the sea). SSC values during flood tides are associated with the daily minimum discharge, while those during ebb tides correspond to the daily maximum discharge. Initial sediment concentrations at the upstream boundary are set to the average SSC from the time series. At the downstream river mouths, an equilibrium boundary is applied, meaning that the amount of sediment entering through the boundary is assumed to be equal to the amount leaving the boundary, as no SSC data is available for this region.

The Van Rijn (2004) sediment transport predictor [22] is used for the simulation of sediment transport in the Delft3D model. This formula is selected because it is well-suited for sand-dominated, non-cohesive sediment transport and accurately accounts for both bed and suspended load in estuarine systems. A similar approach using Van Rijn (2000) is successfully applied in this study area by Xing et al. (2017) [89], confirming its suitability for the local sediment and flow conditions. The formula definitions can be found in Appendix C.

For the simulation of the scenarios over 2020-2050, the Morphological Scale Factor (MORFAC) is set to 10. This factor is used to accelerate morphological changes in the model by adjusting the sediment transport rates, allowing for faster simulation of long-term morphological processes. Secondary flow is also activated in the model to account for the additional lateral flow components that occur due to channel curvature and turbulence. This helps to more accurately simulate sediment redistribution across the riverbed and refines the representation of sediment transport dynamics.

Other settings are kept at default with a spin-up interval of 720 minutes, a minimum depth for sediment calculation of 0.1 m. For Van Rijn's formula, a reference height factor of 1 (-) and a threshold sediment thickness of 0.05 m are applied.

3.4. Scenario design

3.4.1. Scenario overview

The Delft3D model assesses the relative impacts of four future scenarios on sediment and bifurcation dynamics in the Song Hau distributary. These scenarios reflect key drivers of change and are evaluated against a baseline reference case.

Each scenario represents a 30-year morphological period, driven by hydrodynamic forcing and suspended sediment concentration (SSC) data from the years 2020 to 2022. As no continuous SSC time series is available for this period, the SSC inputs are constructed using rating curves derived from 2016–2019 data (see Appendix B). A morphological acceleration factor (MORFAC) of 10 is applied to compress the 30-year morphological period into a three-year simulation. Figure 3.3 shows a schematisation of the base scenario together with the four scenario designs. An overview of all scenarios is provided in Appendix D.1, which will be further discussed in the following sections.

The following criteria are used to evaluate changes in sediment and bifurcation dynamics:

1. Sediment transport across the Dinh An and Tran De distributaries
2. Spatial pattern analysis of bed level change
3. Bifurcation dynamics in terms of symmetry and stability

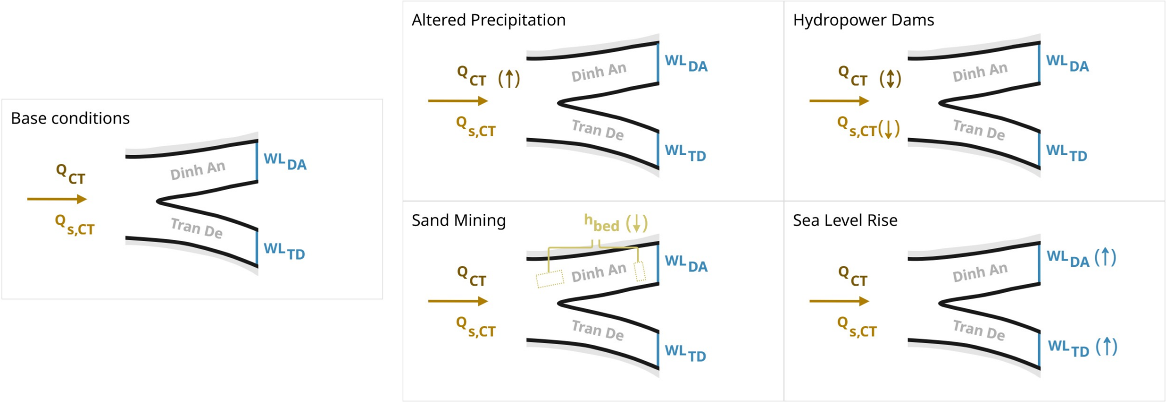

Figure 3.3: Schematisation of scenarios

3.4.2. Scenario group 1: Discharge modifications

Four scenarios are implemented to investigate the impact of altered precipitation patterns on the Song Hau distributary. For the near future (2021–2050), two scenarios are applied: SSP2–4.5 and SSP5–8.5. For the mid future (2041–2070) and far future (2071–2100), the SSP5–8.5 scenario is used, as it represents more severe climatic changes and enables a better assessment of potential impacts. The relative seasonal changes applied to the discharge time series are presented in Figure 2.4, resulting in the adjusted time series for each scenario as shown in Figure 3.4.

Hydropower dams also affect the incoming discharge at Can Tho, as well as the incoming sediment. Three scenarios are applied to investigate their impact. In the first scenario, an 80% reduction of the SSC input is applied, based on findings by [21]. This reduction is implemented as a linear decrease in SSC over time, starting from 100% of the baseline value in 2020 and declining to 20% after 3 years, after which it remains constant:

$$SSC_{\text{scaled}}(t) = \max\left(0.2,\ 1.0 - \frac{0.8}{1095} \cdot t\right) \cdot SSC_{\text{baseline}}(t)$$

where t is the number of days since 1 January 2020.

The second scenario includes modifications to the discharge, as dam regulation is expected to flatten the hydrograph. Following projections for both SSP2-4.5 and SSP5-8.5 scenarios [42], a 30% increase in the dry season and an 11% decrease in the wet season are applied to the discharge input time series. The third scenario combines both effects. Also for the Hydropower Dams scenario with induced discharge flattening (HD-2), the adjusted time-series is presented in Figure 3.4.

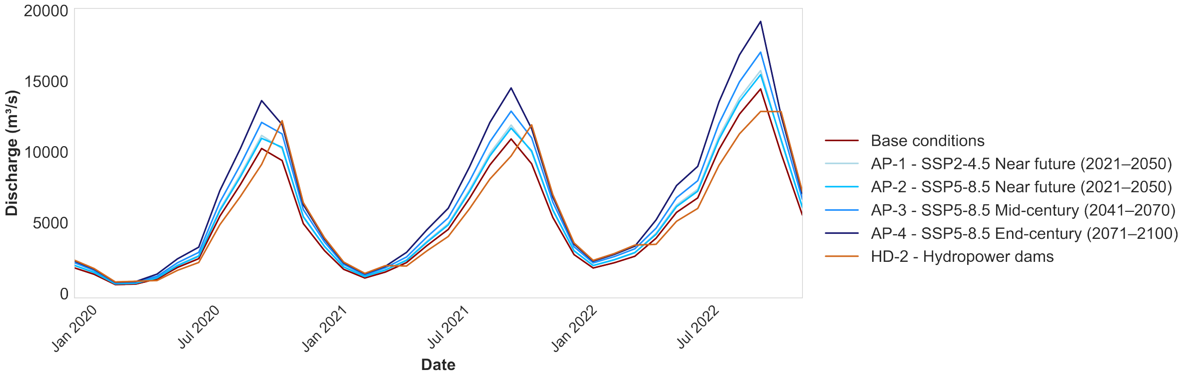

Figure 3.4: Time-series of monthly discharge under each discharge modification scenario: Altered Precipitation (AP) and Hydropower Dams (HD)

3.4.3. Scenario group 2: Water level increases

To simulate future changes due to sea-level rise and subsidence changes over a 30-year morphodynamic period, time series are generated by applying linearly increasing water level shifts at the downstream boundary. A morphological acceleration factor (MORFAC) is used to compress the 30-year physical period into a 3-year simulation.

The applied rate per simulation year is scaled using:

$$r_{\text{sim}} = r_{\text{year}} \cdot \frac{T_{\text{morph}}}{T_{\text{sim}}} \qquad \text{with } T_{\text{morph}} = 30 \text{ yrs}, \ T_{\text{sim}} = 3 \text{ yrs, giving:} \qquad r_{\text{sim}} = r_{\text{year}} \cdot \left(\frac{30}{3}\right) \tag{3.1}$$

where r_{sim} is the applied rate (m/year) and r_{year} is the observed annual sea level rise. Using $r_{\text{SLR}} = 0.00392$ m/year and $r_{\text{RSLR}} = 0.01045$ m/year, this results in:

$$r_{\text{SLR, sim}} = 0.0392 \text{ m/year}, \quad r_{\text{RSLR, sim}} = 0.1045 \text{ m/year}$$

For each time step, the elapsed time since the start of the simulation is computed in fractional years. The corresponding elevation shift is then applied as:

$$\Delta h(t) = r_{\text{sim}} \cdot t \tag{3.2}$$

The shift $\Delta h(t)$ is added to the original downstream water level series (Tran De) to construct the adjusted boundary time series under SLR and RSLR conditions, visualized in Figure 3.5.

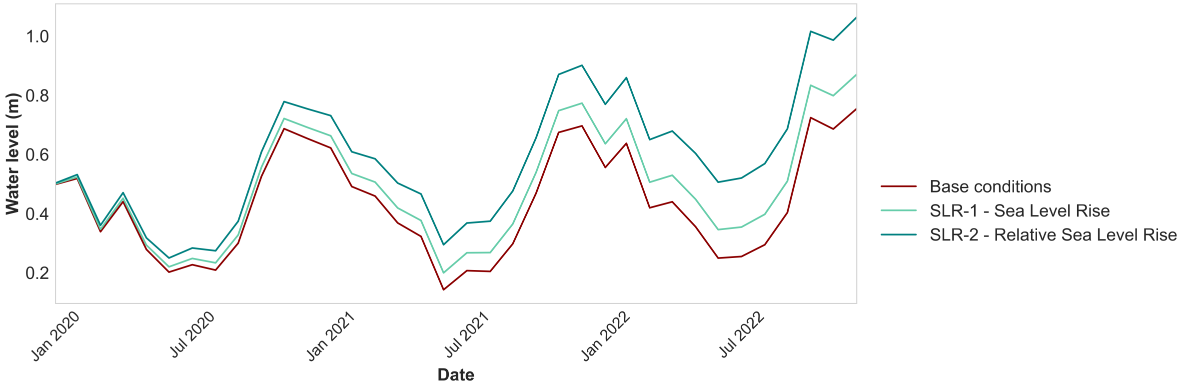

Figure 3.5: Monthly downstream water level time-series for the base conditions, Sea Level Rise and Relative Sea Level Rise

3.4.4. Scenario group 3: Bed level lowering

For the Sand Mining scenario, a Dump and Dredge (DAD) file is created using the *Dump and Dredge Areas* tool in QUICKIN of Delft3D. The selected areas are based on research conducted by ICOE [34], which provides information on sand mining activity locations and corresponding mining areas. Appendix D.2 presents the characteristics of the sand mining activities and the input data used for the DAD file generation. Figure 3.6 visualizes the defined DAD areas.

Three scenario designs are examined, with extraction rates of 1 Mt/yr, 2 Mt/yr, and 4 Mt/yr. The maximum rate is constrained by the available sediment load in the SSC forcing time series. Extraction is applied uniformly across all areas shown in Figure 3.6.

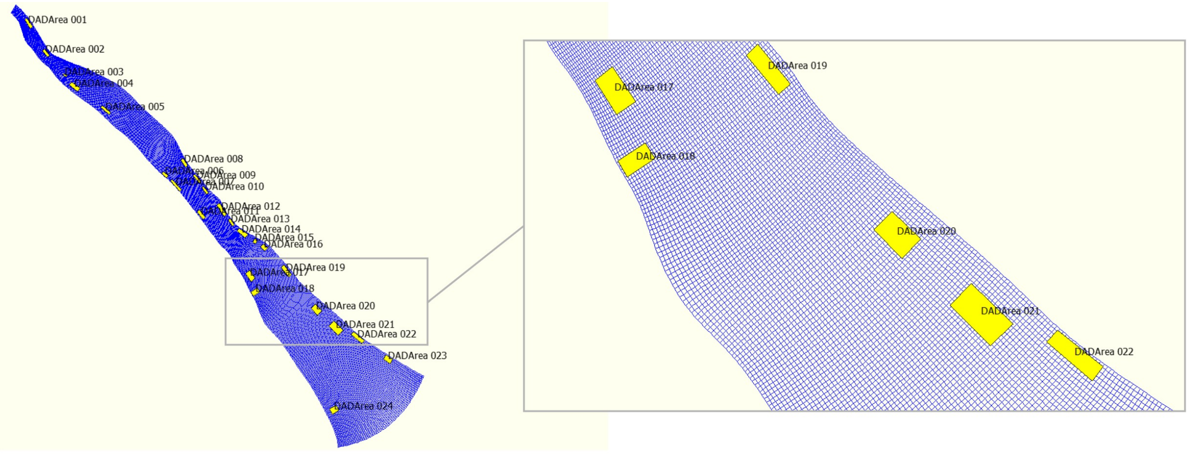

Figure 3.6: Polygons of sand mining activities in Delft3D model

4

Model verification

4.1. Overview

This section describes the verification and performance assessment of the developed Delft3D model. First, the performance metrics are introduced, followed by the calibration and validation of the hydrodynamics in the Delft3D-FLOW module, and finally the calibration and validation of the sediment transport in the Delft3D-SED module.

4.2. Metrics for model performance

Model performance is evaluated using the Nash–Sutcliffe Efficiency (NSE) and the Root Mean Square Error (RMSE), as defined in Equations 4.1 and 4.2. The NSE measures how well the model reproduces the observed variability, with values closer to 1 indicating better replication of the observed dynamics. The RMSE quantifies the average prediction error (in metres in this study), where smaller values indicate higher accuracy. Together, these metrics provide a robust assessment of both the timing and magnitude of simulated water levels [50].

$$\text{RMSE} = \sqrt{\frac{1}{n}\sum_{i=1}^{n}\left(S_i - O_i\right)^2} \tag{4.1}$$

$$\text{NSE} = 1 - \frac{\sum_{i=1}^{n}\left(S_i - O_i\right)^2}{\sum_{i=1}^{n}\left(O_i - \bar{O}\right)^2} \tag{4.2}$$

where:

- S_i: the simulated value
- O_i: the observed value
- $\bar{O}$: the mean of the observed values
- n: the number of time steps.

4.3. Verification of Delft-3D FLOW

Hydrodynamic calibration is performed over the period 2016–2019 at Dai Ngai station (Figure 4.1a), which is validated over the period 2020–2022 (Figure 4.1b). The model performance is indicated in Figure 4.2. The model reproduces the seasonal cycle but shows a systematic positive bias of 0.1908 m, which is removed by applying a constant bias correction.

In calibration (2016–2019), NSE improves from ∼0.89 (raw) to ∼0.94 (bias-corrected) and RMSE from ∼0.28 m to ∼0.20 m, showing improvements due to bias correction and good (RMSE) to very good (NSE) results. In validation (2020–2022), raw NSE is low overall (∼0.25 overall) but rises to very good after bias correction (∼0.90 overall). RMSE drops from ∼0.20–0.21 m (raw, good) to ∼0.07–0.08 m (bias-corrected, very good). Performance is generally better in the dry season than in the wet season. Overall, once the mean bias is removed, the model gives a very good depiction of the timing and magnitude of downstream water levels.

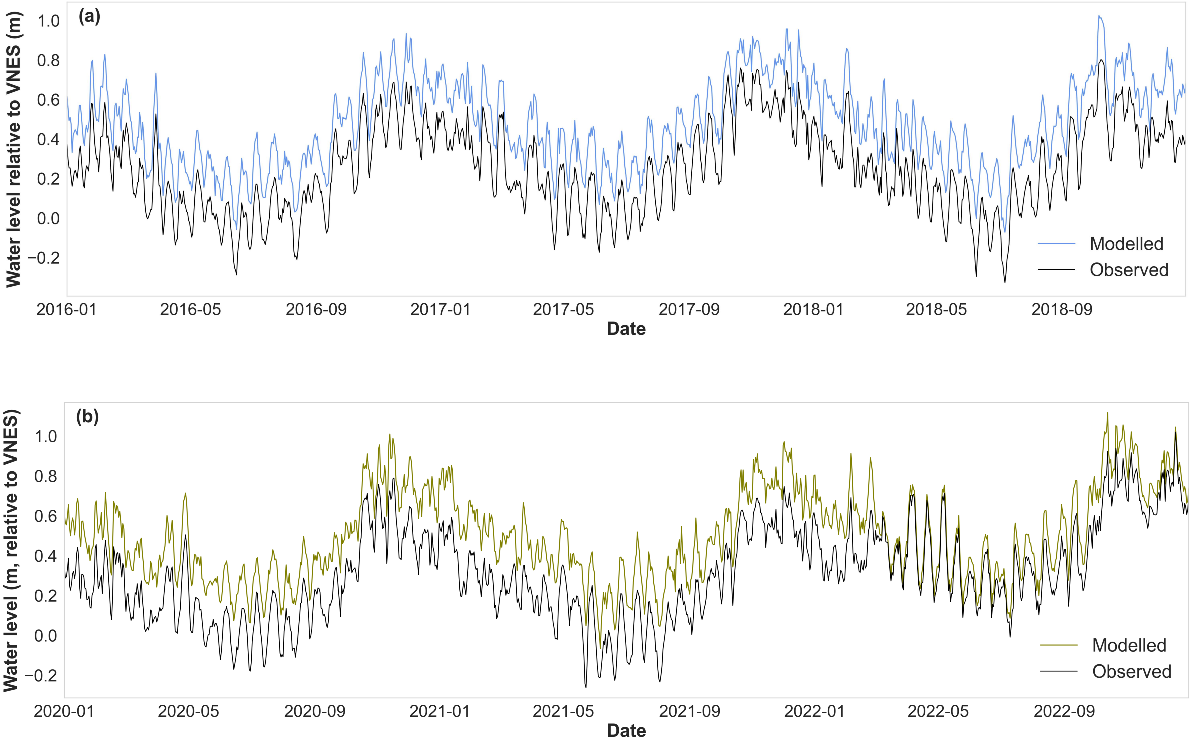

Figure 4.1: Comparison of modelled and observed water levels at Dai Ngai, relative to VNES: (a) 2016–2019 (calibration) and (b) 2020–2022 (validation).

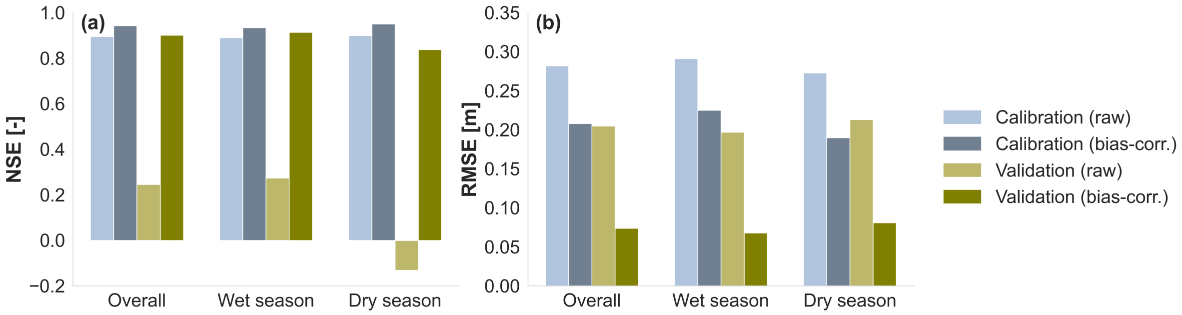

Figure 4.2: Model performance metrics: (a) Nash–Sutcliffe Efficiency (NSE). (b) Root Mean Square Error (RMSE)

4.4. Verification of Delft-3D SED

The sediment transport component of the model is calibrated on the base scenario (normal hydrodynamic forcing) run without morphological acceleration (MORFAC = 1). The calibration uses estimates of the total sediment load (Mt/yr) expected to pass through the domain, derived from the input suspended sediment concentration (SSC) time series. Calibration is carried out by comparing simulated sediment transport at several cross-sections with the input SSC data, with focus on the area before the bifurcation, as this represents the domain without boundary disruptions and the main focus of this study. Upstream and downstream sediment fluxes are evaluated and found to be close to zero, indicating that net sedimentation approximately balances net erosion within the model domain. The model results show that coarse sediment fractions are not effectively transported under the hydrodynamic forcing: thus, particles coarser than 175 μm are excluded from the simulation.

Model validation is performed by comparing the modelled suspended sediment concentration (SSC) and corresponding fluxes at several cross-sections with the forced SSC input. Figure 4.3 shows the instantaneous SSC comparison and the RMSE between the input and the modelled values at monitoring locations ranging from the upstream boundary to the cross-sections before the bifurcation. The RMSE of 0.03–0.04 kg/m³ corresponds to roughly 10–20 % of the observed SSC magnitude, indicating good model agreement in terms of absolute concentration levels. The model therefore reproduces the correct order of magnitude of SSC, which is considered sufficient for the scope of this study: relative, long-term scenario comparison.

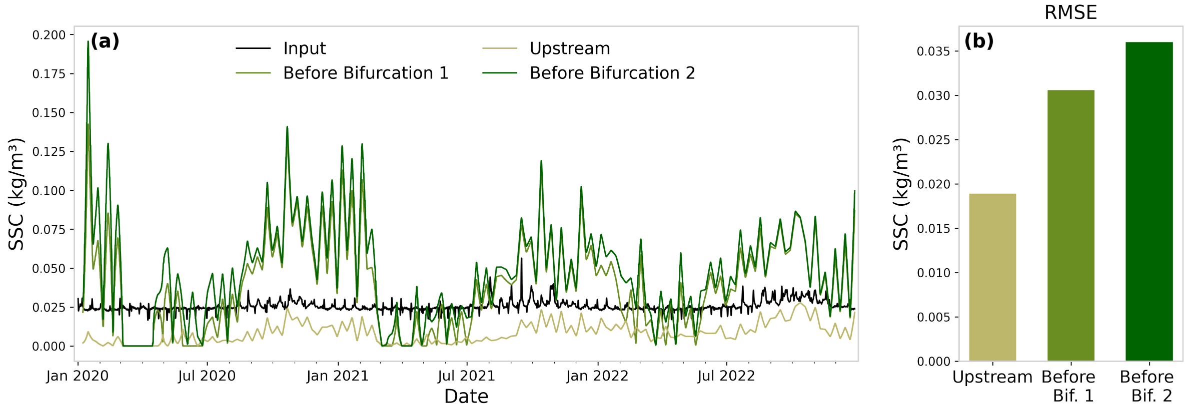

Figure 4.3: Comparison of instantaneous SSC flux of input with several monitoring cross-sections: (a) Time-series. (b) RMSE

At the upstream cross-section, the model systematically underestimates SSC, as can be seen from the discharge ratio in Figure 4.4. The boundary inflow discharge is not fully translated to the model domain, resulting in lower $Q_{upstream}/Q_{input,boundary}$ ratios, especially during the dry season (Nov-Apr). Model performance is generally better during the wet season (May–Oct), when discharge magnitudes are higher.

Since suspended sediment flux scales with $F_{\text{sus}} = QC$ and concentration C typically increases with discharge following a power-law relation $C = aQ^b$ with $b > 0$ a reduction in Q directly reduces both F_{sus} and C [64]. This relationship explains why underestimation of inflow discharge leads to lower simulated SSC in the upstream section. Additionally, the use of the Van Rijn (2004) capacity-based transport formulation contributes to this behaviour. The model continuously adjusts SSC toward an equilibrium concentration (C_{eq}) determined by the local hydraulic conditions and sediment properties. As a result, excess SSC from the boundary tends to deposit near the entrance of the domain. A more detailed explanation of this mechanism is provided in Section 6.5.2. To complement this analysis, additional figures are presented in Appendix E.

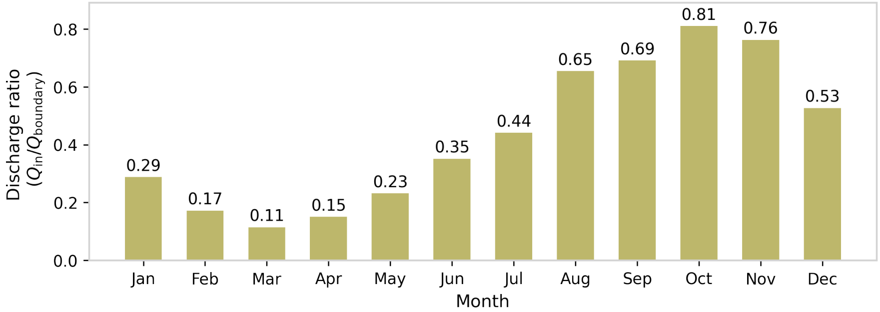

Figure 4.4: Monthly discharge ratio ($Q_{upstream}/Q_{input,boundary}$). Ratio = 1 indicates full throughflow of boundary discharge, while ratio < 1 reflects loss of boundary input.

5

Results

5.1. Overview

The results address three aspects of system behaviour: (i) sediment transport, (ii) spatial patterns, and (iii) bifurcation dynamics. For each aspect, outcomes are first presented by scenario group, and then findings are synthesized across groups. The scenarios are grouped into four categories based on model modifications:

0. Base (no modification)
1. Discharge modifications (AP-1, AP-2, AP-3, AP-4, HD-2)
2. Water level increases (SLR-1, SLR-2)
3. Bed level lowering (SM-1, SM-2, SM-3)

Scenarios HD-1 and HD-3 are excluded because the upstream SSC input has negligible influence on the model. Sediment transport in the system is dominated by hydrodynamics (see section 6.5.2). As a result, the output of HD-1 is equivalent to the Base scenario and the output of HD-3 is equivalent to HD-2.

5.2. Sediment transport

5.2.1. Sediment transport overview

The figures used to analyse sediment transport over the Dinh An (DA) and Tran De (TD) channels require specific interpretative notes to ensure consistent reading, these are provided in the *Interpretation guideline* , see below. Note that early fluctuations reflect model spin-up of sediment transport, which is also visible in the sediment mass balances per scenario (Appendix E.3). Interpretation therefore focuses on trends after this spin-up phase and on relative comparisons between scenarios rather than absolute magnitudes.

First, the base scenario is analysed, followed by the analysis of sediment transport per scenario group. The figures for the scenario groups (1-3) show only two representative sections in detail to highlight the main differences between scenarios. The interpretation principles remain identical (5.2.1).

Interpretation guideline

1. *Segment division*
   The channels are divided into four line segments, based on the monitoring cross-sections (Figure 5.1).
2. *Cumulative sediment transport curves*
   Cumulative curves (see Figures a,b in 5.2) indicate both the direction and magnitude of sediment flux over time, and the cumulative level represents the total balance since the start of the simulation.
   - Increasing curve = seaward transport (export, land → sea).
   - Decreasing curve = landward transport (import, sea → land).
3. *Segment storage in bar charts*
   Bar charts (see Figure c in 5.2) show the sediment budget per segment. Sediment budgets are derived by subtracting the downstream section from the upstream section of each segment (“Begin DA” – “DA 1”). Positive values indicate net deposition, while negative values indicate net erosion.
4. *Morphological time*
   The simulations apply a three-year hydrodynamic forcing combined with a morphological acceleration factor (MORFAC) of 10. Therefore, the timing of changes in cumulative transport does not correspond to real calendar years. Instead, the curves are interpreted as relative morphological development over the 2020–2050 period.

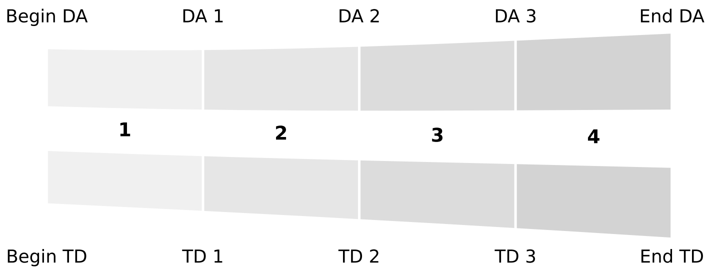

Figure 5.1: Schematisation of Dinh An (DA) and Tran De (TD) channels: **(1–4)** segment numbers.

5.2.2. Sediment transport group 0: Base conditions

In the base scenario (Figure 5.2), both Dinh An and Tran De show a sharp landward sediment pulse during the early simulation years (∼2025–2030), due to the spin-up phase of sediment transport. After this spin-up phase, the channels show different responses. Along Tran De, all cross-sections show a steady upward trend, indicating consistent seaward export from land to sea throughout the remaining period. In contrast, Dinh An exhibits slight seaward transport in its upstream sections, but this remains negligible compared to the much larger landward import at the downstream end. As a result, the minor export upstream cannot compensate for the downstream import, and Dinh An continues to function as a net sediment sink. This contrast is also reflected in the segment storage: Dinh An shows deposition in all segments, whereas Tran De displays limited erosion upstream but clear deposition downstream.

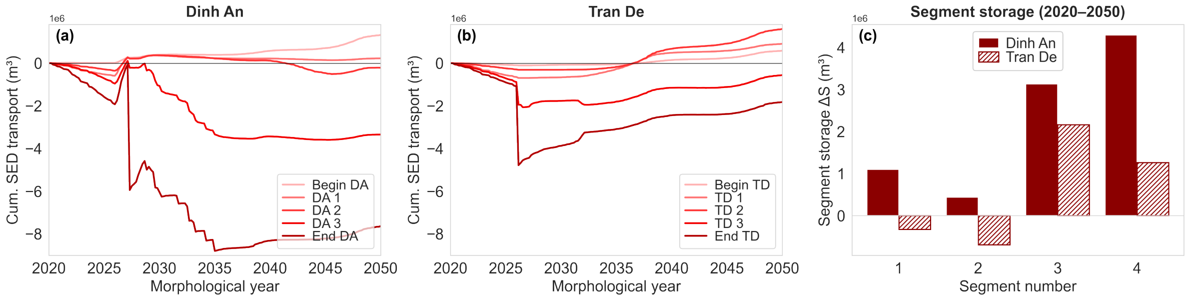

Figure 5.2: Sediment transport for base scenario (a,b): Cumulative sediment transport over time, (c): Sediment budget per channel segment

5.2.3. Sediment transport group 1: Discharge modifications

In Figure 5.3, a representative upstream and downstream section of the Dinh An and Tran De channels are shown, with the sediment budgets presented in panels (c, f). In the upstream sections (panels a, d), the responses across all scenarios are similar, whereas higher variability is observed in the downstream sections (panels b, c). After the spin-up phase, which lasts until approximately 2025 (Appendix E.3), a shift in cumulative sediment transport occurs across all scenarios. From that point onward, transport is directed seaward and gradually increases until 2050, except for the base and HD-2 scenarios in the downstream section of Dinh An, where transport shifts landward after that point. Thus, a higher input discharge decreases the import in the downstream section of the Dinh An branch.

In the Dinh An branch, deposition dominates across all segments, with the highest amounts in the last segment. In contrast, the Tran De branch shows a more balanced sedimentation–erosion pattern, with more pronounced erosion in the upstream segments, except for AP-3, which shows strong deposition in segment 4. The scenario with the highest discharge increase (AP-4) results in the most balanced outcome in terms of sedimentation and erosion. This is notable, as AP-1 to AP-3 show an increasing imbalance, indicating a shift toward a more balanced system response under high discharge. The HD-2 scenario shows the most similar response to the base in the Dinh An branch, but an opposite pattern in the Tran De branch, where HD-2 exhibits slight erosion in the upstream segments, the base shows slight sedimentation in the downstream part. The temporal evolution of each cross-section is presented in Appendix F.

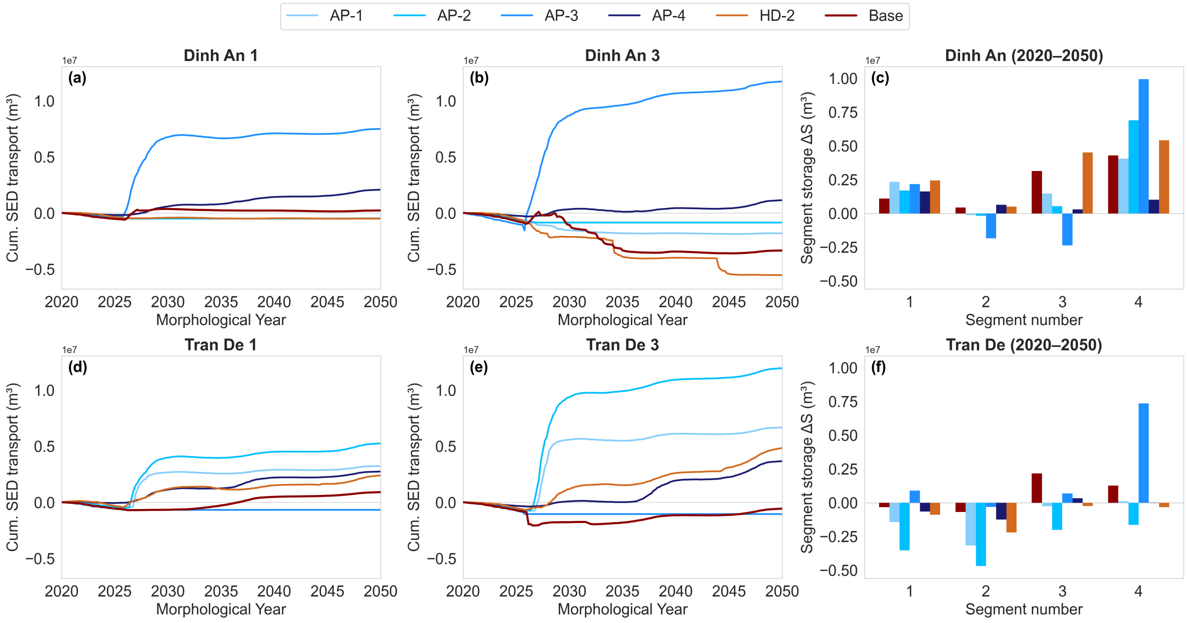

Figure 5.3: Cumulative sediment transport over time (a–b, d–e) and sediment budget per channel segment (c, f) for discharge modification scenarios.

5.2.4. Sediment transport group 2: Downstream water level increases

For the water level increase scenarios (Figure 5.4), deposition is concentrated in the downstream segments of both channels, which is similar to the base response. When subsidence is taken into account (SLR-2), deposition becomes higher in the downstream segments, with relative sea-level rise resulting in more than three times the deposition observed under sea-level rise alone in the Dinh An branch.

The spin-up phase lasts until approximately 2025, after which the sediment response flattens and only slightly increases, and no net erosion is observed. Overall, deposition occurs along both the Dinh An and Tran De branches, which therefore act as net importers. This pattern is consistent with enhanced backwater effects, where higher downstream water levels reduce flow velocities and promote sediment trapping in the lower channel segments. This effect is particularly visible in the Dinh An branch under relative sea-level rise (SLR-2).

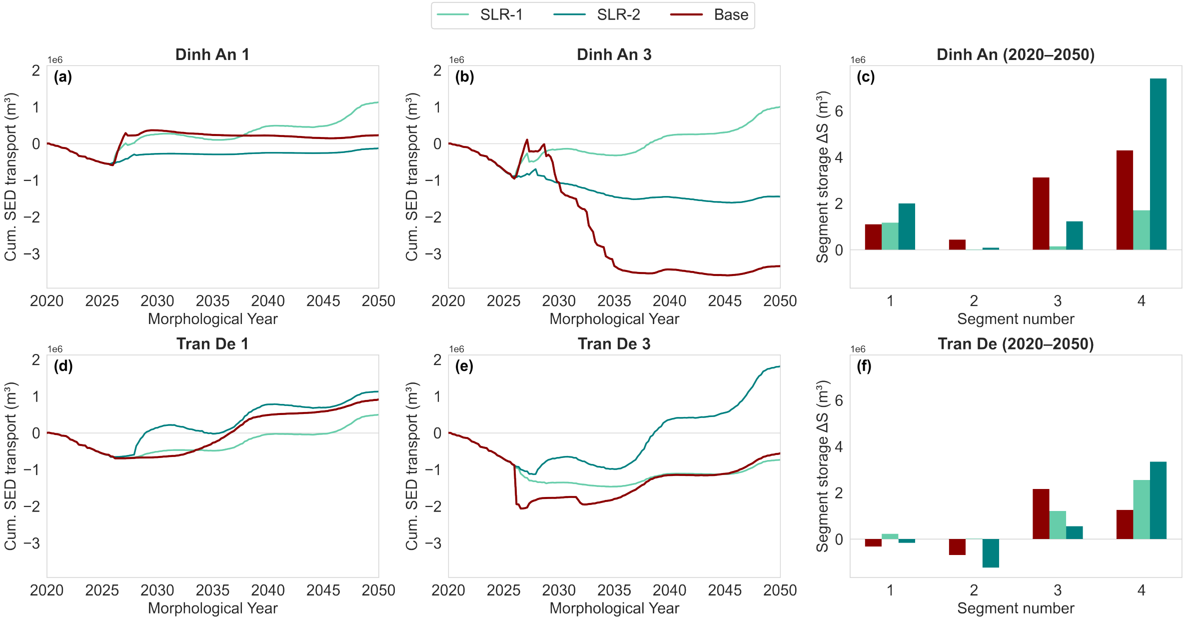

Figure 5.4: Cumulative sediment transport over time (a–b, d–e) and sediment budget per channel segment (c, f) for water level increase scenarios.

5.2.5. Sediment transport group 3: Bed level lowering

For the bed level lowering scenarios with extraction rates of 1, 2, and 4 Mt/yr for SM-1 to SM-3, respectively, sand extraction mainly takes place in the Dinh An channel (Figure 3.6). As shown in Figure 5.5, SM-2 and SM-3 generally show similar responses, with most sedimentation occurring in the downstream segments of Dinh An, whereas SM-1 deviates with stronger deposition in Tran De segment 4. In addition, in SM-1 the cumulative sediment transport direction differs, with seaward transport in Dinh An and landward transport in Tran De after approximately 2025. In SM-2 and SM-3, these flux directions are reversed.

In Tran De, a systematic trend appears with increasing extraction rates: segment 1 shows progressively more deposition, while segments 2 to 4 display decreasing storage. This demonstrates that intensified extraction in Dinh An strengthens the landward sediment flux and increases deposition within the channel. At the same time, it reduces the inward flux in Tran De from SM-1 to SM-3, with SM-3 ultimately showing deposition in the last segment similar to that of the base.

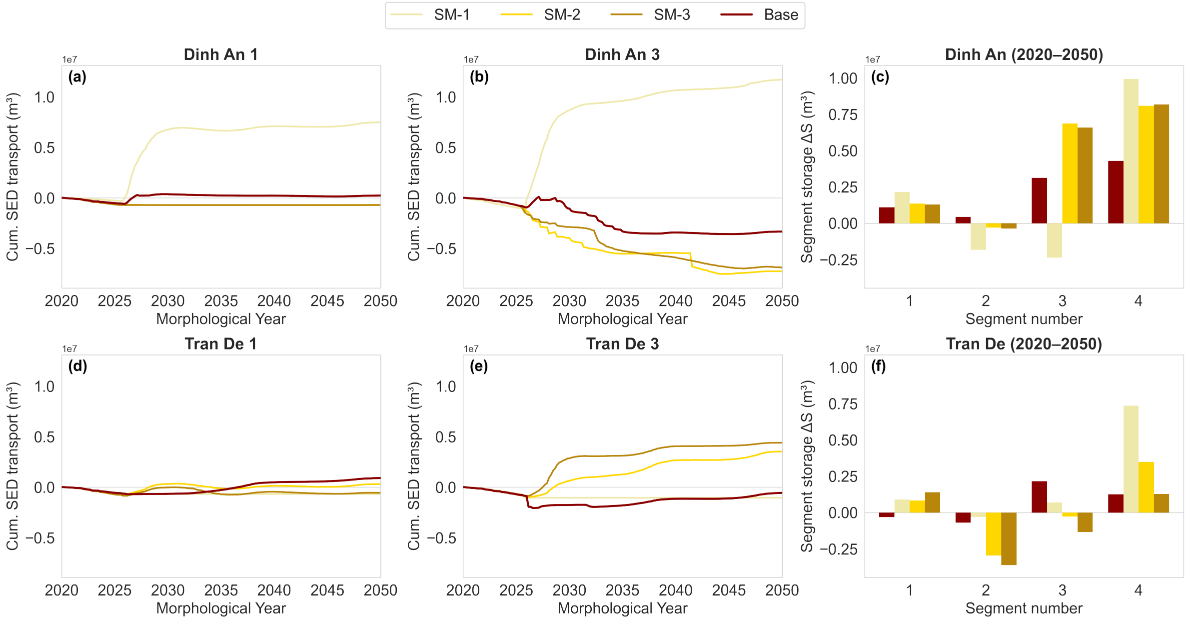

Figure 5.5: Cumulative sediment transport over time (a–b, d–e) and sediment budget per channel segment (c, f) for bed level lowering scenarios.

5.2.6. Overview of net sediment budgets for 2020–2050

Across all scenarios, the net sediment budget over the entire simulation period (2020–2050) is positive for the Dinh An channel, which consistently acts as a sediment importer (Figure 5.6). Values range from a minimum of about 4 Mt up to 26 Mt, with the largest increases occurring under the anthropogenic scenarios, sand mining (SM) and hydropower dams (HD). In contrast, the Tran De channel shows a more variable response. It functions as a sediment exporter in five scenarios, four of which are discharge modifications, and as an importer in the other six. The magnitudes are generally smaller than in Dinh An, mostly between −7 and +14 Mt, with the clear exception of AP-2, where export reaches almost −19 Mt.

A broader perspective reveals systematic patterns. With increasing discharge from AP-1 to AP-4, Tran De and Dinh An shift toward a more balanced state of sedimentation–erosion, especially clear in the Tran De channel. At the same time, with increasing sand mining from SM-1 to SM-3, Dinh An shows progressively larger positive budgets, whereas Tran De shifts from positive under SM-1 to slight net erosion under SM-3. For the water level increase scenarios, no clear trend is defined, but the results indicate strongly intensified sedimentation in Dinh An and a slight reduction in Tran De.

When compared to the base case, AP-4 and SLR-1 produce more balanced outcomes, while the anthropogenic scenarios (except SM-1) deviate strongly for Dinh An. The response in the Tran De channel deviates more markedly from the base, with erosion in about half of the scenarios, although overall magnitudes remain low (except for AP-3).

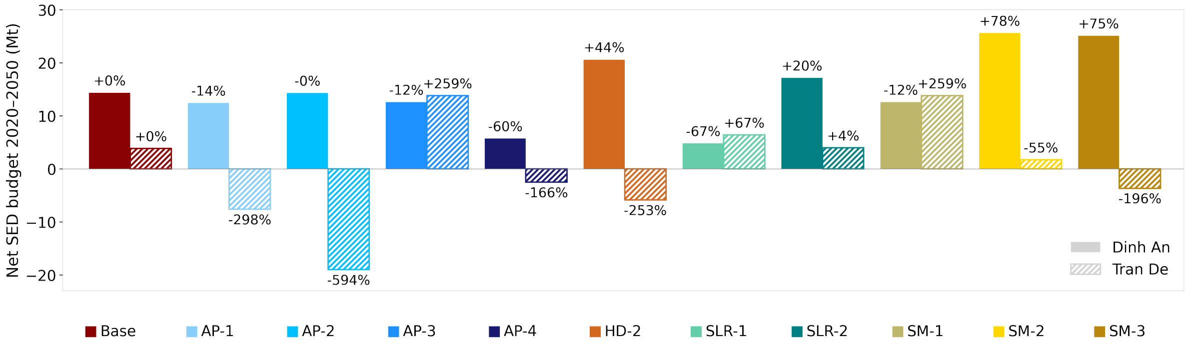

Figure 5.6: Overview of net change in Sediment Budget per scenario (2020-2050)

5.3. Spatial analysis

5.3.1. Spatial analysis group 0: Base conditions

The evolution of bed level change provides a spatial perspective on the morphological adjustments over 2020–2050. Figure 5.7 shows where erosion and deposition occur at 5-year intervals within the channels, with red indicating deposition and blue indicating erosion.

In the early years (2025–2030), clear deposition hotspots form near the mouths of both Dinh An and Tran De. Over time, these depositional zones spread further landward, gradually filling more of the channels. In contrast, erosion mainly appears as the deepening of a dominant flow pathway, especially upstream and next to the depositional zones near the mouths. The erosion becomes more pronounced after significant sedimentation. By 2040–2050, large depositional lobes are visible at the downstream ends, while upstream changes remain more limited. This shows that the estuary does not change uniformly, but through contrasting zones of deposition and channel deepening.

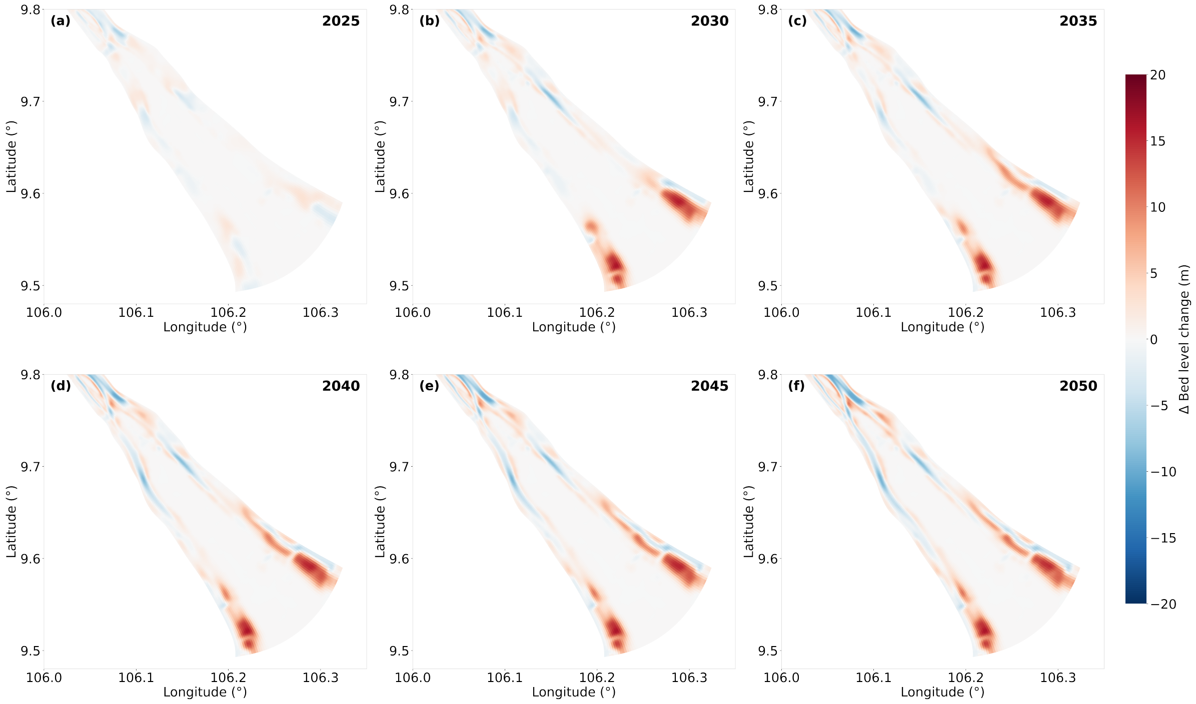

Figure 5.7: Evolution of bed level change (2020-2050) for the base conditions

5.3.2. Spatial analysis group 1-3: all scenarios

As shown in Section 5.2, the most pronounced development of the sedimentation–erosion pattern occurs after 2025 for most scenarios. From this point onwards, the system no longer undergoes extreme changes. Therefore, only the final bed level change in 2050 is presented here for each scenario, while the full temporal evolution is provided in Appendix G.

As can be seen in Figure 5.8, the scenarios with slight discharge increases due to precipitation (AP-1, AP-2) show an erosion pathway through the center of the Tran De channel, while a sedimentation hotspot develops near the river mouth in the Dinh An branch. AP-2 intensifies the AP-1 pattern, indicating a consistent trend. For higher discharge (AP-3), this erosion–deposition contrast becomes less pronounced, and for the highest, far-future discharge (AP-4), it weakens further, suggesting that higher discharge scenarios promote a more spatially balanced sedimentation–erosion pattern in the branches. Induced discharge flattening (HD-2) produces a much larger imbalance than any of the altered precipitation scenarios: the flatter discharge regime drives extreme sedimentation in the river mouth of Dinh An, while erosion in Tran De remains concentrated along the channel centerline. This spatial response closely resembles that of AP-1 and AP-2, but in a more intensified form. The sea-level rise scenarios concentrate deposition in the river mouths of both branches, with a more pronounced effect when subsidence is included (SLR-2). In this case, stronger sedimentation in the downstream part of Dinh An is accompanied by increased erosion in the mid-section of Tran De, while the sedimentation hotspot in its downstream part weakens. For the sand mining (SM) scenarios, sedimentation in the downstream part of the Dinh An channel extends further upstream as sand extraction rates increase, while the erosion pattern in the Tran De channel remains consistently present across all extraction rates.

Overall, extreme sedimentation hotspots in the downstream segments of Dinh An are accompanied by a more pronounced erosion pathway in Tran De. Compared to the base, sedimentation in Dinh An is more concentrated in the downstream segment rather than evenly distributed across multiple segments in both branches. Scenarios with stronger contrasts between the two branches (AP-2, HD-2, SM-1) also show an affected zone in the upstream part of Cu Lao Dung Island, indicating that greater divergence in channel responses increased the area affected by erosion.

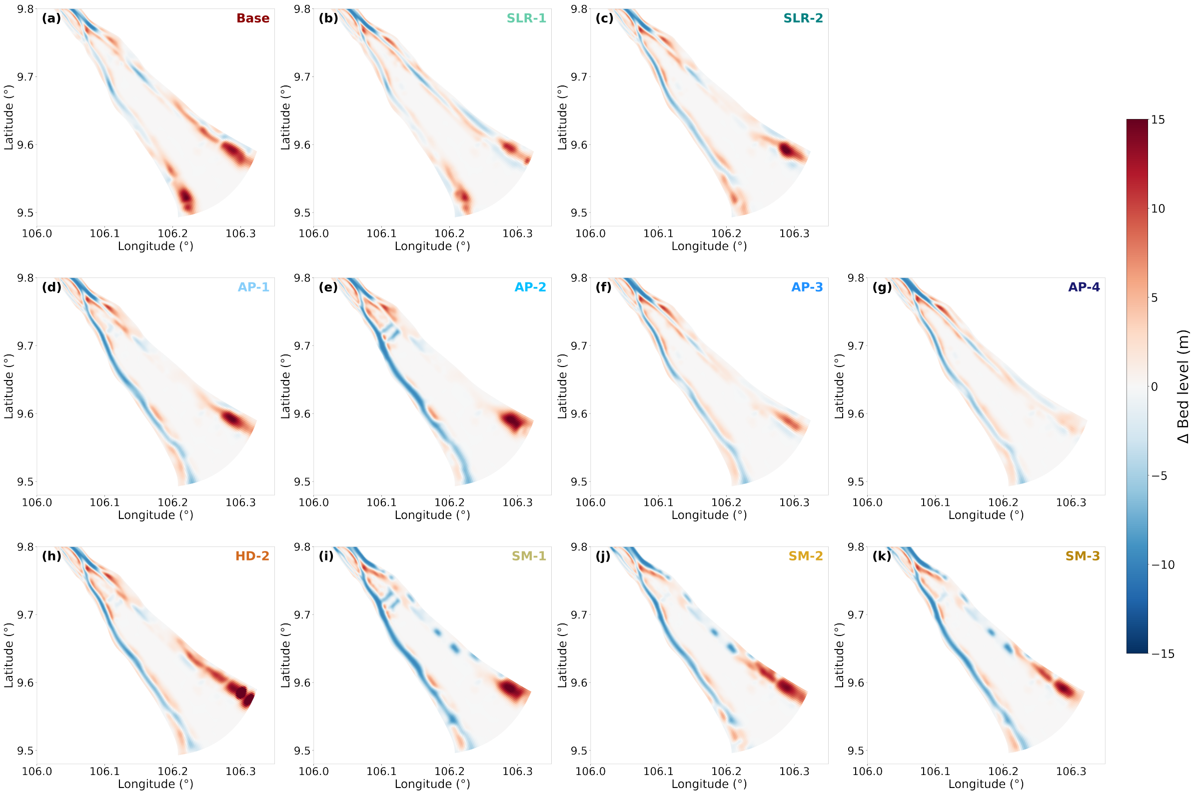

Figure 5.8: Total bed level change (2020 to 2050) for every scenario

5.4. Bifurcation dynamics

5.4.1. Bifurcation symmetry

The cumulative discharge curve (Figure 5.10) shows the temporal evolution of discharge partitioning at the bifurcation. Figure 5.9 presents a schematic of the bifurcation in the system. For the base scenario, the curve indicates that after the spin-up period (until $\sim$ 2025), the Dinh An branch dominates for about ten years, after which the Tran De branch becomes dominant until 2050.

After the spin-up phase (for most scenario runs until $\sim$ 2030), a clear difference in response between channels becomes visible for every scenario. Under the near-future altered precipitation scenarios, Tran De initially receives a larger share of the discharge, but the imbalance diminishes with increasing inflow (AP-3) and finally shifts toward a larger share for Dinh An under the highest inflow (AP-4). A flattened hydrograph (HD-2) follows a trajectory similar to AP-2, with a preference toward Dinh An.

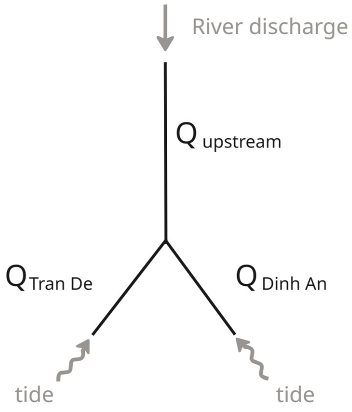

Figure 5.9: Schematization of the bifurcation

The sea-level rise (SLR) scenarios indicate that under sea-level rise alone (SLR-1), Dinh An receives slightly more flow than Tran De, while when subsidence is included (SLR-2), the distribution becomes more balanced. This suggests that higher downstream water-level forcing reduces asymmetry at the bifurcation. The sea-level rise (SLR) scenarios indicate that under only sea-level rise (SLR-1) Dinh An receives slightly more flow than Tran De, while when subsidence is included (SLR-2) the distribution becomes more balanced, suggesting that higher downstream water-levels reduces asymmetry at the bifurcation. Under the sand mining scenario with the lowest extraction rate (SM-1), a strong asymmetry appears, with Dinh An receiving a much larger share of the discharge. This imbalance disappears with increasing sand mining rates (SM-2 and SM-3) show a more balanced partitioning, with a slight preference toward the Tran De channel.

Compared to the base, slight discharge increases (AP-1, AP-2), discharge flattening (HD-2), and low extraction (SM-1) increase asymmetry. In contrast, large discharge increases (AP-3, AP-4), high water-level rise (SLR-2), and high extraction (SM-2, SM-3) produce discharge distributions that are similar to or more symmetric than the base.

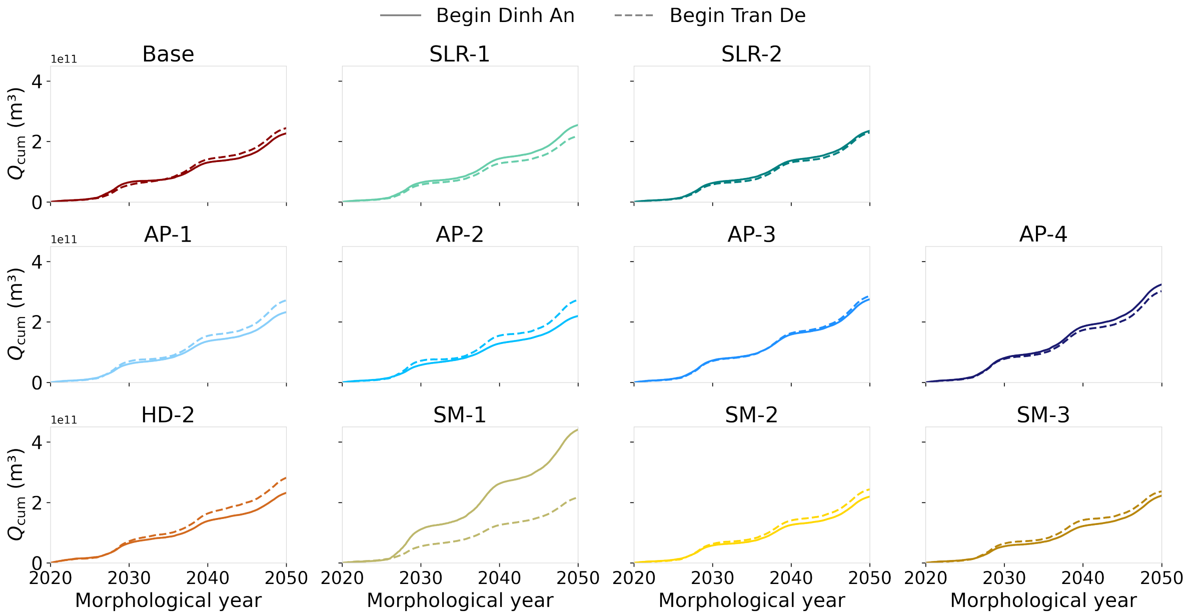

Figure 5.10: Cumulative Discharge for begin sections of the Dinh An and Tran De channels per scenario

The asymmetry index (Ψ) quantifies how discharge and sediment partition at the bifurcation. Values near 0 indicate symmetric partitioning, while larger magnitudes $|\Psi|$ reflect stronger asymmetry. The sign identifies the dominant branch: $\Psi > 0$ denotes dominance toward Tran De, and $\Psi < 0$ toward Dinh An. Section 2.3.2 provides the formal definitions, and Appendix H shows the full temporal evolution.

The asymmetry indices (Table 5.1) show that discharge partitioning is generally good, with Ψ_Q between -0.05 and 0.17, indicating near-symmetric conditions that are relatively insensitive to model modifications. The largest deviations occur under SM-1 (-0.48) and AP-2 (0.27), which are also reflected in the cumulative discharge curves (Figure 5.10). Higher discharges (AP-3 and AP-4) and higher downstream water levels (SLR) produce symmetric results close to the base conditions. Seasonal differences are minor, with the highest difference of 0.10 occurring under a flattened hydrograph (HD-2).

Sediment partitioning is consistently more asymmetric ($\Psi_S \approx -0.80$ to 0.61) and more sensitive to forcing. Higher discharge input and downstream water-level rise (AP-3, AP-4, SLR-2) show the most symmetric results, but still less balanced than the base conditions, whereas anthropogenic drivers strongly intensify asymmetry, with SM-1 showing the most extreme imbalance. Seasonal variability is also larger for sediment than for discharge, though no consistent seasonal pattern emerges across scenarios.

Overall, discharge partitioning remains stable and only weakly affected by forcing, while sediment transport shows strong and scenario-dependent responses, underscoring the higher sensitivity of sediment dynamics at the bifurcation.

Table 5.1: Asymmetry indices (Ψ) at the bifurcation, low-flow (Jan–Jun), and high-flow (Jul–Dec).

	Base	**AP-1**	**AP-2**	**AP-3**	**AP-4**	**HD-2**	**SLR-1**	**SLR-2**	**SM-1**	**SM-2**	**SM-3**
$\Psi_{Q,\text{all}}$	-0.01	0.15	0.27	0.04	0.02	0.13	-0.05	0.04	-0.48	0.11	0.17
$\Psi_{Q,\text{low}}$	0.01	0.12	0.24	0.04	0.04	0.07	-0.03	0.05	-0.48	0.11	0.16
$\Psi_{Q,\text{high}}$	-0.02	0.16	0.30	0.04	0.01	0.17	-0.06	0.03	-0.48	0.12	0.18
$\Psi_{S,\text{all}}$	-0.04	0.40	0.61	0.20	-0.15	0.48	-0.45	0.20	-0.80	0.34	0.51
$\Psi_{S,\text{low}}$	0.00	0.31	0.59	0.24	-0.17	0.30	-0.40	0.20	-0.84	0.17	0.40
$\Psi_{S,\text{high}}$	-0.07	0.45	0.62	0.18	-0.13	0.59	-0.48	0.20	-0.77	0.45	0.58

5.4.2. Bifurcation stability

It should be noted that a full stability assessment of a tidally influenced bifurcation requires evaluation on tidal timescales (see Section 2.3.2). Given the focus on the long-term sediment dynamics of the Song Hau estuary, only weekly outputs are analysed to maintain reasonable runtimes for the scenario runs. Therefore, the normalised cumulative sediment bias over time (Figure 5.11) is used as an indicator of bifurcation stability. The bias represents the cumulative difference in sediment transport between the two distributaries, normalised by the total transported load. Values close to zero indicate balanced partitioning, while magnitudes close to one indicate dominance of one branch. A positive bias corresponds to Tran De, and a negative bias to Dinh An. Formal definitions are provided in Appendix H.2.1.

Across all scenarios, clear disturbances appear at the beginning of the simulation period (the spin-up phase) and tend to disappear around 2025–2030. Under base conditions, after $\sim$ 2035, equilibrium in sediment partitioning is reached with a preference for the Dinh An branch. The elevated water level scenarios also stabilise after $\sim$ 2035 with a slight preference for the Dinh An branch. Under sea-level rise alone, this preference becomes more pronounced, and when subsidence is included, this equilibrium comes very close to 0, but still favours Dinh An, indicating a relatively symmetric sediment partitioning.

The behaviour of discharge due to altered precipitation varies widely. The first near-future scenario (AP-1) shows the most equal sediment partitioning, balancing around 0 after the spin-up phase, while the more extreme near-future projection (AP-2) shows a pronounced favouring of the Tran De channel, highlighting its extreme deviating response. The higher discharge increases (AP-3, AP-4) show a more similar response to each other, with a slight preference for Dinh An, similar to base conditions. The curves become very flat after spin-up, indicating a stable sediment partitioning regime. The induced discharge flattening due to hydropower dams (HD-2) shifts the favour towards Tran De, compared to base conditions, with fluctuations continuing throughout the simulation. Interestingly, small changes in the discharge time-series, such as slight increases or changes in the hydrograph, result in shifts to a different sediment partitioning equilibrium.

In the sand mining scenarios, significant changes in equilibrium are also observed. Extreme favouring of one branch occurs. Under slight extraction rates, Dinh An is strongly favoured, but with increased extraction rates, a pronounced favoring of Tran De is observed. Scenarios SM-2 and SM-3 show a similar response, though SM-3 shows a slightly stronger preference for Tran De, suggesting that higher extraction rates cause Tran De to attract more sediment.

Overall, initial adjustments occur in the sediment bias curve, but under most scenarios, the system settles into a steady partitioning regime. This stability develops earlier under climate change drivers compared to anthropogenic ones. The visual impression of stability is supported by the autocorrelation analysis of symmetry indices (Appendix H.2.2), which shows a rapid loss of memory in most scenarios, confirming the stable dynamics.

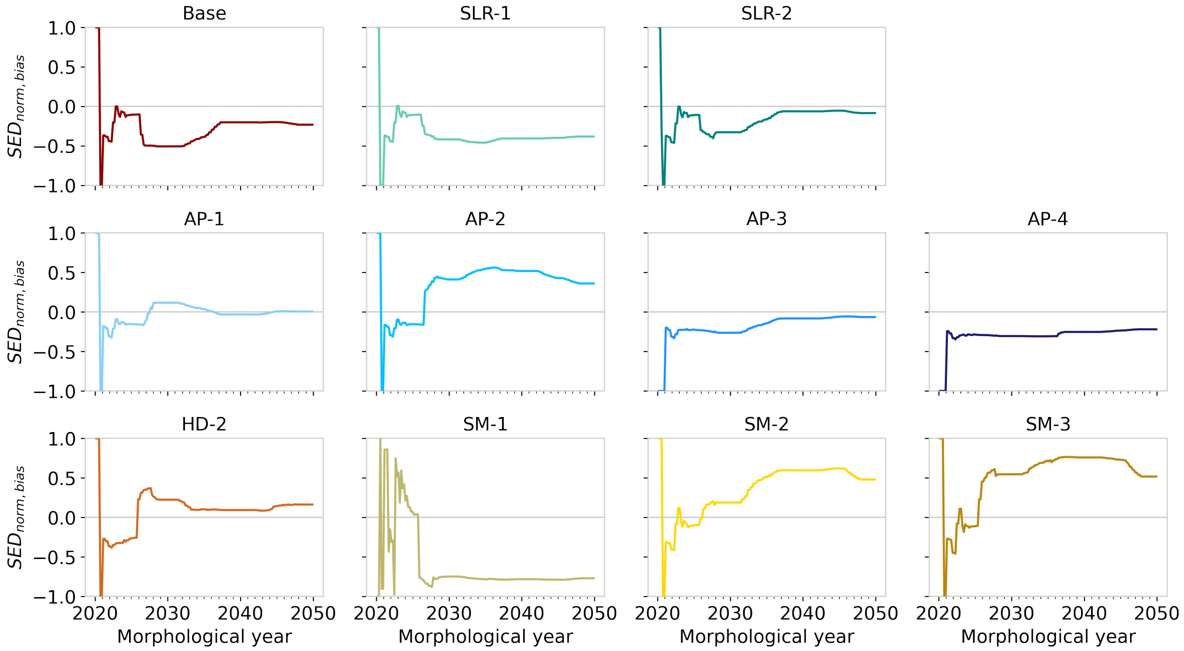

Figure 5.11: Normalised cumulative sediment bias (-): $dS_{norm,cum} > 0$ Tran De dominance, $dS_{norm,cum} < 0$ Dinh An dominance

6

Discussion

6.1. Overview

This discussion interprets the results in relation to the main research question, which examines future sediment dynamics under climatic and anthropogenic drivers through the Dinh An and Tran De distributaries. It first presents an analysis of each driver individually, followed by a cross-scenario synthesis, an assessment of limitations and uncertainties, and concludes with a reflection on the broader implications of the findings.

6.2. Climate change drivers

6.2.1. Altered precipitation

Under slight discharge increases (AP-1, AP-2), Tran De initially captures a larger share of the flow compared to Dinh An, intensifying the imbalance relative to the base scenario. At higher discharges (AP-3, AP-4), this routing becomes more balanced, with both water and sediment partitioning showing a trend toward greater symmetry. While the asymmetry index of sediment load index (Ψ_s) indicates a worsening compared to the base up to AP-3, the cumulative sediment bias improves under the higher discharge cases (except AP-2). For AP-4, the high-flow season shows better symmetry compared to the base conditions, though slightly worse in the low-flow season. The corresponding sedimentation–erosion patterns also become more balanced under higher discharges relative to the base conditions.

This tendency toward increased symmetry under higher discharges is consistent with Hackney et al. (2018) [32], who observed that flow partitioning at river-dominated bifurcations becomes more symmetrical during high-flow seasons but unstable during low-flow seasons. Szupiany et al. (2012) [74] and Zolezzi et al. (2006) [92] likewise reported improved bifurcation symmetry under higher discharges. A comparable mechanism is described by Iwantoro et al. (2020) [35], who showed that in tide-influenced bifurcations, higher relative river discharge reduces the influence of tidal backflow and sediment redistribution, thereby maintaining more symmetric channel morphology and sediment transport. Together, these findings suggest that high-discharge scenarios drive a more stable and balanced partitioning at the Song Hau bifurcation. This more balanced partitioning regime results in more efficient and predictable sediment delivery to the coastal zones, as it reduces the formation of hotspots in erosion or deposition, which could otherwise disrupt the uniform export of sediment to the sea. This consistent sediment transport supports long-term stability in delta morphology and coastal ecosystems.

6.2.2. Sea-level rise

Under sea-level rise only (SLR-1), deposition is more concentrated in the downstream segments than in the base case, but with lower overall magnitudes. Relative sea-level rise (SLR-2) produces stronger deposition in the downstream segment of Dinh An, exceeding the base, while deposition in Tran De is reduced. This suggests more sediment is retained within the system, decreasing export to the sea. Discharge routing remains largely symmetric, with a slight dominance of Dinh An over Tran De, as in the base case, and symmetry improves further under SLR-2, enhancing the base conditions. A similar trend is observed for sediment routing, where downstream partitioning becomes more balanced with higher water levels. This is also reflected in the cumulative sediment bias, which shows a more symmetric outcome under SLR-2 compared to the base conditions.

These findings are consistent with earlier studies highlight the role of sea-level rise and subsidence in modifying distributary morphology and sediment trapping. Allison et al. (2017) [5] showed that accelerating sea-level rise modifies estuarine circulation and sediment-trapping efficiency in the Mekong distributaries, while Van et al. (2012) [83] demonstrated that sea-level rise leads to backwater effects. This can be understood as higher downstream water levels that reduce flow velocities and trigger sediment deposition, which in turn results in more symmetric partitioning. Similar insights are provided by Leonardi et al. (2015) [41] and Esposito et al. (2020) [27], who note that increased downstream water levels suppress tidal dominance and extend backwater reaches, stabilizing flow division and sediment routing. The strong response to SLR-2 also aligns with the findings of Minderhoud et al. (2019) [49], who highlighted the Mekong Delta's extreme sensitivity to sea-level rise due to its low elevation.

6.3. Anthropogenic drivers

6.3.1. Sand mining

For the sand mining (SM) scenarios, extraction occurs mainly in the Dinh An branch. Based on bifurcation theory, lowering the bed in one branch reduces head loss at the node and makes that branch hydraulically more attractive, thereby drawing a larger share of the discharge [62, 63, 23]. Because suspended-sediment flux scales as $F_{\text{sus}} = Q\,C$ and C typically increases with Q (rating relation $C = a\,Q^b$ with $b > 0$), the branch that gets more flow (Q) also carries more than its share of suspended sediment [64]. Deepening further increases velocity and shear, which increases bed load transport capacity and further shifts total sediment transport toward the lowered branch [46]. The other branch receives less water, accumulates sediment, and may gradually disconnect from the main channel.

The model outcomes, however, reveal a different response. At the lowest extraction rate (1 Mt/yr), Dinh An shows strong dominance in both discharge and sediment partitioning ($\Psi_Q = -0.48$ and $\Psi_S = -0.80$, aligning with theoretical expectations. Most of the flow is directed toward this branch, while Tran De receives less water and sediment, resulting in increased deposition in its downstream segment. As extraction rates increase (2 and 4 Mt/yr), the dynamics shift: Tran De becomes relatively more dominant in both discharge and sediment transport, and at the highest extraction rate it even acts as a net exporter of sediment to the sea (sediment budget of -4 Mt over 2020-2050). In contrast, deposition in the lower segments of Dinh An becomes more pronounced and extends farther inland, with this trend intensifying at higher extraction rates (positive sediment budget of 25 Mt over 2020-2050). Consistently, greater asymmetry is observed in discharge and sediment load, as reflected in the cumulative sediment bias, which indicates dominance of Tran De.

These findings reflect a non-linear response in which initial bed lowering increases Dinh An's dominance, but further extraction reduces its relative role and amplifies Tran De's contribution. If the imposed bed level difference is relatively small, other factors, such as downstream boundary conditions, sediment supply variability, tidal asymmetry, or hydrodynamic connectivity, can override the expected dominance effect [23]. In particular, tidal rivers can stimulate sediment intrusion from the sea to land because lower bed levels reduce hydraulic resistance to tidal inflows and promote sediment trapping [64, 45]. This could clarify the increased deposition in the downstream segments of the Dinh An channel, while Tran De gradually shifts to becoming a net exporter of sediment to the sea, Dinh An silts up and becomes less effective at transporting sediment.

It should be noted that the maximum extraction rate (4 Mt/yr) is constrained by the upstream SSC used to force the model and is likely low for actual sand mining in the Song Hau. According to the literature (Section 2.2.4), reported delta-wide extraction spans a wide range, with mostly much higher values. If the Song Hau accounts for roughly half of delta-wide mining, 4 Mt/yr translates to $\sim$8 Mt/yr at the delta scale, close to the lowest published estimate. Consequently, the simulated magnitudes of erosion–deposition and the shifts in discharge and sediment partitioning should be interpreted as minimum responses: at higher, more realistic extraction rates, thresholds are likely crossed earlier and with greater magnitude, and morphological adjustment is stronger. Overall, the combined variability in discharge forcing, tides, sediment supply, and evolving morphology, together with the wide uncertainty in reported extraction rates, makes the effect of increasing extraction rates difficult to predict in tide-influenced branches.

6.3.2. Hydropower dams

Only the flattening of the discharge hydrograph is considered to analyse the effect of hydropower dams, because any reduction in SSC at the upstream boundary seems to have negligible effects. The model response is dominated by hydrodynamic conditions together with the prescribed sediment properties, not by the SSC time-series forcing. A more detailed explanation and justification are provided in the Model Limitations and Uncertainties section 6.5.2.

The scenario with a flatter discharge regime (decreased Q_{wet}, increased Q_{dry}) shows several key differences compared to the base case. Tran De emerges as the dominant branch, with higher relative discharge and sediment transport than Dinh An. The cumulative discharge (Q_{cum}) was already larger through Tran De in the base case, but this dominance becomes more pronounced under the flatter hydrograph. Morphodynamic responses follow from this shift. Tran De erodes in its upstream segments due to more sustained hydraulic forcing at the bifurcation entrance [92, 62], while Dinh An accumulates sediment downstream as reduced peaks limit its export capacity. Similar upstream–downstream contrasts have been observed in field and laboratory studies [74, 32].

The asymmetry indices (Ψ_Q and Ψ_S) confirm this picture. Ψ_Q rises slightly from -0.01 under base to 0.13 under HD-2, indicating a modest intensification of Tran De's discharge share. Ψ_S, however, increases more strongly from -0.04 to 0.48. As discussed in Section 6.3.1, sediment flux scales nonlinearly with discharge ($Q_s \propto Q^b$ with $b > 1$). In the base case, this nonlinearity allowed Dinh An to profit from occasional high-flow events and capture a slightly larger sediment share. With a flatter hydrograph, such events are damped, so Tran De secures a consistently larger fraction of sediment, leading to a clearer asymmetry. This mechanism is consistent with observations that discharge variability strongly controls bifurcation partitioning [64, 24, 11].

Finally, the cumulative sediment bias reflects the same shift: from slightly in favor of Dinh An in the base case ($dS_{norm,cum} \approx -0.25$) to favoring Tran De in the flatter scenario ($dS_{norm,cum} \approx 0.20$), although its absolute magnitude decreases because overall sediment throughput is lower without extreme flood events. These results indicate that a flatter hydrograph enhances the dominance of Tran De, where more sediment is exported to the sea, suggesting that future changes in the flow regime could intensify existing asymmetries between distributary channels and affect the long-term morphology of the delta.

6.4. Cross-scenario comparison

Considering the variety of drivers, a number of systematic patterns emerge when comparing all scenarios together. Climate-related scenarios (altered precipitation, sea-level rise) generally promote more balanced outcomes at the bifurcation, while anthropogenic modifications (sand mining, discharge flattening due to hydropower) tend to intensify asymmetries. Model modifications further divide into discharge forcing (precipitation, hydropower), water-level forcing (SLR, RSLR), and bed-level forcing (sand mining), each leaving a specific response on sediment transport and bifurcation symmetry and stability.

In the discharge-forcing group, increased inflow through precipitation shifts the system toward greater symmetry at high discharges ($\Psi_Q \approx 0.04 - 0.02$ for AP-3, AP-4 respectively) consistent with previous findings that flood seasons stabilise bifurcation dynamics. Conversely, reduced variability under a flatter hydrograph enhances the dominance of Tran De ($\Psi_Q \approx 0.13$, compared to base conditions: $\Psi_Q \approx -0.01$), suppressing the balancing role of extreme high flows. These outcomes highlight that the temporal structure of discharge, not only its magnitude, is a key control on bifurcation partitioning and sediment export to the sea, as a more stable discharge regime allows for more predictable sediment delivery.

In the water-level forcing group, sea-level rise consistently improves symmetry by reducing tidal influence and trapping sediment more evenly across branches ($dS_{norm,cum} \approx -0.01$) under relative sea-level rise). The more efficient trapping compared to base conditions results in slightly less sediment throughput to the coastal zone under relative sea-level rise. Increased sediment budgets (Fig. 5.6) relative to base conditions are observed for both Dinh An (+20%) and Tran De (+4%). This highlights the sensitivity of distributary partitioning to downstream boundary conditions.

In the bed-level forcing group, sand mining produces strongly nonlinear responses. At low extraction, Dinh An dominates as expected, but higher extraction reverses the balance, with Tran De becoming a net exporter of sediment. The amount deposited under base conditions in Tran De is now exported under the highest sand mining extraction rates, resulting in a 200% decrease in the sediment budget (Fig. 5.6). This underscores the potential for anthropogenic bed lowering to shift the system's response and and destabilize the bifurcation through feedbacks between hydraulics, sediment supply, and tidal interaction.

Across all scenarios, Dinh An maintains a positive sediment budget, while Tran De alternates between importing and exporting sediment depending on the forcing. Compared to base conditions, the sediment budget change in Tran De ranges from +259% to -594%, highlighting this variability. Asymmetry indices confirm that discharge partitioning is relatively stable ($\Psi_Q \approx -0.48$ to 0.27), showing only modest deviations from the base conditions, while sediment partitioning is more sensitive and amplifies asymmetries ($\Psi_S \approx -0.80$ to 0.61). Cumulative sediment bias curves (Fig. 5.11) further indicate that climate-driven scenarios, such as altered precipitation, settle into a stable regime after 2025–2030. However, anthropogenic drivers continue to cause deviations and increase variability.

Together, these results demonstrate that climate change drivers generally enhance sediment export to the sea, through both branches, while anthropogenic interventions reduce the efficiency of sediment export through Dinh An, promoting sediment export via Tran De. This is reflected in the sediment budgets (Fig. 5.6), for climate-drivers only decreases are observed in Dinh An (0 to -60%), whereas anthropogenic scenarios show mostly increases in Dinh An (+44% to +78%, except SM-1). In terms of bifurcation dynamics, climate drivers generally reduce asymmetries and stabilize sediment partitioning over the bifurcation ($\Psi_Q \approx -0.05$ to 0.04), while anthropogenic interventions amplify contrasts, leading to greater dominance of one branch and unpredictable shifts in responses ($\Psi_Q \approx -0.48$ to 0.17). The balance between discharge, water-level, and bed-level forcing ultimately determines whether the Song Hau bifurcation evolves toward greater symmetry or increased instability.

6.5. Model limitations and uncertainties

6.5.1. Data availability and boundary conditions

The limited availability of suspended sediment concentration (SSC) data poses a constraint for this research, as a complete time series is only available for the years 2016 to 2018 at the upstream boundary of Can Tho. For the hydrodynamic input, the most recent three-year time series (2020 to 2022) is used. Since the SSC data from 2016–2018 represent the most recent complete dataset, this results in a temporal misalignment. To solve this, a prediction of the SSC time series is conducted by applying rating curves (see Appendix B) to estimate SSC for the recent hydrodynamic period.

The scarcity of data also constrains the model domain. Extending the model boundaries further upstream or offshore is technically possible, but doing so would require more advanced and time-consuming approaches that are beyond the scope of this study. Upstream, the model is limited to the reliable monitoring station Can Tho. Extending further would require applying a tide-dependent time lag to the time series, as tidal influence still reaches this location. Extending the grid further downstream would require a tidal hydrodynamic model to convert the water level of Tran De into a reliable offshore boundary time series. These limitations increase the influence of boundary effects at both ends of the model, making the bifurcation itself the most reliable location for analysis.

At the downstream boundary, no SSC observations are available. Therefore, a simplified equilibrium condition with zero incoming sediment concentration is applied. In this approach, the sediment flux entering and leaving the boundary is assumed to be balanced, representing a steady-state situation with no net sediment import. While computationally efficient, this steady-state assumption does not capture the dynamic nature of sediment transport in a tidally influenced environment. It neglects processes such as tidal resuspension, backflow, and marine sediment intrusion, as well as the temporal variability associated with ebb and flood currents. Consequently, sediment input from the sea is likely underestimated, which could bias the sediment budget near the river mouth toward net export and reduce accuracy at the coastal boundary.

Furthermore, no SSC time series are available within the model domain itself. Consequently, calibration and validation of sediment concentrations can only be carried out on an order-of-magnitude basis by comparing the upstream input with concentrations in the focus area before the bifurcation, rather than through detailed spatial validation.

6.5.2. Sediment transport Formulation (Van Rijn, 2004)

In this study, the Delft3D SED-module uses the capacity-based sediment transport formulation of Van Rijn, 2004 (see Appendix C). This formulation determines the total transport q_{tot} based on hydrodynamic conditions, such as flow velocity and bed shear stress, along with sediment properties like grain size and density, rather than relying on prescribed suspended sediment concentration (SSC) values.

The aspect of upstream input SSC having no impact on the model can be seen in the cumulative inbound sediment volumes (see Appendix E.2), which show that the prescribed SSC at the upstream boundary does not directly translate into equivalent sediment inflow within the model domain. The actual flux at the upstream cross-section is significantly lower, indicating rapid adjustment towards an equilibrium concentration C_{eq} defined by the Van Rijn formulation. This equilibration explains the limited sensitivity of model results to variations in upstream SSC input.

Another aspect of the sediment transport formulation concerns the spin-up phase of sediment transport within the model. During the initial simulation period, time series of cumulative and instantaneous sediment fluxes show strong fluctuations. These reflect the equilibration of imposed concentrations and bed levels as the transport regime stabilizes. The sediment mass balances (Appendix E.3) confirm that such residuals occur over a wider, scenario-dependent range, rather than within a fixed period. Because erosion and deposition are path-dependent, this spin-up phase influences subsequent morphological development. Sediment and erosion budgets were therefore calculated over the full simulation period, including the spin-up phase. While this likely exaggerates the absolute magnitude of early erosion and deposition, the period cannot be excluded, as it directly affects later system evolution. Nevertheless, as all scenarios are subject to spin-up behaviour, the long-term trends and relative differences between scenarios remain meaningful, even if the absolute timing and magnitude of the spin-up are not robust.

Lastly, the Van Rijn (2004) formulation also produces artefacts in the long-term morphodynamic output, including unrealistically deep channels and excessive sedimentation at the river mouths. Such behaviour is a well-documented side effect of capacity-based transport formulations [58]: erosion tends to be overestimated in high-energy channels, while deposition is exaggerated in zones with sharp velocity reductions, such as estuarine mouths. As shown by Baar et al. (2019) [6], this artefact originates from an imbalance between channel incision and downslope sediment transport, since the Van Rijn formulation accounts for slope effects only on the bed-load fraction. Therefore, sediment tends to accumulate in a single grid cell, failing to account for the lateral distribution of sediments. Therefore the spatial pattern of sedimentation-erosion is should not be interpreted literally. While the magnitudes of erosion is biased, the consistent occurrence of hotspots across scenarios provides meaningful insight into the dominant morphological responses of the system.

Given the known limitations and uncertainties of the sediment transport formulation, the results should only be interpreted primarily in a relative sense. The model is most reliable for capturing broad-scale spatial patterns of erosion and deposition and for comparing differences between scenarios, rather than predicting absolute sediment fluxes or channel changes. Within this scope, the simulations provide valuable insights into highlighting trends and cross-scenario comparisons.

6.5.3. Simplifications

The model setup required several simplifications, which should be considered when interpreting the results. The main ones are: (a) exclusion of fine-sediment classes, (b) exclusion of salinity, (c) weekly temporal resolution of outputs, (d) exclusion of wind forcing, (e) exclusion of floodplains, (f) exclusion of embankment structures and (g) use of a structured grid.

The exclusion of fine sediments and salinity are closely related. In the Song Hau estuary, fines dominate during the dry season and are strongly affected by salt intrusion and estuarine circulation [5, 13, 56].

By excluding both, the model does not capture processes such as flocculation, mud–sand interactions, and density-driven landward transport of fines. As a result, the outputs emphasise sand-dominated export during high flows but underestimate dry-season deposition, cohesive sediment trapping, and seasonal contrasts. This simplification likely biases the results toward overestimating net sediment export to the shelf.

Furthermore, the temporal resolution of weekly outputs smooths out short-term tidal variability. Field studies show that sediment transport is strongly phase-dependent, with Dinh An ebb-dominated and efficient at sand export, while Tran De is flood-dominated and subject to fine import [5, 89]. Such tidal-scale asymmetries are not resolved, which explains why the model results show more balanced partitioning than observed.

Other simplifications include the exclusion of wind forcing, which may underestimate surface-driven flows and flow reversal during the dry season, and the exclusion of floodplains, which neglects overbank flooding and sediment storage during high flows. The exclusion of embankment structures also results in unrealistic flooding of islands, affecting the model's ability to predict sediment deposition accurately. Finally, the use of a structured grid improves computational efficiency but reduces flexibility in representing complex channel–island geometries, potentially affecting local flow paths and sediment routing, particularly in narrow or curved sections of the river.

All in all, the simplifications are both necessary and justified for assessing long-term effects. Including additional processes, characteristics, and complexities would significantly increase the computational run time, making the choice to neglect some of these elements reasonable for long-term studies. While these simplifications introduce certain limitations, they allow for a more manageable and efficient analysis of the broader, long-term trends, which is the primary focus of this study.

6.6. Broader Implications

The results of this study have implications that extend beyond the scale of the Song Hau bifurcation. First, the findings highlight the importance of the sediment balance in the Mekong Delta. Sand mining and hydropower regulation make the system more prone to sediment trapping, shifting the balance between export to the sea and storage within distributaries. Specifically, the Dinh An branch acts as a sediment sink, with increases in sedimentation of +44% to 78% compared to base conditions (Fig. 5.6). This reduces the sediment available to sustain the delta's coastal zone, limiting its capacity to keep pace with subsidence and sea-level rise, thereby increasing the risk of coastal erosion, as ecosystems like mangroves are highly sensitive to sediment fluctuations. These changes alter coastal morphology and reduce ecosystem extent and stability, leaving the delta more exposed to storms and sea-level rise. The strong link between upstream river dynamics and downstream coastal resilience underscores the need for delta management strategies that integrate riverine and coastal processes, both in the Mekong and in deltas worldwide. Since such interventions are common across deltas worldwide, better understanding their scale of impact is crucial for effective future protection and management strategies.

Second, the findings emphasise the importance of bifurcation symmetry and stability for system resilience, highlighting the role of sediment partitioning in shaping downstream impacts. Instabilities at the bifurcation can lead to altered sediment pathways, channel abandonment, and loss of navigability, which may result in sediment deficits downstream and increased riverbank erosion. In the case of human-induced scenarios, higher asymmetry indices are observed, with sedimentation hotspots occurring in the downstream segment of Dinh An (see Figure 5.8), and high sediment biases noted (SM-1 > -0.8, SM-2, SM-3 > 0.6). These shifts can further exacerbate issues such as flooding, reduced navigability, and altered hydrological patterns, putting local communities, agricultural land, and infrastructure at greater risk, underscoring how distributary-scale morphodynamics translate into socio-economic impacts.

Together, these broader implications demonstrate that managing sediment fluxes is not only essential for bifurcation stability but also for sustaining the wider delta system and its ecosystems under increasing human and climatic pressures.

7

Conclusion

This study assesses how climate and human-induced drivers shape long-term, sand-dominated sediment transport in the tidally influenced zone of the Song Hau distributary system: the estuary. It compares altered precipitation (AP) with higher discharges, sea-level rise (SLR) with increased downstream water levels, sand mining (SM) with extraction at multiple locations, and hydropower-induced discharge flattening (HD), which results in lower discharge peaks in the wet season and higher flow in the dry season. It demonstrates how variations in discharge magnitude, downstream water levels, and bed-level changes affect sediment transport and the bifurcation behaviour from 2020 to 2050. The bifurcation behaviour is characterised by symmetry, referring to the distribution of flow between the two branches, and stability, describing the ability of the bifurcation to reach and maintain equilibrium over time.

These conclusions should be understood within the scope of the model, which focuses on comparing the relative behaviour of different scenarios in terms of sedimentation-erosion patterns, discharge and sediment distribution across the bifurcation, and sediment transport over time, rather than on exact magnitudes. This approach accounts for the limited calibration and validation of sediment transport and the limitations of the Van Rijn (2004) capacity-based transport formulation, where sediment transport is determined based on flow conditions and sediment properties like grain size and density. Despite these limitations, the differences between scenarios remain clear and consistent.

In terms of sediment transport, climate forcing shifts the system toward a more balanced regime. Higher discharge increases export capacity and reduces sedimentation compared to the base conditions, as reflected in sediment budget reductions under the highest discharge increase (Dinh An -60%, Tran De -166%), leading to a more balanced erosion-sedimentation pattern. Elevated downstream water levels cause the river's flow to slow down, amplifying backwater effects. This results in more sedimentation at the river mouths but less inland spread compared to base conditions. The system reacts more drastically under human-induced influences. A flattened hydrograph from hydropower dam operations reduces the disproportionate contribution of short, high-flow periods to sediment export (since $Q_s \propto Q^b$, $b > 1$), allowing Tran De to capture a more consistent share of sediment, while Dinh An tends toward downstream accumulation. Increased sand mining extraction rates turn Dinh An into a sediment sink, with sediment budgets increasing by +75%, drawing more sediment from the sea and intensifying estuary circulation. As a result, Tran De becomes a sediment exporter, with export rates matching the sedimentation observed under base conditions.

Concerning bifurcation behaviour, the distribution of water and sediment between the two river branches shows very different behaviour. The distribution of water is relatively stable under different model modifications: the asymmetry index (Ψ_Q) varies only modestly between -0.01 and 0.17, meaning that neither branch carries significantly more or less water than the other. This pattern does not change much over time or across scenarios. The sediment distribution, however, is much more sensitive, with an asymmetry index (Ψ_S) ranging from -0.45 to 0.61. Small changes in forcing therefore lead to disproportionately large changes in sediment storage and export. The base conditions exhibit the most balanced system in terms of symmetry, with the lowest asymmetry indices for both discharge and sediment (closest to 0), indicating an almost equal division of water and sediment between the two branches. Climate-driven scenarios with high flows and elevated water levels approach this symmetric condition over a relatively short period of time, after which it stays in one equilibrium, indicating a stable steady state of the system. In contrast, anthropogenic forcings lead to higher asymmetry indices, pushing the system away from this equilibrium. Under a flattened hydrograph, asymmetry shifts both water and sediment towards Tran De, while sand extraction shows a nonlinear response, indicating the presence of a threshold: at modest bed lowering, Dinh An dominates, but at higher extraction rates, Tran De becomes dominant. Tran De becomes the more dominant branch in terms of flow and sediment distribution when the behaviour of the bifurcation is disturbed, as occurs under human interventions.

To conclude, climate-driven changes generally stabilise the system, promoting a more symmetric distribution of river flow and sediment, while human-induced modifications tend to intensify asymmetries over the bifurcation. Under such interventions, Tran De is prone to becoming the dominant branch, taking most of the water and sediment, which puts Dinh An at risk of potential silting up. This underscores the importance of regulating discharge dynamics and controlling sand mining extraction rates to maintain a stable sediment distribution, which is crucial for the resilience of the system and for sustaining sediment supply to the wider delta.

8

Recommendations

8.1. Overview

Further research increases both the potential of the Delft3D model for the Song Hau estuary and the understanding of this region within the wider Mekong Delta system. This chapter presents recommendations for future research, structured as follows: first, model improvements and validation, and then wider system-oriented recommendations.

8.2. Model Improvements

- **Domain & boundaries**: Extending the Delft3D model domain further downstream into the coastal zone improves tidal boundary representation and reduces boundary-induced disruptions. In the current set-up, the open boundary lies too close to the river mouth, where tides, waves, and sediment interact in complex ways. Because these processes are not fully captured, the model depends on prescribed boundary conditions that are uncertain and difficult to validate due to limited data. Extending the domain farther offshore allows the assumption of a near-zero net sediment flux at the open boundary, simplifying boundary treatment and preventing artificial sediment gain or loss. This adjustment reduces numerical artefacts and better represents tidal dynamics and sediment exchange between the estuary and the sea. Although a larger domain increases computation time and requires more detailed bathymetry, it remains a high-priority improvement for increasing the reliability of sediment flux estimates in the Song Hau estuary.
- **Sediment transport formulation**: Revising the sediment-transport formulation is recommended to reduce the unrealistic channel incision associated with the Van Rijn (2004) predictor, as described in Section 6.5.2. Testing alternative predictors such as Engelund–Hansen, Meyer-Peter–Müller, or Soulsby–Van Rijn, and refining the slope-effect parameterisation, could reduce these artefacts and result in more realistic morphodynamic behaviour. This improvement is expected to result in more physically consistent sediment fluxes in the Song Hau estuary.
- **Spin-up procedure**: Introducing a spin-up period for suspended sediment concentrations is recommended to stabilise the model before applying the scenario-specific forcing. Adding a start-up year prior to the three-year simulation allows suspended sediment to reach dynamic equilibrium, preventing the unrealistic fluctuations observed at the start of the runs (see Fig. 5.2). During this period, identical forcing should be applied across all scenarios to ensure comparable initial conditions. This procedure removes early SSC adjustment effects and improves the consistency of cross-scenario comparisons.
- **Process expansion**: Including additional physical processes is recommended to reduce the influence of model simplifications discussed in Section 6.5.3. In particular, adding fine-sediment fractions and salinity dynamics would improve the model's representation of estuarine processes. Fine sediments strongly affect settling, resuspension, and flocculation, while salinity influences density-driven circulation and stratification. Their interaction is essential for accurately reproduc-

ing sediment trapping and deposition patterns near the river mouths. Implementing these processes would therefore provide a more realistic basis for analysing sediment exchange between the estuary and the coastal zone.

- **Mesh & bathymetry representation**: Applying a flexible mesh configuration improves the spatial representation of island and coastline curvatures within the study area. Delft3D Flexible Mesh allows smoother transitions between channels and higher-elevation zones. It also better resolves local bathymetric gradients, resulting in a more realistic flow distribution and sediment exchange around the islands. However, flexible grids do not necessarily improve sediment transport performance [2], as numerical diffusion and cell-size effects may still dominate. The main advantage of this approach lies therefore in improved geometric accuracy and numerical stability rather than a direct gain in transport performance.

8.3. Model Validation

Future modelling efforts would benefit from improved data availability, particularly for bathymetry and suspended sediment concentration (SSC), which are currently outdated and limited in this study area.

- **Bathymetry**: An up-to-date bathymetry dataset is essential for reliable model performance. Bathymetry forms the foundation of the hydrodynamic model, and outdated surveys cause significant uncertainty, particularly in dynamic estuarine systems like the Song Hau. Regular resurveying is recommended, with a horizontal resolution on the order of tens of metres to adequately represent channel geometry. A combination of full-area multibeam surveys every few years and more frequent cross-sectional surveys along characteristic locations, including cross-sections upstream of the bifurcation where morphological variability is high due to island bars, and several cross-sections within the two distributary branches, would sufficiently capture morphological evolution.
- **Suspended sediment concentration (SSC)**: Reliable SSC data are critical for model verification, as suspended sediment transport is highly variable in tidally influenced areas. Observations should ideally be continuous, with a temporal resolution on the order of hours to capture tidal variability. SSC data collection at existing monitoring stations (see Figure 2.2) would make implementation easier and already cover a large part of the spatial domain. In addition, one observation point in the Dinh An branch is recommended to investigate branch-specific variability. Such a setup would allow quantification of both temporal fluctuations and spatial gradients in SSC. Combining in-situ sensors with satellite-based remote sensing could provide a cost-effective data source for future model validation. Expanding SSC monitoring capacity in this way would substantially improve the modelled sediment transport.

8.4. Wider Recommendations

- **Tidal-influenced bifurcation behaviour**: Most bifurcation research focuses on river-dominated systems, while tidal-influenced bifurcations remain understudied. The partitioning of water and sediment under varying tidal and discharge conditions is still poorly understood and largely limited to specific case studies [64]. Therefore, case-specific investigations of the Mekong Delta's tidal bifurcation are needed to assess the current stability of this node and to improve understanding of how resilient the system is to changing fluvial, tidal, climatic, and anthropogenic forces.
- **Human interventions**: To reduce risks to the system, human interventions should be more strictly regulated and monitored. This study indicates that human drivers can amplify system responses in unpredictable ways, particularly affecting discharge and sediment division at the bifurcation. Such changes may alter branch dominance and have large-scale impacts on the stability of the delta.
- **Mangrove loss**: It is recommended to investigate mangrove loss at larger spatial and temporal scales to capture the full range of interacting processes. These include long-term changes in sediment delivery from all river mouths of the Mekong Delta (including the Song Hau), subsidence of the delta plain, and shifts in alongshore sediment transport that together shape coastal stability. The present model can serve as one element within such broader-scale investigations, for example by being expanded or coupled with existing coastal models to quantify the sediment contribution from the Song Hau.

References

[1] 1TheGioi.vn. *Supply for the Chau Doc – Can Tho – Soc Trang Expressway Investment Project, Phase 1*. 2024. URL: `https://1thegioi.vn/soc-trang-khai-thac-them-mo-cat-song-phuc-vu-du-an-cao-toc-222921.html` (visited on 07/16/2025).

[2] F. M. Achete et al. "A 2-D process-based model for suspended sediment dynamics in the Sacramento–San Joaquin Delta". In: *Hydrology and Earth System Sciences* 19 (2015), pp. 2837–2857. DOI: `10.5194/hess-19-2837-2015`. URL: `https://doi.org/10.5194/hess-19-2837-2015`.

[3] Ministry of Agriculture and Rural Development (MARD). *Mekong River Delta Survey and Monitoring*. Tech. rep. Hanoi, Vietnam: MARD, 2019.

[4] Ministry of Agriculture and Rural Development (MARD). *Surveying erosion and sedimentation in the river system of the Mekong Delta from 2008 to 2011*. Tech. rep. Hanoi, Vietnam: MARD, 2011.

[5] M.A. Allison, H.D. Weathers, and E.A. Meselhe. "Bottom morphology in the Song Hau distributary channel, Mekong River Delta, Vietnam". In: *Continental Shelf Research* 147 (2017), pp. 51–61. DOI: `10.1016/j.csr.2017.05.010`.

[6] Anne W. Baar et al. "Critical dependence of morphodynamic models of fluvial and tidal systems on empirical downslope sediment transport". In: *Nature Communications* 10.4903 (2019), pp. 1–10. DOI: `10.1038/s41467-019-12753-x`. URL: `https://doi.org/10.1038/s41467-019-12753-x`.

[7] Báo Công Lý. *For the construction of Subproject 4 under the Chau Doc – Can Tho – Soc Trang Expressway Project, Phase 1*. 2024. URL: `https://baove.congly.vn/khoi-cong-khai-thac-mo-cat-tren-song-hau-phuc-vu-du-an-cao-toc-438486.html` (visited on 07/16/2025).

[8] Báo Nhân Dân. *For the construction of Subproject 4 of the Chau Doc – Can Tho – Soc Trang Expressway Project (East–West Expressway of the Mekong Delta)*. 2025. URL: `http://nhandan.vn/soc-trang-thong-qua-ho-so-tac-dong-moi-truong-mo-cat-so-11-post809386.html` (visited on 07/16/2025).

[9] Báo Sóc Trăng. *For the construction of Subproject 4 of the Chau Doc – Can Tho – Soc Trang Expressway (East–West Expressway of the Mekong Delta)*. 2025. URL: `https://baosoctrang.org.vn/tin-noi-bat/202506/thao-go-kho-khan-trong-khai-thac-cat-phuc-vu-du-an-cao-toc-e8c4cce/` (visited on 07/16/2025).

[10] Báo Sóc Trăng. *Supply for the Chau Doc – Can Tho – Soc Trang Expressway Project, Phase 1*. 2024. URL: `https://baosoctrang.org.vn/cac-du-an-dau-tu-xay-dung-cong-trinh-trong-diem-soc-trang/202408/khoi-cong-khai-thac-mo-cat-ms01-tren-song-hau-6383b58/` (visited on 07/16/2025).

[11] Maurizio Bolla Pittaluga, Rossana Repetto, and Marco Tubino. "Channel bifurcations in braided rivers: equilibrium configurations and stability". In: *Water Resources Research* 39.3 (2003), p. 1046. DOI: `10.1029/2001WR001112`.

[12] J.-P. Bravard, M. Goichot, and S. Gaillot. "Geography of sand and gravel mining in the Lower Mekong River. First survey and impact assessment". In: *EchoGéo* (2013), pp. 1–20. DOI: `10.4000/echogeo.13659`.

[13] J.-P. Bravard, M. Goichot, and H. Tronchère. "An assessment of sediment-transport processes in the Lower Mekong River based on deposit grain sizes, the CM technique and flow-energy data". In: *Geomorphology* 207 (2014), pp. 174–189. DOI: `10.1016/j.geomorph.2013.11.004`.

[14] G. Brunier et al. "Recent morphological changes in the Mekong and Bassac river channels, Mekong Delta: the marked impact of river-bed mining and implications for delta destabilisation". In: *Geomorphology* 224 (2014), pp. 177–191. DOI: `10.1016/j.geomorph.2014.07.009`.

[15] F. A. Buschman et al. “Subtidal flow division at a shallow tidal junction”. In: *Water Resources Research* 46.12 (2010), W12513. DOI: `10.1029/2010WR009266`.

[16] Stimson Center. *Mekong Dam Monitor*. Retrieved from Stimson Eyes on Water. Stimson Center. Feb. 7, 2023. URL: `https://monitor.mekongwater.org/basin-wide-dams-and-connectivity/?v=1642195188734`.

[17] M. Coleman and O. K. Huh. *Major Deltas of the World: A Perspective from Space*. Tech. rep. Available at: `http://www.geol.lsu.edu/WDD/PUBLICATIONS/C&Hnasa04/C&Hfinal04.htm` (Accessed: 12 April 2012). Baton Rouge, LA, USA: Coastal Studies Institute, Louisiana State University, 2004.

[18] Mekong River Commission. *Overview of the Hydrology of the Mekong Basin*. Accessed: 2025-06-23. 2005. URL: `https://archive.iwlearn.net/mrcmekong.org/download/free_download/Hydrology_report_05.pdf`.

[19] Tra Vinh Province People’s Committee. *Assessment and forecast of flow regime (flow, water level, water quality) and erosion developments on Co Chien and Hau rivers in Tra Vinh province*. Tech. rep. Tra Vinh, Vietnam: Tra Vinh Province, 2023.

[20] Tra Vinh Province People’s Committee. *Survey, assessment and forecast of riverbank erosion in Tra Vinh province under the conditions of climate change - sea level rise*. Tech. rep. Tra Vinh, Vietnam: Tra Vinh Province, 2014.

[21] Floor Cornielje. “Modelling the sediment dynamics in the Vietnamese Mekong Delta using Delft3D”. MSc Thesis. Delft University of Technology, 2023.

[22] Deltares. *Delft3D-FLOW User Manual*. Version 3.15, The Netherlands. 2014. URL: `https://content.oss.deltares.nl/delft3d/manuals/Delft3D-FLOW_User_Manual_v3.15.pdf`.

[23] Lorenzo Durante et al. “Downstream Control on the Stability of River Bifurcations”. In: *Journal of Geophysical Research: Earth Surface* 129 (2024), e2023JF007548. DOI: `10.1029/2023JF007548`.

[24] Douglas A. Edmonds and Rudy Slingerland. “Stability of delta distributary networks and their bifurcations”. In: *Water Resources Research* 44.9 (2008), W09426. DOI: `10.1029/2008WR006992`.

[25] S. Eslami et al. “Tidal amplification and salt intrusion in the Mekong Delta driven by anthropogenic sediment starvation”. In: *Scientific Reports* 9 (2019), p. 18746. DOI: `10.1038/s41598-019-55018-9`.

[26] Somayeh Eslami et al. “Projections of salt intrusion in a mega-delta under climatic and anthropogenic stressors”. In: *Communications Earth & Environment* 2.1 (2021), p. 113. DOI: `10.1038/s43247-021-00208-5`. URL: `https://www.nature.com/articles/s43247-021-00208-5`.

[27] C. Esposito et al. “Flow loss in deltaic distributaries: Impacts on channel geometry and backwater reach”. In: *Water Resources Research* 56.1 (2020), e2019WR026463. DOI: `10.1029/2019WR026463`.

[28] Graham Evans. “Deltas: the fertile dustbins of the continents”. In: *Proceedings of the Geologists’ Association* 123.3 (2012), pp. 397–418. DOI: `10.1016/j.pgeola.2011.11.001`.

[29] S.M. Gagliano and W.G. McIntire. *Reports on the Mekong River Delta*. Tech. rep. TR-57. Baton Rouge: Coastal Studies Institute, Louisiana State University, 1968. URL: `http://www.dtic.mil/docs/citations/AD0831165`.

[30] Google LLC. *Google Earth Pro*. `https://earth.google.com/`. Accessed: July 2025. 2025.

[31] C. R. Hackney et al. “Sand mining far outpaces natural supply in a large alluvial river”. In: *Earth Surface Dynamics* 9.6 (2021), pp. 1323–1334. DOI: `10.5194/esurf-9-1323-2021`. URL: `https://esurf.copernicus.org/articles/9/1323/2021/`.

[32] Christopher R. Hackney et al. “The influence of flow discharge variations on the morphodynamics of a diffluence–confluence unit on a large river”. In: *Earth Surface Processes and Landforms* 42.10 (2017), pp. 1522–1538. DOI: `10.1002/esp.4204`.

[33] A. J. F. Hoitink et al. “Tidal controls on river delta morphology”. In: *Nature Geoscience* 10.9 (2017), pp. 637–645. DOI: `10.1038/ngeo3000`. URL: `https://doi.org/10.1038/ngeo3000`.

[34] Institute of Coastal and Offshore Engineering (ICOE). *Relative Sea Level Rise and Sand Mining Data in the Vietnamese Mekong Delta (2000–2024)*. Institute of Coastal and Offshore Engineering, Vietnam. Unpublished data provided through research collaboration. 2023. URL: `http://www.icoe.org.vn/index.php?mod=list&action=view&gid=1006&id=1042`.

[35] A. P. Iwantoro, M. van der Vegt, and M. G. Kleinhans. "Stability and Asymmetry of Tide-Influenced River Bifurcations". In: *Journal of Geophysical Research: Earth Surface* 127.6 (2022). DOI: `10.1029/2021JF006282`. URL: `https://doi.org/10.1029/2021JF006282`.

[36] P. Ph. Jansen et al. *Principles of River Engineering: The Non-Tidal Alluvial River*. Delft Hydraulics Laboratory Publication. London: Pitman Publishing, 1979.

[37] C. Jordan et al. "Sand mining in the Mekong Delta revisited — current scales of local sediment deficits". In: *Scientific Reports* 9 (2019), p. 17823. DOI: `10.1038/s41598-019-53804-z`.

[38] David Knighton. *Fluvial Forms and Processes: A New Perspective*. 2nd. eBook published 2014. London: Routledge, 1998. DOI: `10.4324/9780203784662`. URL: `https://doi.org/10.4324/9780203784662`.

[39] G. Mathias Kondolf et al. "Changing sediment budget of the Mekong: Cumulative threats and management strategies for a large river basin". In: *Science of The Total Environment* 625 (2018), pp. 114–134. DOI: `10.1016/j.scitotenv.2017.11.361`. URL: `https://www.sciencedirect.com/science/article/pii/S0048969717334198`.

[40] M. G. Kondolf et al. "Changing sediment budget of the Mekong: Cumulative threats and management strategies for a large river basin". In: *Science of the Total Environment* 625 (2018), pp. 114–134. DOI: `10.1016/j.scitotenv.2017.12.207`. URL: `https://doi.org/10.1016/j.scitotenv.2017.12.207`.

[41] N. Leonardi, T. Sun, and S. Fagherazzi. "Interplay between river and tidal forcings in a delta distributary". In: *Advances in Water Resources* 80 (2015), pp. 69–78. DOI: `10.1016/j.advwatres.2015.03.005`.

[42] Steven Ly, Takahiro Sayama, and Sophal Try. "Integrated impact assessment of climate change and hydropower operation on streamflow and inundation in the lower Mekong Basin". In: *Progress in Earth and Planetary Science* 10.55 (2023). DOI: `10.1186/s40645-023-00586-8`. URL: `https://doi.org/10.1186/s40645-023-00586-8`.

[43] Mekong River Commission. *Hydropower*. Accessed 2023. Mekong River Commission. 2023. URL: `https://www.mrcmekong.org/our-work/topics/hydropower/`.

[44] Mekong River Commission. *State of the Basin Report*. Vientiane, Lao PDR: Mekong River Commission, 2010, p. 232.

[45] Ehab Meselhe, Kazi Sadid, and Ashok Khadka. "Sediment Distribution, Retention and Morphodynamic Analysis of a River-Dominated Deltaic System". In: *Water* 13.10 (2021), p. 1341. DOI: `10.3390/w13101341`.

[46] E. Meyer-Peter and R. Müller. "Formulas for Bed-Load Transport". In: *Proceedings of the 2nd Meeting of the International Association for Hydraulic Structures Research*. Stockholm, Sweden, 1948, pp. 39–64.

[47] J. D. Milliman and B. U. Haq. "River-sediment inputs to major deltas". In: *Sea-Level Rise and Coastal Subsidence: Causes, Consequences, and Strategies*. Ed. by B. U. Haq and J. D. Milliman. Dordrecht, Netherlands: Springer, 1996, pp. 63–85.

[48] John D. Milliman and Katherine L. Farnsworth. *River Discharge to the Coastal Ocean: A Global Synthesis*. Cambridge, UK: Cambridge University Press, 2011. ISBN: 9780521769053. DOI: `10.1017/CBO9780511781247`. URL: `https://doi.org/10.1017/CBO9780511781247`.

[49] P. S. J. Minderhoud et al. "Mekong delta much lower than previously assumed in sea-level rise impact assessments". In: *Nature Communications* 10.1 (2019), p. 3847. DOI: `10.1038/s41467-019-11602-1`.

[50] Daniel N. Moriasi et al. "Model evaluation guidelines for systematic quantification of accuracy in watershed simulations". In: *Transactions of the ASABE* 50.3 (2007), pp. 885–900. DOI: `10.13031/2013.23153`.

[51] Government of the Netherlands. *Mangrove Living Lab, the result of 'flourishing partnership' between Vietnam and the Netherlands*. `https://www.government.nl/latest/weblogs/the-work-of-the-ministry-of-foreign-affairs/2024/restore-mangrove-forests-vietnam-in-cooperation-with-the-netherlands`. Ministry of Foreign Affairs, accessed September 18, 2025. Mar. 2024.

[52] T. Ngoc, N. Hoang, and H. Thu. *Mekong Delta Erosion: Is Authorities' Lack of Determination to Blame?* Accessed: 2025-07-06. 2023. URL: `https://e.vnexpress.net/news/news/environment/mekong-delta-erosion-is-authorities-lack-of-determination-to-blame-4650396.html`.

[53] A.D. Nguyen et al. "Using salt intrusion measurements to determine the freshwater discharge distribution over the branches of a multi-channel estuary: the Mekong Delta case". In: *Estuarine, Coastal and Shelf Science* 77 (2008), pp. 433–445. DOI: `10.1016/j.ecss.2007.10.010`. URL: `http://dx.doi.org/10.1016/j.ecss.2007.10.010`.

[54] V. L. Nguyen, T. K. O. Ta, and M. Tateishi. "Late Holocene depositional environments and coastal evolution of the Mekong River Delta, southern Vietnam". In: *Journal of Asian Earth Sciences* 18 (2000), pp. 427–439. DOI: `10.1016/S1367-9120(99)00076-0`.

[55] V. L. Nguyen et al. "Bottom morphology in the Song Hau distributary channel, Mekong River". In: *Geo-Marine Letters* 42.2 (2022), pp. 133–149. DOI: `10.1007/s00367-021-00701-0`.

[56] Daniel J. Nowacki et al. "Sediment dynamics in the lower Mekong River: Transition from tidal river to estuary". In: *Journal of Geophysical Research: Oceans* 120.9 (2015), pp. 6363–6383. DOI: `10.1002/2015JC010754`. URL: `https://doi.org/10.1002/2015JC010754`.

[57] Joakim Öjendal. *Sharing the Good-Modes of Managing Water Resources in the Lower Mekong River Basin*. Accessed: 2025-06-23. 2000. URL: `https://gupea.ub.gu.se/handle/2077/15144`.

[58] M. van Ormondt, L. C. van Rijn, and D. J. R. Walstra. *Description of TRANSPOR2004 and Implementation in Delft3D-ONLINE*. Tech. rep. Z3748.10. Delft, The Netherlands: WL | Delft Hydraulics, Nov. 2004.

[59] Stuart Orr et al. "Dams on the Mekong River: Lost fish protein and the implications for land and water resources". In: *Global Environmental Change* 22.4 (2012), pp. 925–932. DOI: `10.1016/j.gloenvcha.2012.06.002`.

[60] Uttam Pawar et al. "Frequency and trend analyses of annual peak discharges in the Lower Mekong Basin". In: *Heliyon* 9.9 (2023). Accessed: 2025-06-23, e19690. DOI: `10.1016/j.heliyon.2023.e19690`. URL: `https://www.researchgate.net/publication/373559205_Frequency_and_trend_analyses_of_annual_peak_discharges_in_the_Lower_Mekong_Basin`.

[61] Vietnam-Netherlands Mekong Delta Masterplan project. *Mekong Delta Water Resources Assessment Studies*. Vietnam-Netherlands Mekong Delta Masterplan project. Report. 2011.

[62] Marco Redolfi, Guido Zolezzi, and Marco Tubino. "Free instability of channel bifurcations and morphodynamic influence". In: *Journal of Fluid Mechanics* 799 (2016), pp. 476–504. DOI: `10.1017/jfm.2016.389`.

[63] Gerard Salter, Vaughan R. Voller, and Chris Paola. "How does the downstream boundary affect avulsion dynamics in a laboratory bifurcation?" In: *Earth Surface Dynamics* 7.4 (2019), pp. 911–927. DOI: `10.5194/esurf-7-911-2019`.

[64] M. G. Sassi et al. "Sediment discharge division at two tidally influenced river bifurcations". In: *Water Resources Research* 49.4 (2013), pp. 2119–2134. DOI: `10.1002/wrcr.20216`.

[65] P. Schiappacasse, B. Müller, and L. T. Linh. "Towards responsible aggregate mining in Vietnam". In: *Resources* 8.3 (2019), p. 138. DOI: `10.3390/resources8030138`.

[66] Ministry of Science and Technology (MOST). *Research and propose solutions for Science and Technology to forecast and prevent coastal encroachment in Tra Vinh province and surrounding areas*. Tech. rep. Hanoi, Vietnam: MOST, 2013.

[67] Ministry of Science and Technology (MOST). *Research on adverse impacts of morphological changes and water level reduction of the Mekong River system, proposing mitigation solutions*. Tech. rep. Hanoi, Vietnam: MOST, 2020.

[68] Ministry of Science and Technology (MOST). *Research on appropriate solutions and technology to prevent erosion and stabilize the coastal strip and estuaries of the Mekong River, from Tien Giang to Soc Trang*. Tech. rep. Hanoi, Vietnam: MOST, 2020.

[69] Ministry of Science and Technology (MOST). *Research on scientific and technological solutions to adjust and stabilize river sections with islands experiencing major morphological changes on the Tien and Hau rivers*. Tech. rep. Hanoi, Vietnam: MOST, 2016.

[70] SGGP. *Supply for the Chau Doc – Can Tho – Soc Trang Expressway, Phase 1*. 2025. URL: `https://www.sggp.org.vn/soc-trang-them-mot-mo-cat-song-duoc-dua-vao-khai-thac-theo-co-che-dac-thu-post756105.html` (visited on 07/16/2025).

[71] Vietnam Department of Survey and Mapping. *Transformation Between VN-2000 and WGS-84 Vertical Datums*. Tech. rep. Accessed via internal document: vert_datum_VN2000_WGS84.pdf. Ministry of Natural Resources and Environment (MONRE), 2009.

[72] James P. M. Syvitski and Albert Kettner. “Sediment flux and the Anthropocene”. In: *Philosophical Transactions of the Royal Society A: Mathematical, Physical and Engineering Sciences* 369.1938 (2011), pp. 957–975. DOI: `10.1098/rsta.2010.0329`. URL: `https://royalsocietypublishing.org/doi/10.1098/rsta.2010.0329`.

[73] James P. M. Syvitski et al. “Sinking deltas due to human activities”. In: *Nature Geoscience* 2 (2009), pp. 681–686. DOI: `10.1038/ngeo629`.

[74] R. N. Szupiany et al. “Flow fields, bed shear stresses, and suspended bed sediment dynamics in bifurcations of a large river”. In: *Water Resources Research* 48.11 (2012), W11515. DOI: `10.1029/2011WR011677`.

[75] D. Thi Ha, S. Ouillon, and G. Van Vinh. “Water and Suspended Sediment Budgets in the Lower Mekong from High-Frequency Measurements (2009–2016)”. In: *Water* 10 (2018), p. 846. DOI: `10.3390/w10060846`. URL: `https://doi.org/10.3390/w10060846`.

[76] N.N. Thuy. *Hydrometeorology of Vietnam Sea Waters*. In Vietnamese. Hanoi: 1 Marine Hydrometeorological Center, Science & Technical Publishers, 1988.

[77] N.N. Thuy. *Tides in the Gulf of Thailand and in the coastal regions of the Mekong Delta*. Symposium, Can-Tho Institute. In Vietnamese. 1979.

[78] N.N. Thuy. *Tides in the Vietnam Estuaries*. In Vietnamese. Marine Hydrometeorological Center, 1988.

[79] UBND tỉnh Sóc Trăng. *For the construction of Subproject 4 of the Chau Doc – Can Tho – Soc Trang Expressway (East–West Expressway of the Mekong Delta)*. 2024. URL: `https://mytu.soctrang.gov.vn/SiteFolders/Root/5116/2024/BC%20danh%20gia%20tac%20dong%20moi%20truong/Thang%201/THAM%20VAN%20NOI%20DUNG%20DTM%20MS11%20CTY%20HAI%20DANG.pdf` (visited on 07/16/2025).

[80] UBND tỉnh Sóc Trăng. *For the investment and construction of the Chau Doc – Can Tho – Soc Trang Expressway Project, Phase 1*. 2024. URL: `https://www.soctrang.gov.vn/ubnd-stg/4/469/65921/396085/Cac-du-an-dau-tu-xay-dung-cong-trinh-trong-diem-tren-dia-ban-tinh-soc-trang/Khoi-cong-khai-thac-mo-cat-MS04-tren-song-Hau.aspx` (visited on 07/16/2025).

[81] Ủy ban Nhân dân tỉnh Trà Vinh. *Quyết định 2142/QĐ-UBND năm 2011 về quy hoạch sử dụng cát, sỏi xây dựng trên địa bàn tỉnh Trà Vinh đến năm 2015, định hướng đến năm 2020*. `https://thuviennhadat.vn/van-ban-phap-luat-viet-nam/quyet-dinh-2142-qd-ubnd-nam-2011-quy-hoach-su-dung-cat-soi-xay-dung-tra-vinh-196290.html`. Planning for the use of construction sand and gravel in Trà Vinh Province from 2010 to 2015, with an orientation toward 2020. Currently, the mines have ceased operation. 2011. (Visited on 07/16/2025).

[82] Ủy ban Nhân dân tỉnh Vĩnh Long. *Quyết định 10/2018/QĐ-UBND điều chỉnh quy hoạch khai thác và sử dụng cát lòng sông tỉnh Vĩnh Long đến năm 2020, tầm nhìn đến năm 2030*. `https://thuviennhadat.vn/van-ban-phap-luat-viet-nam/quyet-dinh-10-2018-qd-ubnd-dieu-chinh-quy-hoach-khai-thac-va-su-dung-cat-long-song-vinh-long-392367.html`. Part of exploration and sand exploitation plan in Vinh Long (2016–2020), vision to 2030. Includes inactive mines. 2018. (Visited on 07/16/2025).

[83] Pham Dinh Van, Shinjiro Kanae, and Dai Yamazaki. “A study of the climate change impacts on fluvial flood propagation in the Vietnamese Mekong Delta”. In: *Hydrology and Earth System Sciences* 16.12 (2012), pp. 4637–4649. DOI: `10.5194/hess-16-4637-2012`.

[84] Leo C. Van Rijn. “Unified View of Sediment Transport by Currents and Waves. I: Initiation of Motion, Bed Roughness, and Bed-Load Transport”. In: *Journal of Hydraulic Engineering* 133.6 (2007), pp. 649–667. DOI: `10.1061/(ASCE)0733-9429(2007)133:6(649)`.

[85] G. Vasilopoulos et al. “Establishing sustainable sediment budgets is critical for climate-resilient mega-deltas”. In: *Environmental Research Letters* 16.6 (2021), p. 064089. DOI: `10.1088/1748-9326/ac06fc`.

[86] Vietnam Ministry of Natural Resources and Environment. *QCVN 11:2008/BTNMT - National Technical Regulation on the Establishment of Elevation Control Network*. `https://example.com`. Accessed PDF titled: ”quy-chuan-qcvn-11-2008-btnmt-xay-dung-luoi-do-cao.pdf”. 2008.

[87] S.A. de Wit. “Master Thesis”. Contributor(s): Dirk S. van Maren (TU Delft - Environmental Fluid Mechanics), Z. B. Wang (TU Delft - Coastal Engineering). Master’s thesis. Delft, Netherlands: TU Delft - Civil Engineering & Geosciences, 2025. URL: `https://resolver.tudelft.nl/uuid:a776f4ac-d9e5-4e4d-b1a7-04544d3f5953`.

[88] Colin D. Woodroffe et al. “Landscape Variability and the Response of Asian Megadeltas to Environmental Change”. In: *Global Change and Integrated Coastal Management: The Asia-Pacific Region*. Ed. by Nick Harvey. Vol. 10. Coastal Systems and Continental Margins. Dordrecht: Springer, 2006, pp. 277–314. DOI: `10.1007/1-4020-3628-0_16`.

[89] F. Xing et al. “Analysis and numerical modeling of the flow and sand dynamics in the lower Song Hau channel, Mekong Delta”. In: *Continental Shelf Research* 147 (2017), pp. 62–77. DOI: `10.1016/j.csr.2017.08.003`. URL: `http://dx.doi.org/10.1016/j.csr.2017.08.003`.

[90] K. W. Yuen et al. “Extent of illegal sand mining in the Mekong Delta”. In: *Communications Earth & Environment* 5 (2024), p. 31. DOI: `10.1038/s43247-023-01161-1`.

[91] Claudia Zoccarato, Philip S. J. Minderhoud, and Pietro Teatini. “The role of sedimentation and natural compaction in a prograding delta: insights from the mega Mekong delta, Vietnam”. In: *Scientific Reports* 8 (2018), p. 11437. DOI: `10.1038/s41598-018-29734-7`. URL: `https://www.nature.com/articles/s41598-018-29734-7`.

[92] Guido Zolezzi, Walter Bertoldi, and Marco Tubino. “Morphological Analysis and Prediction of River Bifurcations”. In: *Braided Rivers: Process, Deposits, Ecology and Management*. Ed. by Gregory H. Sambrook Smith et al. Vol. 36. International Association of Sedimentologists Special Publications. Blackwell Publishing Ltd, 2006, pp. 297–312. DOI: `10.1002/9781444304374.ch11`.

A

Vertical datum conversion to VNES (VN-2000)

All steps for the vertical datum conversion are summed up below. In this Appendix the method is described step by step.

1. Conversion from Geodetic WGS84 to ECEF Coordinates
2. Helmert transformation (WGS84 to VN-2000, G1762, epoch 2005)
3. Convert ECEF VN-2000 to geodetic coordinates
4. Project to VN-2000 UTM Zone 48N

1. Conversion from Geodetic WGS84 to ECEF Coordinates
To convert from geodetic WGS84 coordinates (ϕ, λ, h), where ϕ is latitude, λ is longitude, and h is ellipsoidal height, to Earth-Centered Earth-Fixed (ECEF) Cartesian coordinates (X, Y, Z), the following equations were used:

$$\begin{aligned} a &= 6378137.0 \quad \text{(WGS84 semi-major axis)} \\ f &= \frac{1}{298.257223563} \quad \text{(WGS84 flattening)} \\ e^2 &= f \cdot (2 - f) \quad \text{(eccentricity squared)} \\ N &= \frac{a}{\sqrt{1 - e^2 \cdot \sin^2 \phi}} \end{aligned}$$

$$\begin{aligned} X &= (N + h) \cdot \cos \phi \cdot \cos \lambda \\ Y &= (N + h) \cdot \cos \phi \cdot \sin \lambda \\ Z &= (N \cdot (1 - e^2) + h) \cdot \sin \phi \end{aligned}$$

These formulas were implemented in Python to convert a dataset of latitude, longitude, and altitude values to ECEF coordinates.

2. Helmert transformation (WGS84 to VN-2000, G1762, epoch 2005)
The seven-parameter Helmert transformation was applied to convert ECEF coordinates from the WGS84 datum to the VN-2000 geodetic system (G1762, epoch 2005). The transformation formulas used are stated below.

$$
\begin{aligned}
X_2 &= T_x + (1 + D) \cdot X - R_z \cdot Y + R_y \cdot Z \\
Y_2 &= T_y + R_z \cdot X + (1 + D) \cdot Y - R_x \cdot Z \\
Z_2 &= T_z - R_y \cdot X + R_x \cdot Y + (1 + D) \cdot Z
\end{aligned}
$$

Where:

- $T_x = 0.1947154$ m, $T_y = 0.0378661$ m, $T_z = 0.1104386$ m, the translation parameters
- $D = -2.217 \times 10^{-9}$, the scale factor
- $R_x = 1.0920 \times \frac{\pi}{180 \cdot 3600 \cdot 1000}$, $R_y = 7.0395 \times \frac{\pi}{180 \cdot 3600 \cdot 1000}$, $R_z = 72.1838 \times \frac{\pi}{180 \cdot 3600 \cdot 1000}$, the rotations (converted from milliarcseconds to radians)

The transformation was applied programmatically in Python over the ECEF coordinates obtained from the original WGS84 geodetic positions.

3. Convert ECEF VN-2000 to geodetic coordinates

The Earth-Centered Earth-Fixed (ECEF) coordinates previously transformed into the VN-2000 datum were converted to geodetic coordinates (ϕ, λ, h) (latitude, longitude, ellipsoidal height). This was done using the `Transformer` class from the `pyproj` library, which defines CRS transformations based on PROJ strings:

- Source CRS: `+proj=geocent +datum=WGS84 +units=m`
- Target CRS: `+proj=latlong +datum=WGS84`

This transformation results in longitude, latitude, and altitude values in the VN-2000 geodetic frame.

4. Project to VN-2000 UTM Zone 48N

The geodetic coordinates were then projected onto the Universal Transverse Mercator (UTM) coordinate system, specifically VN-2000 UTM Zone 48N. The projection used a central meridian of $105°45'$ E (i.e., `+lon_0=105.75`) to match the Vietnamese standard:

- Projection string: `+proj=utm +zone=48 +datum=WGS84 +units=m +lon_0=105.75`

This results in the final projected planar coordinates (X, Y) in meters, consistent with local VN-2000 bathymetry dataset. Altitude Z remained unchanged and was retained from the geodetic transformation.

B

SSC rating curves

To estimate the suspended sediment concentration (SSC) from discharge data, rating curves were established separately for flood and ebb conditions using a power-law relationship:

$$\text{SSC} = a \cdot Q^b \tag{B.1}$$

where: SSC is the suspended sediment concentration $[\mathrm{kg/m^3}]$, Q is the river discharge $[\mathrm{m^3/s}]$, a and b are empirical coefficients obtained via log-log linear regression.

Separate rating curves were fitted for each grain size class and flow direction using observed SSC and discharge data from 2016–2019. Parameters a and b were obtained through least-squares fitting in log-log space. In Figure B.1 the fitted coefficients are stated.

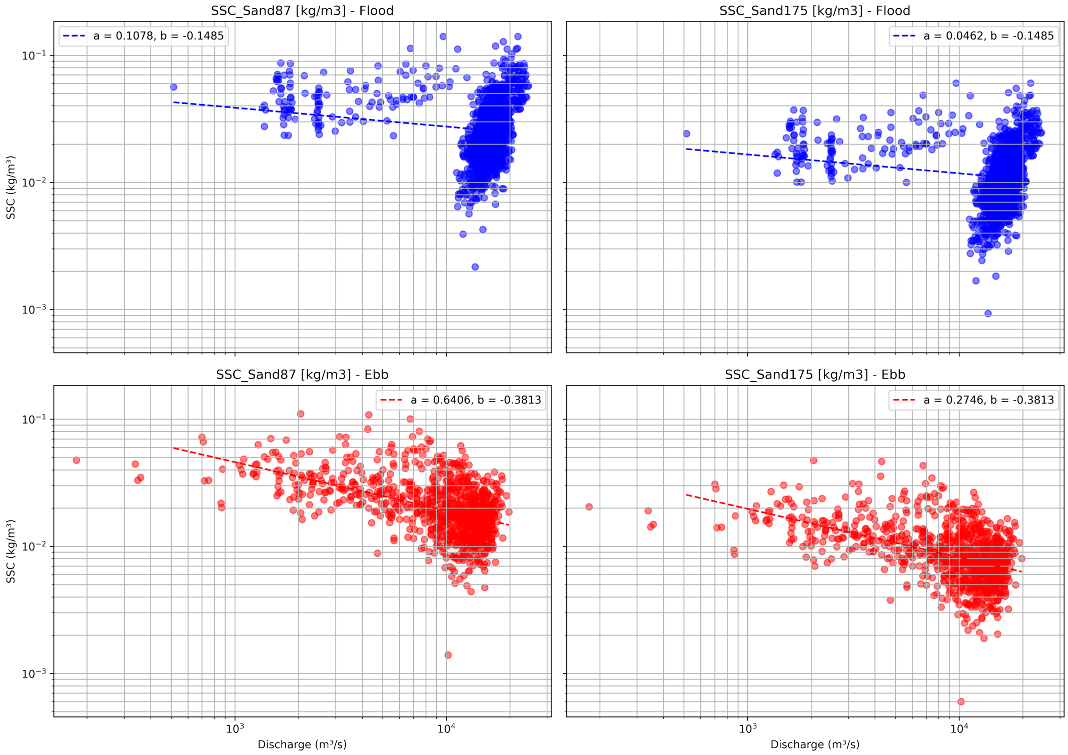

Figure B.1: SSC rating curves per sediment class per tide-phase

C

Sediment Transport Formulation - Van Rijn (2004)

The transport formulation of Van Rijn (2004) [58] is widely applied in Delft3D for non-cohesive sediment. It distinguishes between bedload and suspended load, which together form the total transport capacity. This is a capacity-based formulation, meaning that transport is primarily governed by the hydraulic conditions rather than by prescribed sediment concentrations at the model boundaries.

The bedload transport per unit width q_b is given by:

$$q_b = 0.005\,\frac{D_*^{0.3}}{D_{50}}\,T^{2.4}\,\sqrt{(s-1)gD_{50}^3} \tag{C.1}$$

The bedload transport depends strongly on the transport stage parameter T, which expresses the ratio between the actual bed shear stress and the critical shear stress.

The suspended load transport q_s is defined as:

$$q_s = 0.012\,\frac{D_*^{0.3}}{D_{50}}\,T^{1.5}\,U\,h \tag{C.2}$$

This equation provides the equilibrium suspended sediment transport, where U is the depth-averaged flow velocity and h the water depth.

The total transport is simply the sum of bedload and suspended load:

$$q_{tot} = q_b + q_s \tag{C.3}$$

The dimensionless particle diameter D_* is given by:

$$D_* = D_{50}\left(\frac{(s-1)g}{\nu^2}\right)^{1/3} \tag{C.4}$$

The transport stage parameter T is defined as:

$$T = \frac{\tau_b - \tau_{cr}}{\tau_{cr}} \tag{C.5}$$

This parameter indicates how much the bed shear stress exceeds the critical shear stress for motion. Sediment motion only occurs when $T > 0$.

Parameter definitions of all formulas are summed up below.

- q_b : bedload transport per unit width [m^2/s]
- q_s : suspended load transport per unit width [m^2/s]
- q_{tot} : total sediment transport per unit width [m^2/s]
- D_{50} : median grain size [m]
- D_* : dimensionless particle diameter $(-)$
- $s = \rho_s/\rho$: relative density (typically 2.65 for quartz)
- g : gravitational acceleration [m/s^2]
- ν : kinematic viscosity of water [m^2/s]
- τ_b : bed shear stress [N/m^2]
- τ_{cr} : critical shear stress for entrainment [N/m^2]
- T : transport stage parameter $(-)$
- U : depth-averaged flow velocity [m/s]
- h : water depth [m]

D

Scenario Design

D.1. Overview scenarios

Table D.1: Scenario codes and descriptions

Scenario Code	Description
Base	No modifications
AP-1	SSP2–4.5 Near Future
AP-2	SSP5–8.5 Near Future
AP-3	SSP5–8.5 Mid Future
AP-4	SSP5–8.5 Far Future
SM-1	Sand Mining extraction rate: 1 Mt/yr
SM-2	Sand Mining extraction rate: 2 Mt/yr
SM-3	Sand Mining extraction rate: 4 Mt/yr
SLR-1	Sea Level Rise (SLR)
SLR-2	Relative Sea Level Rise (RSLR)
HD-1	Upstream input sediment reduction 80%
HD-2	Discharge Q flattening
HD-3	Sediment reduction + Q flattening

D.2. Sand mining scenario design

Table D.2: Overview of sand mining activity locations, operation periods and extraction characteristics

DAD area number	GPS (DMS)	Start (date)	Stop (date)	Duration (months)	Status	Mining Area (m^2)	Extraction rate (m^3/month)	Extraction rate (m^3/ha/month)
1	10°03’00”N 105°48’14”E	2014	2020	72	past	580200	8333.33	143.63
2	10°00’33”N 105°49’38”E	2016	2020	48	past	355200	12500.00	351.91
3	9°58’48”N 105°51’07”E	2017	2020	36	past	91700	16666.67	1817.52
4	9°57’55”N 105°52’01”E	2014	2020	72	past	759500	41712.22	549.21
5	9°56’12”N 105°54’12”E	2014	2020	72	past	589000	10585.63	179.72
6	9°50’58”N 105°58’53”E	2024	2028	48	present	340000	24583.33	723.04
7	9°50’21”N 105°59’34”E	1-10-2024	1-12-2025	14	present	602000	46071.43	765.31
8	9°52’02”N 106°00’24”E	2006	2015	108	past	401300	24567.92	612.21
9	9°50’42”N 106°01’27”E	2018	2021	36	past	400000	–	–
10	9°49’52”N 106°02’04”E	2009	2015	72	past	282900	8683.46	306.94
11	9°47’55”N 106°01’45”E	15-8-2024	15-3-2025	7	present	600000	66609.71	1110.16
12	9°48’26”N 106°03’15”E	2006	2015	108	past	846200	26248.75	310.20
13	9°47’24”N 106°04’03”E	2009	2015	72	past	300000	20958.33	698.61
14	9°46’32”N 106°04’55”E	2009	2015	72	past	750000	13215.86	176.21
15	9°45’54”N 106°06’00”E	2009	2015	72	past	221830	4277.78	192.84
16	9°45’31”N 106°06’39”E	2009	2015	72	past	498000	8369.83	168.07
17	9°43’09”N 106°05’44”E	27-10-2024	10-1-2033	98	present	1000000	43516.51	435.17
18	9°42’01”N 106°06’07”E	2024	current	12	present	573000	23363.83	407.75
19	9°43’26”N 106°08’39”E	2010	2015	–	past	800000	–	–
20	9°40’21”N 106°10’39”E	1-7-2024	1-5-2024	22	past	1000000	500000.00	5000.00
21	9°38’46”N 106°12’21”E	2023	current	–	present	1679300	–	–
22	9°38’21”N 106°14’12”E	2010	2015	60	past	724000	28477.33	393.33
23	9°36’37”N 106°16’37”E	2024	current	–	present	616000	–	–
24	9°32’47”N 106°12’30”E	2024	current	12	present	736200	80000.00	1086.66

Table D.3: Information for DAD generation file Delft3D input

DAD area	X	Y	i	j	dx (m)	dy (m)	Area grid cell (m^2)	Mining area (m^2)	Grid cells
1	588091.8	1111049	51	18	30.55	147.21	4497.69	580200	128.9996
2	590660.3	1106540	39	55	27.40	140.00	3835.69	355200	92.6039
3	593378.2	1103322	18	83	55.92	138.92	7768.54	91700	11.8040
4	595026.7	1101698	14	99	66.88	141.92	9491.17	759500	80.0217
5	599024.3	1098545	12	135	72.74	148.45	10798.19	589000	54.5462
6	607609.9	1088924	1	227	75.32	148.10	11155.51	340000	30.4782
7	608862.2	1087791	1	238	61.80	148.88	9200.98	602000	65.4278
8	610376.0	1090898	53	230	56.24	148.20	8334.08	401300	48.1517
9	612302.5	1088447	53	251	60.73	146.41	8891.07	400000	44.9890
10	613434.4	1086914	52	264	55.72	150.83	8403.73	282900	33.6636
11	612866.6	1083319	6	280	57.66	129.12	7444.44	600000	80.5971
12	615605.6	1084280	52	288	57.26	152.34	8722.48	846200	97.0137
13	617074.0	1082380	54	304	51.53	140.10	7218.70	300000	41.5587
14	618663.4	1080788	53	320	61.92	152.45	9439.25	750000	79.4555
15	620647.7	1079627	55	335	88.15	141.65	12486.89	221830	17.7650
16	621838.4	1078924	56	345	108.36	155.05	16800.67	498000	29.6417
17	620176.6	1074557	14	359	91.61	149.16	13665.25	1000000	73.1783
18	620884.3	1072470	9	374	103.90	137.25	14260.66	573000	40.1805
19	625507.9	1075097	57	380	117.88	154.92	18262.19	800000	43.8064
20	629184.5	1069426	47	427	133.53	155.61	20777.82	1000000	48.1282
21	632303.7	1066519	48	456	152.25	141.20	21496.41	1679300	78.1200
22	635690.0	1065763	59	477	131.36	145.81	19154.45	724000	37.7980
23	640121.9	1062585	59	514	192.53	150.08	28894.54	616000	21.3189
24	632616.8	1055492	9	515	205.00	146.25	29980.23	736200	24.5562

E

Model verification

E.1. Hydrodynamic Calibration and Validation

Season	NSE (raw)	RMSE (raw) [m]	NSE (bias-corr.)	RMSE (bias-corr.) [m]
Overall	0.895	0.282	0.943	0.208
Wet season	0.890	0.291	0.934	0.225
Dry season	0.899	0.273	0.951	0.190

Table E.1: Calibration metrics for water level at Dai Ngai (2016–2019). Bias applied in corrected metrics: 0.1908 m.

Season	NSE (raw)	RMSE (raw) [m]	NSE (bias-corr.)	RMSE (bias-corr.) [m]
Overall	0.246	0.205	0.901	0.074
Wet season	0.274	0.197	0.914	0.068
Dry season	-0.132	0.213	0.838	0.081

Table E.2: Validation metrics for water level at Dai Ngai (2020–2022). Bias from calibration applied in corrected metrics: 0.1908 m.

E.2. Sediment Transport Calibration and Validation

To quantify model vs input consistency, the inflow and corresponding sediment fluxes are evaluated through discharge and SSC comparisons. The monthly discharge ratio (R_Q) is computed as:

$$R_Q = \frac{\sum_t Q_{\text{US}}(t)}{\sum_t Q_{\text{in}}(t)}, \tag{E.1}$$

where Q_{US} and Q_{in} represent the upstream and boundary discharges (m^3/s), respectively. Monthly medians of R_Q are used to assess seasonal variations in the inflow.

The cumulative inbound sediment volume (V_{in}) at each cross-section is obtained by integrating positive (inflow-only) sediment fluxes from the model output:

$$V_{\text{mod}}(t) = \int_0^t Q^+_{s,\text{sec}}(\tau)\,\mathrm{d}\tau$$

and compared to the expected inbound volume derived from boundary input SSC and inflow discharge:

$$V_{\text{exp}}(t) = \int_0^t \mathrm{SSC}_{\text{in}}(\tau)\,Q^+_{\text{in}}(\tau)\,\mathrm{d}\tau.$$

Class-wise concentrations are converted to volumetric fractions using $\rho_s = 2650\,\mathrm{kg/m^3}$ before temporal integration.

Figures E.1 (a) and (b) show the cumulative inbound sediment and discharge comparisons. Associated performance metrics (bias, ratio, RMSE) for both cumulative sediment and SSC time series are summarised in Tables E.3 and E.4.

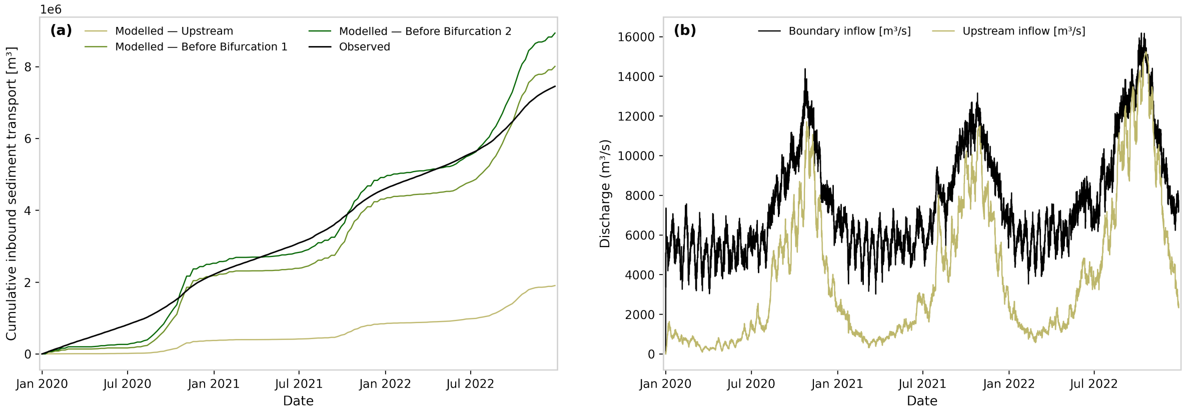

Figure E.1: Comparison input vs modelled: (a) Input SSC vs monitored at several cross-sections. (b) Input discharge vs upstream monitored discharge

Table E.3: Summary of model performance for cumulative inbound sediment (bias, ratio, RMSE).

Section	**Bias (kg/m^3)**	**Ratio model/input**	**RMSE (kg/m^3)**
Before bifurcation 1	0.03	1.07	0.03
Before bifurcation 2	0.05	1.20	0.04
Upstream	-0.12	0.25	0.04

Table E.4: Summary of model performance for SSC (inflow hours) — bias, ratio, and RMSE.

Section	**Bias (kg/m^3)**	**Ratio model/input**	**RMSE (kg/m^3)**
Before bifurcation 1	0.015	1.56	0.031
Before bifurcation 2	0.023	1.84	0.036
Upstream	-0.018	0.34	0.019

E.3. Sediment Balances per scenario

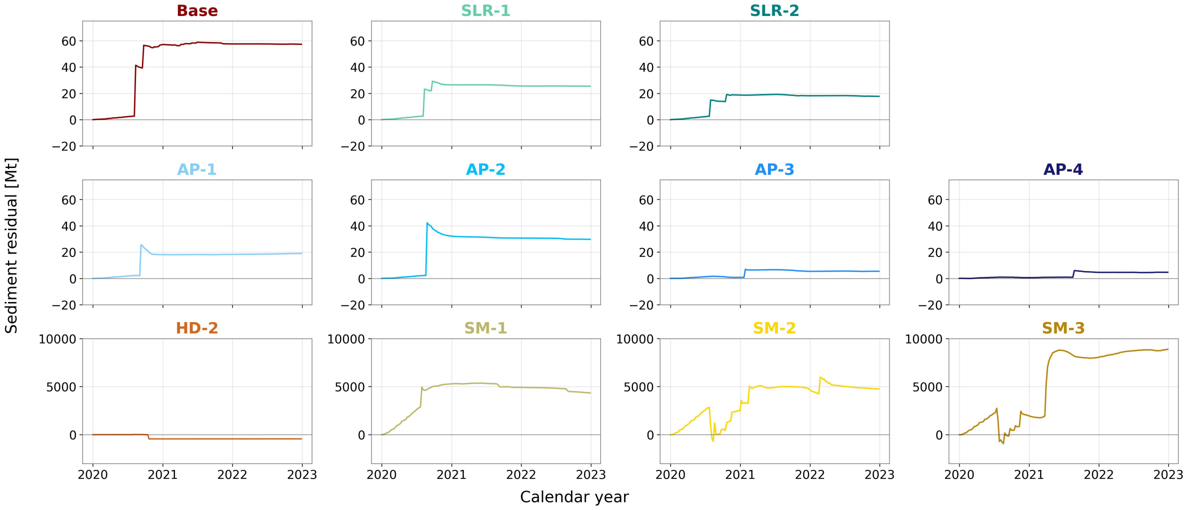

Figure E.2: Sediment balance for each scenario. It should ben noted that the range for the HD-2 and SM-1 to SM-3 have different y-range.

F

Sediment transport

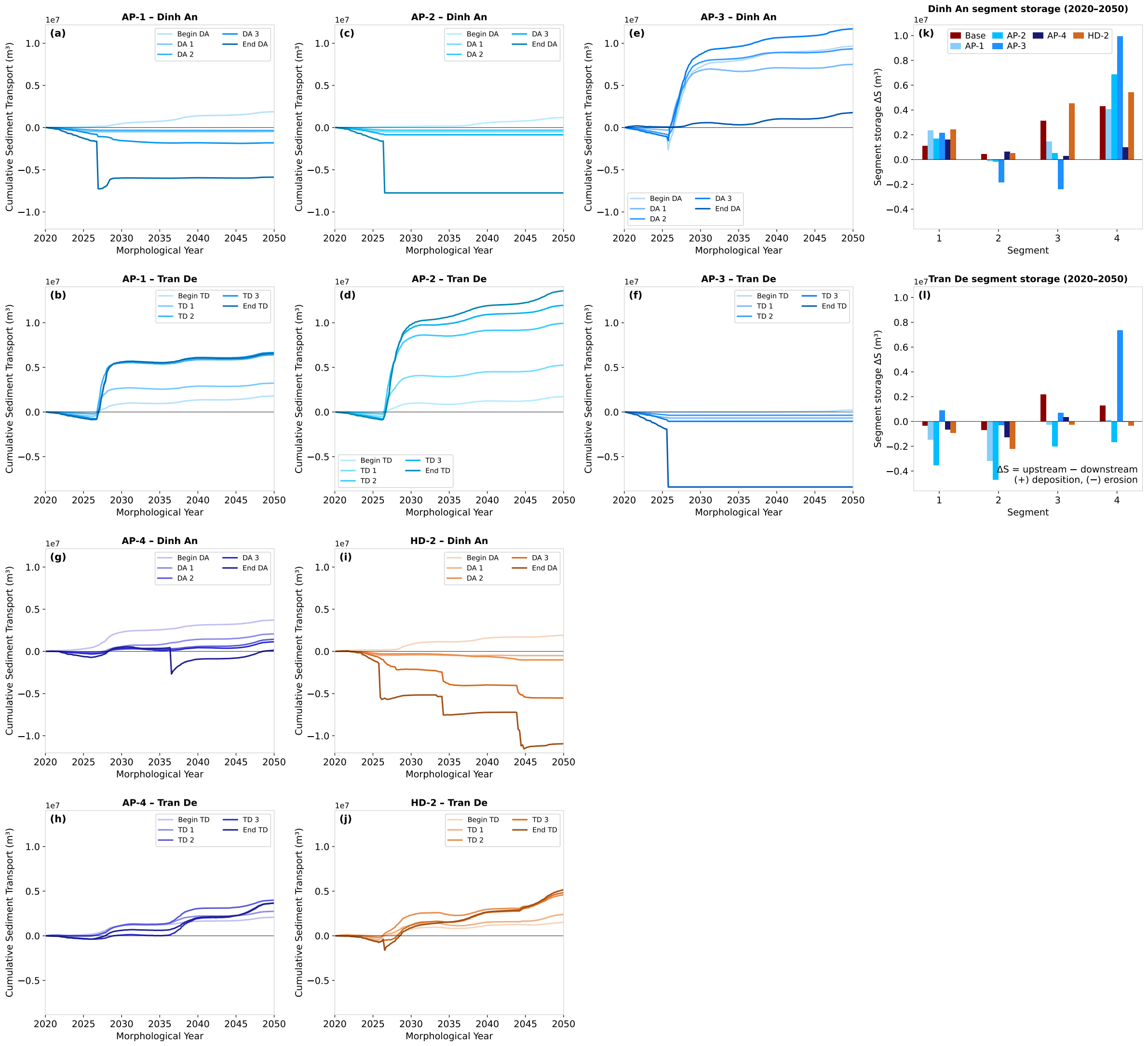

Figure F.1: Cumulative Sediment transport over time and SED budget (2020-2050) for discharge-modification scenarios

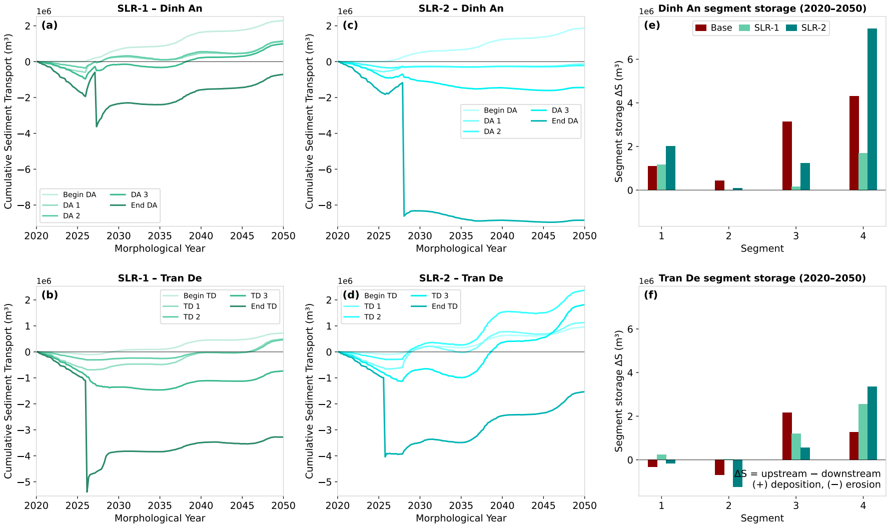

Figure F.2: Cumulative Sediment transport over time and SED budget (2020-2050) for Water Level increase scenarios

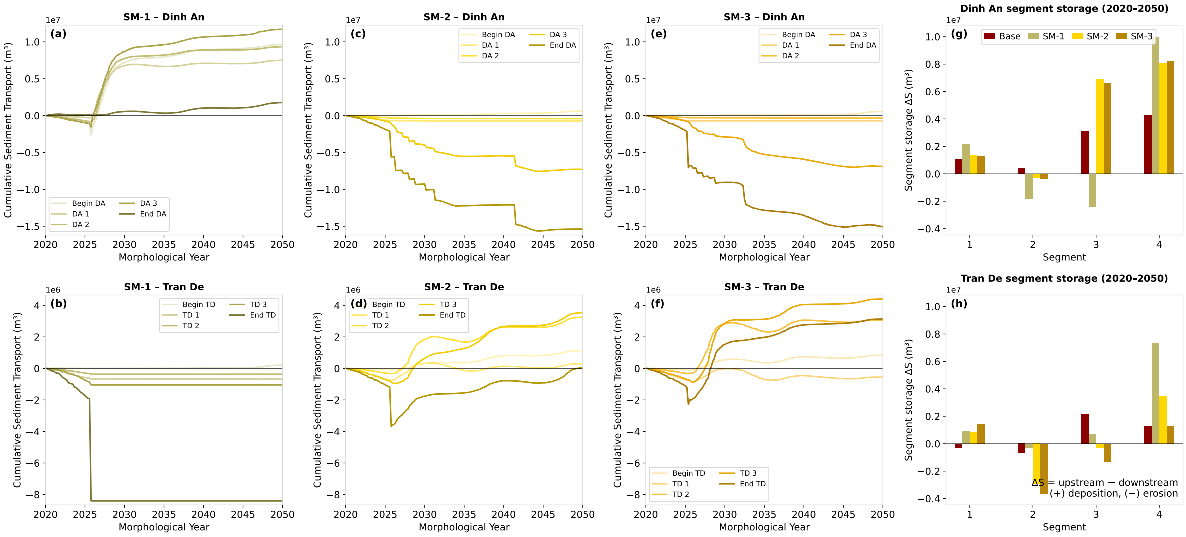

Figure F.3: Cumulative Sediment transport over time and SED budget (2020-2050) for Bed Level lowering scenarios

G

Bed level change over time

Bed level change over time for Altered Precipitation scenarios

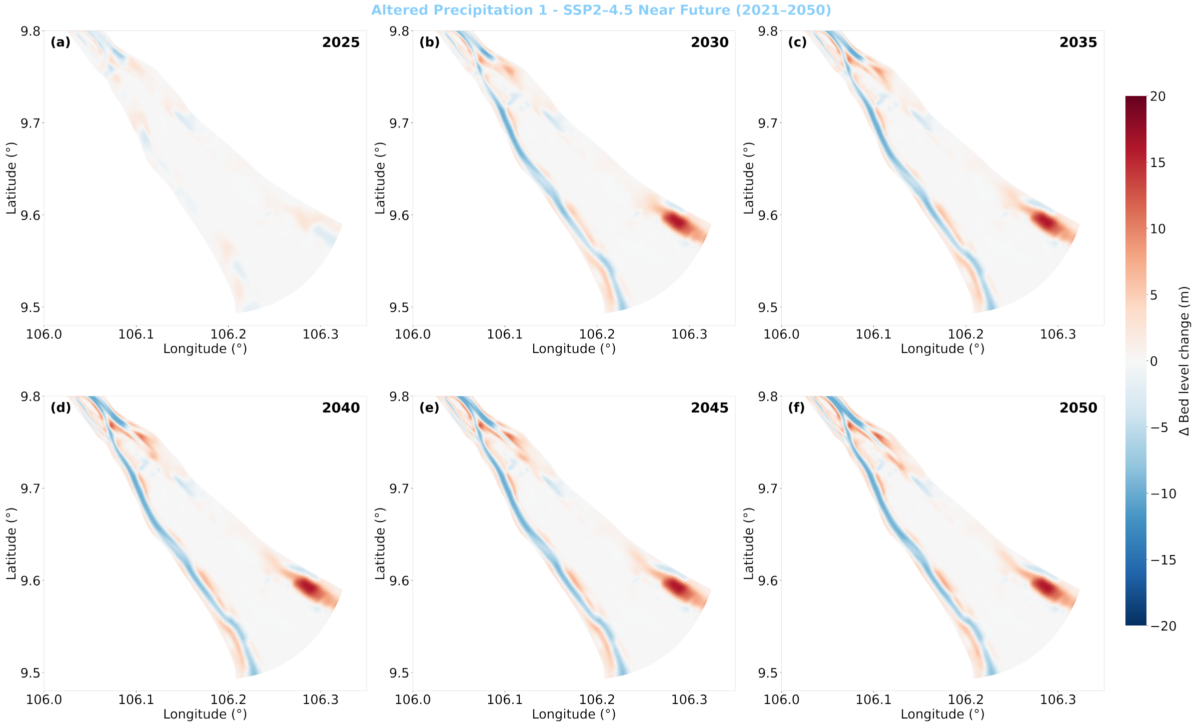

Figure G.1: Altered precipitation 1 (AP-1) - Bed level change over time

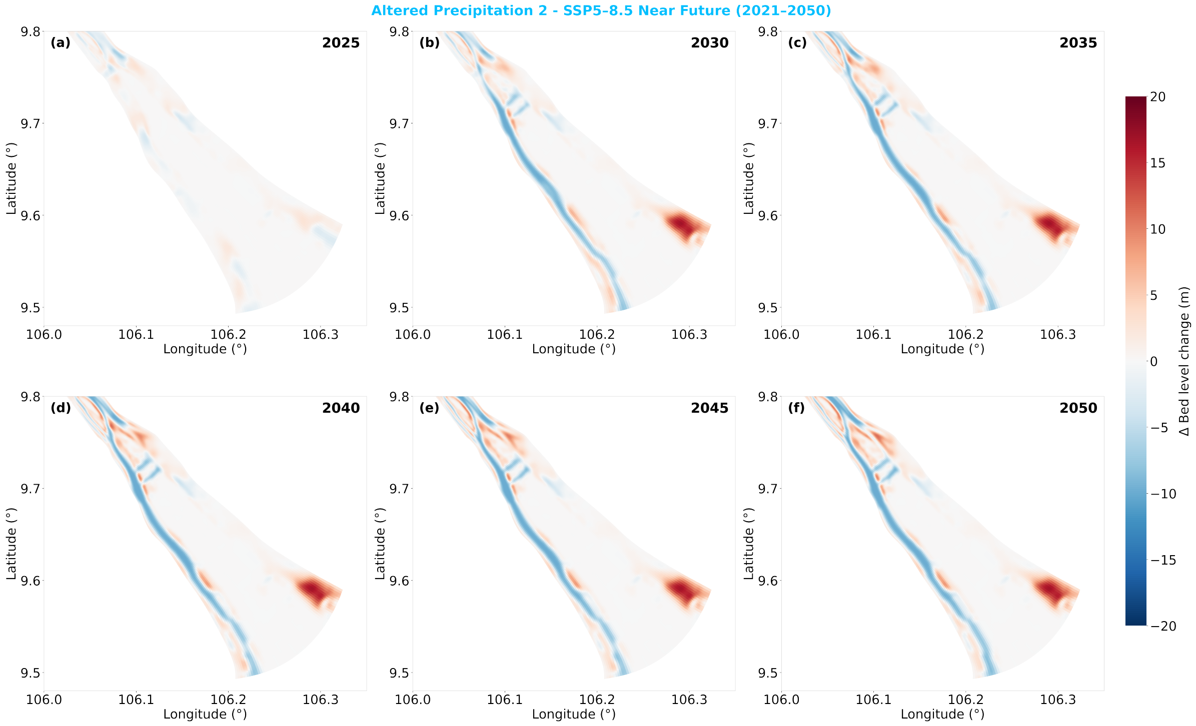

Figure G.2: Altered precipitation 2 (AP-2) - Bed level change over time

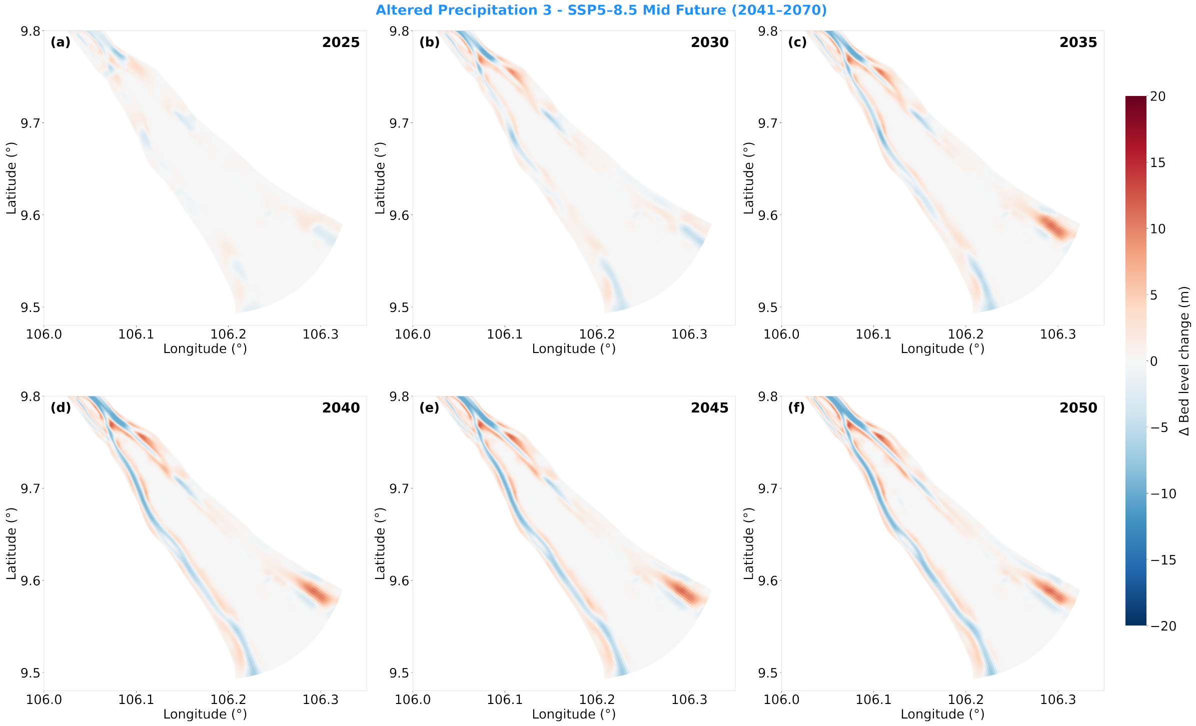

Figure G.3: Altered precipitation 3 (AP-3) - Bed level change over time

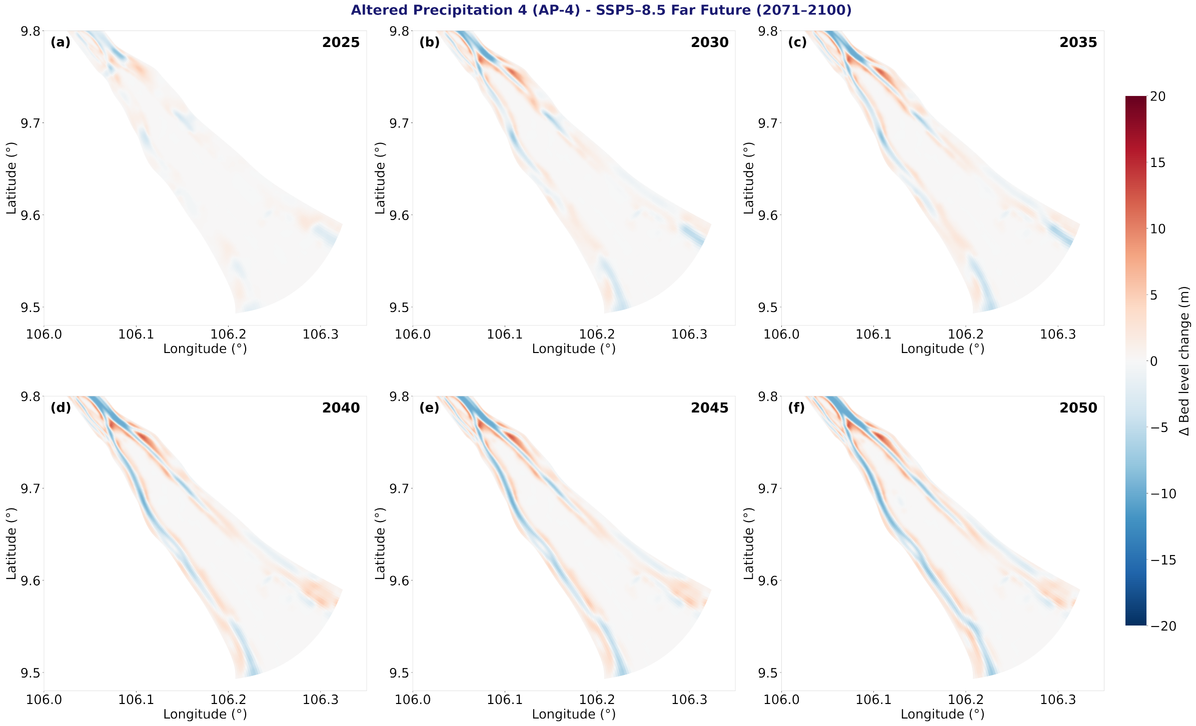

Figure G.4: Altered precipitation 4 (AP-4) - Bed level change over time

Bed level change over time for Hydropower dams scenario

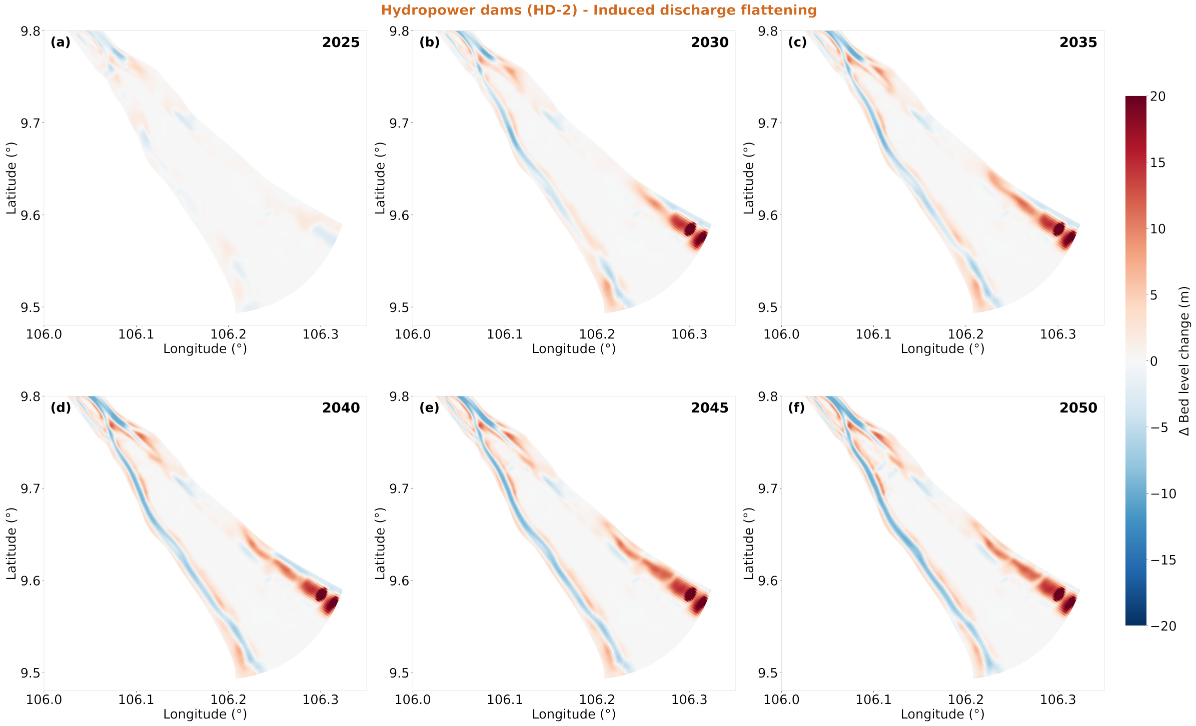

Figure G.5: Hydropower dams 2 (HD-2) - Bed level change over time

Bed level change over time for Sand Mining scenarios

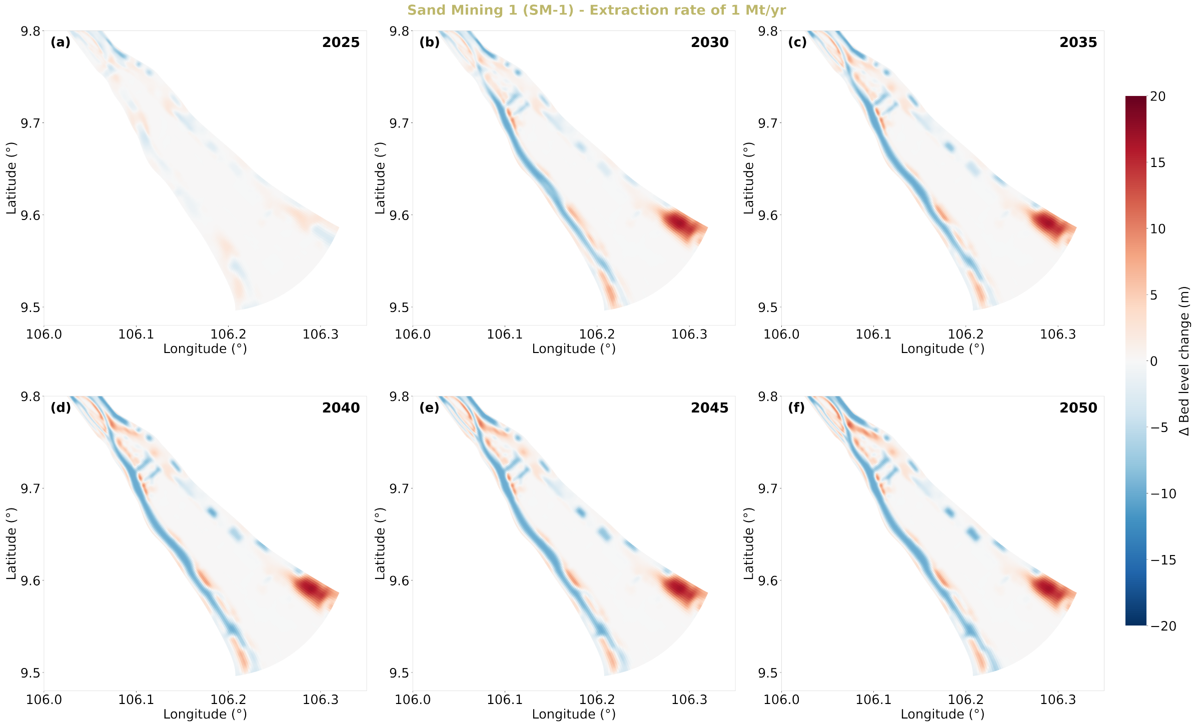

Figure G.6: Sand Mining 1 (SM-1) - Bed level change over time

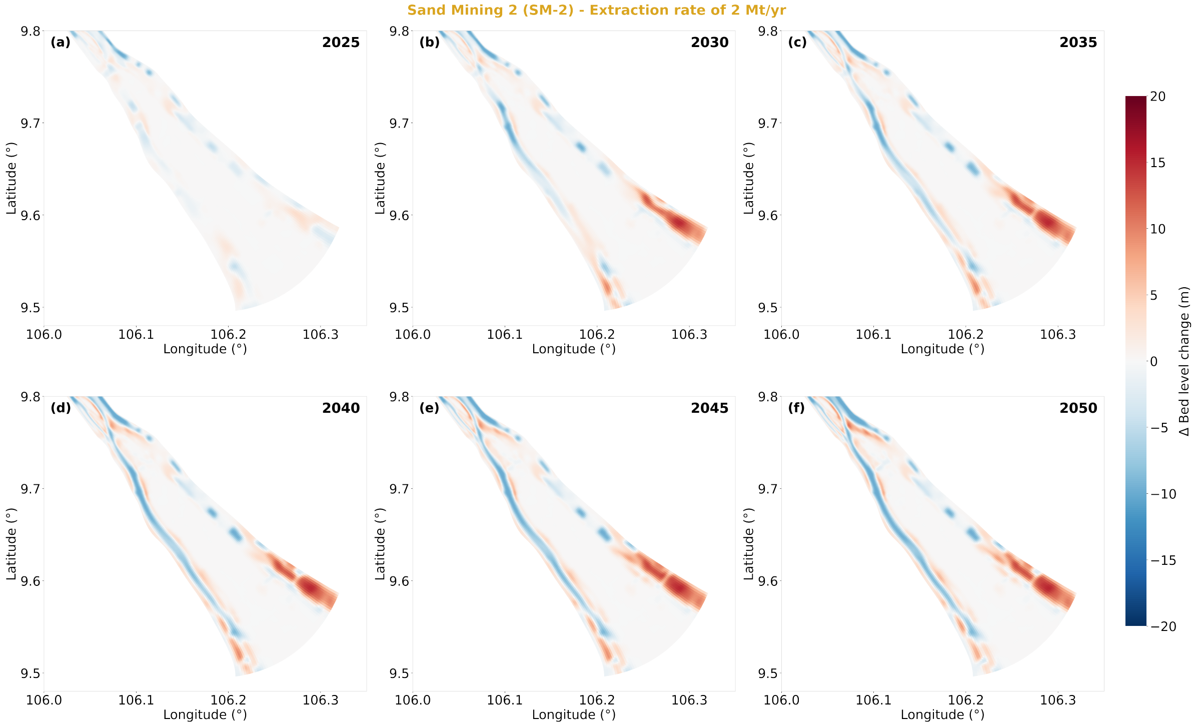

Figure G.7: Sand Mining 2 (SM-2) - Bed level change over time

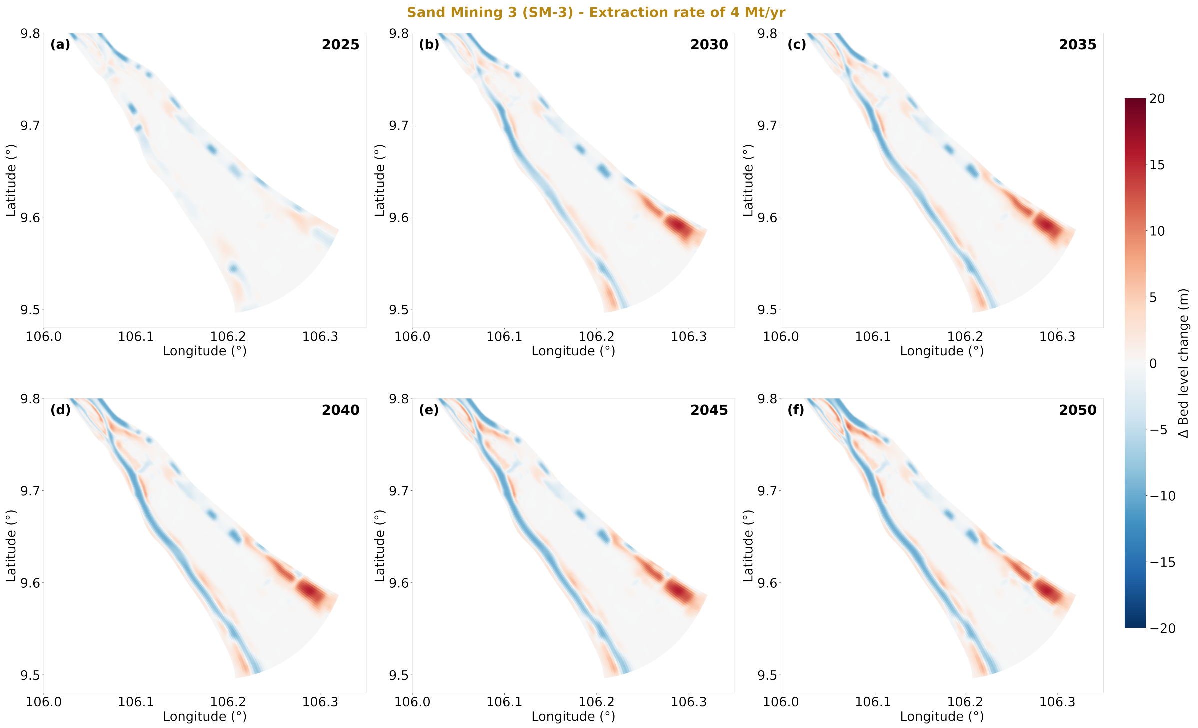

Figure G.8: Sand Mining 3 (SM-3) - Bed level change over time

Bed level change over time for Sea Level Rise scenarios

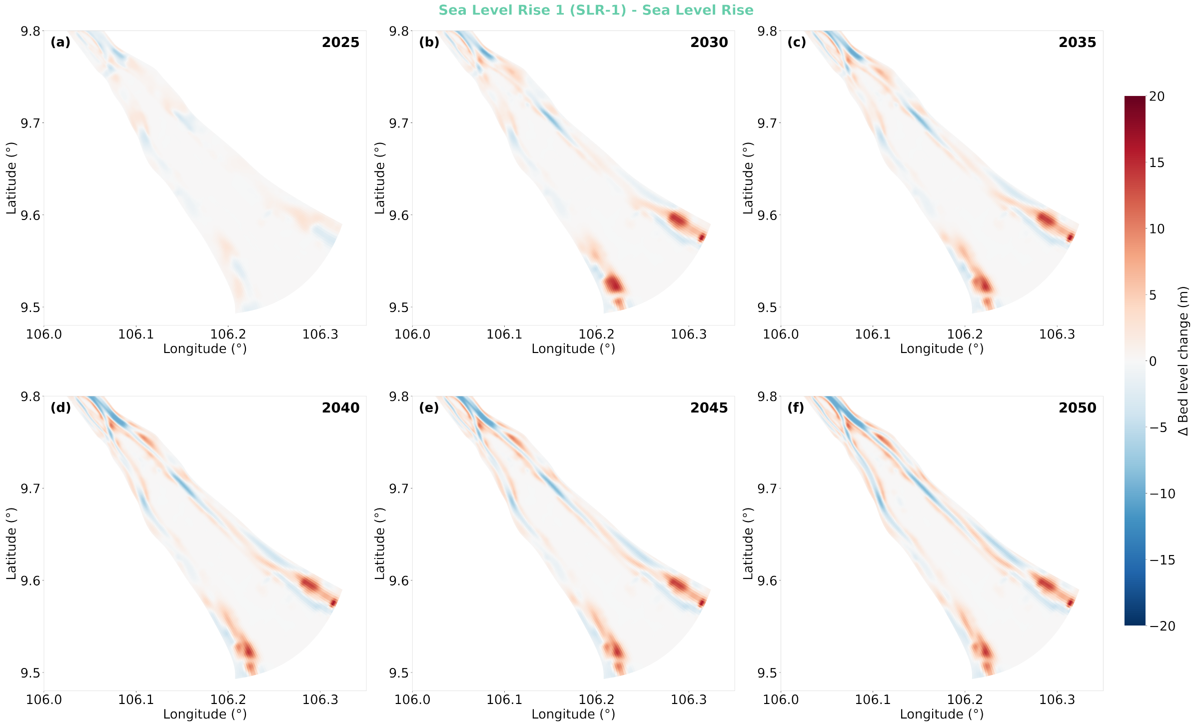

Figure G.9: Sea Level Rise 1 (SLR-1) - Bed level change over time

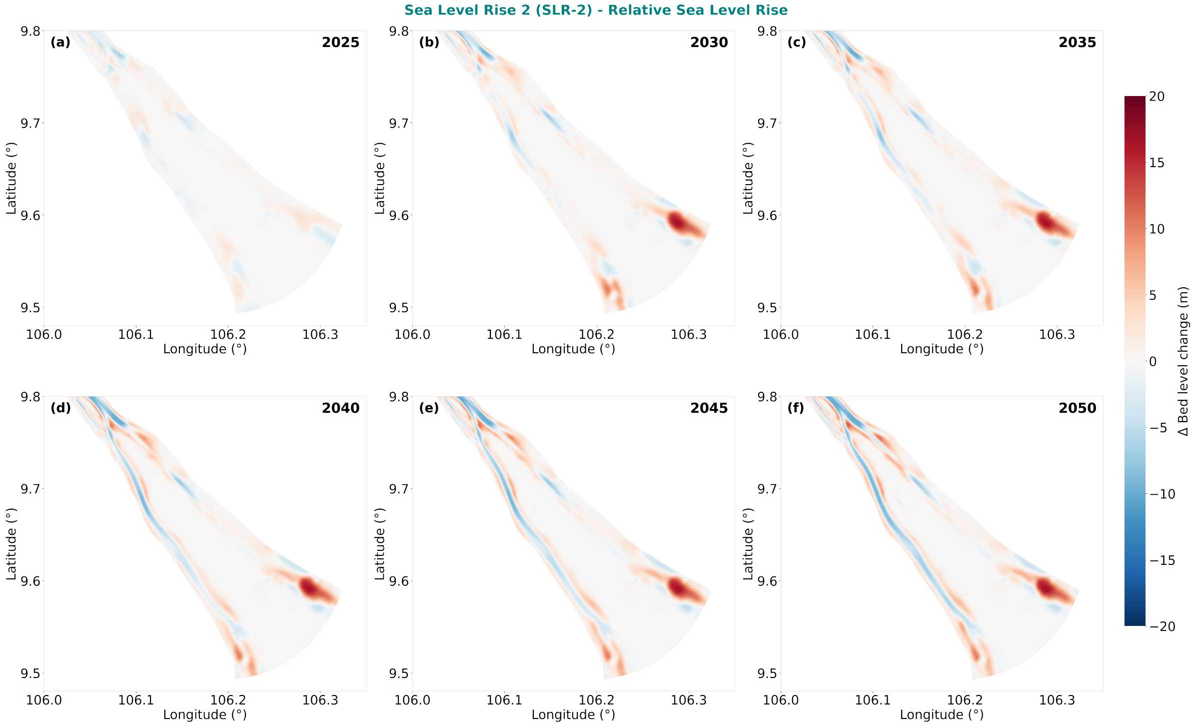

Figure G.10: Sea Level Rise 2 (SLR-2) - Bed level change over time

H

Bifurcation dynamics

H.1. Symmetry bifurcation

H.1.1. Symmetry index after bifurcation

To determine the symmetry index per season, the whole period is divided, $P \in \{\text{TOT}, \text{LOW}, \text{HIGH}\}$ with week set W_P according to the following formula:

$$\overline{\mathrm{SI}_X}^{P} = \frac{1}{|W_P|} \sum_{w \in W_P} \mathrm{SI}_X(w), \tag{H.1}$$

with low-flow season over Jan–May and high-flow season over Jun-Dec.

Time-series of symmetry indices

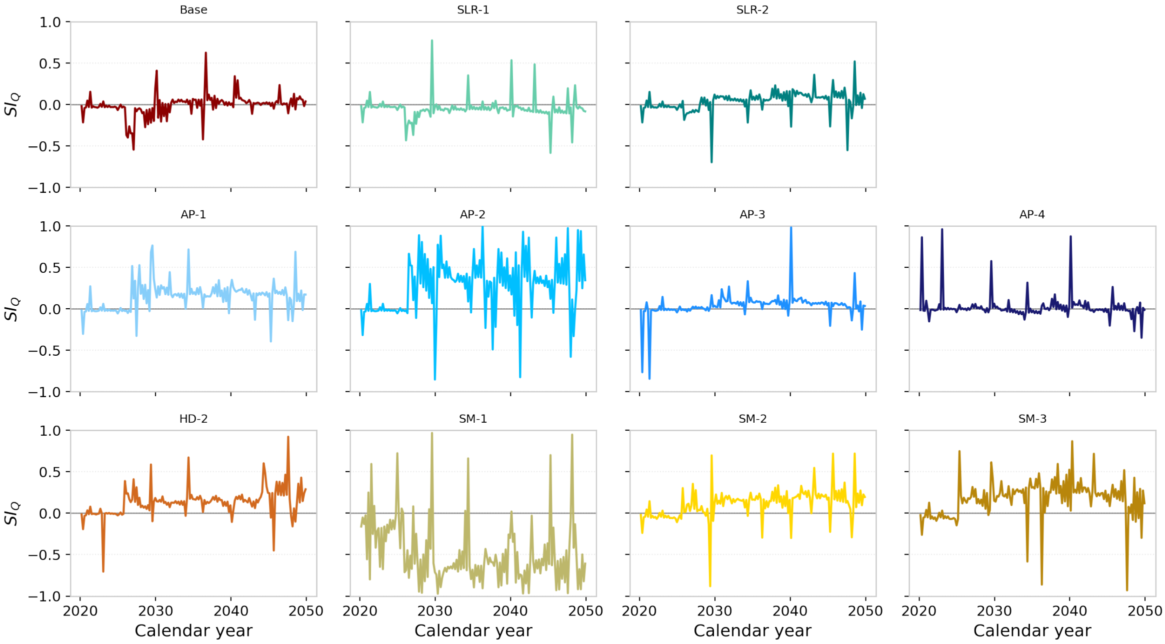

Figure H.1: Symmetry Index for discharge partitioning over bifurcation

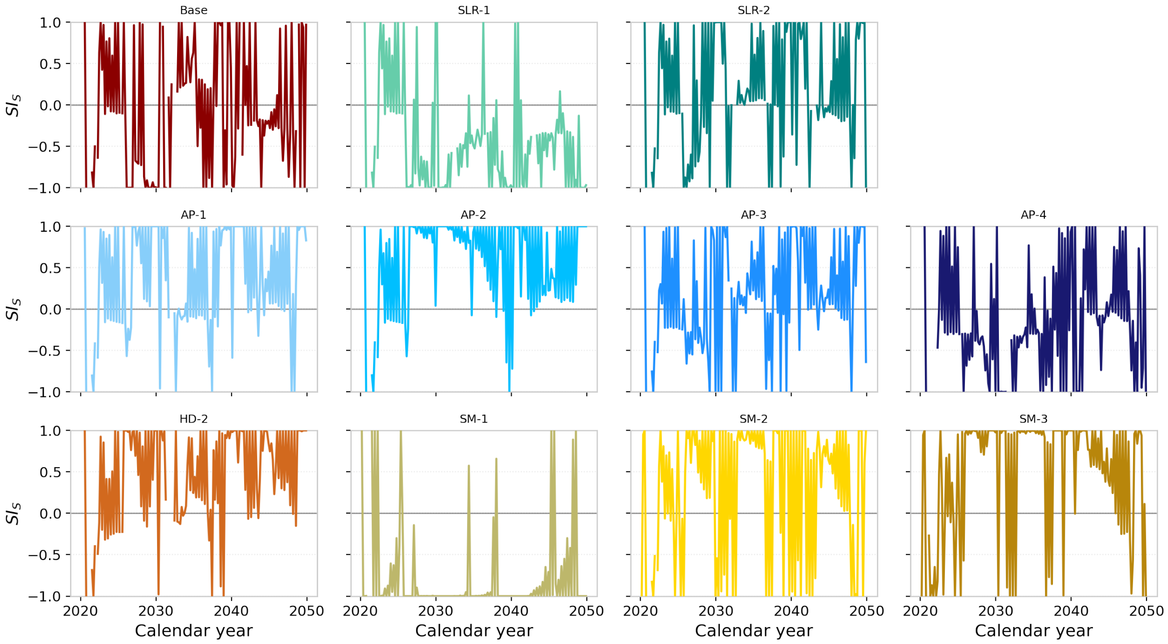

Figure H.2: Symmetry Index for sediment partitioning over bifurcation

H.1.2. Fractions of discharge after bifurcation

Discharge and sediment partitioning at the bifurcation can be expressed as fractions according to Equation H.2.

For each time step t, the fractions to the Tran De branch are defined as:

$$f_Q(t) = \frac{|Q_{TD}(t)|}{|Q_{TD}(t)| + |Q_{DA}(t)|}, \qquad f_S(t) = \frac{|S_{TD}(t)|}{|S_{TD}(t)| + |S_{DA}(t)|}, \tag{H.2}$$

where Q_{TD}, Q_{DA} denote discharges and S_{TD}, S_{DA} sediment fluxes to the Tran De and Dinh An branches, respectively.

- If the value is close to $1 \rightarrow$ almost all discharge comes from Q_{TD}.
- If the value is close to $0 \rightarrow$ almost all discharge comes from Q_{DA}.
- At 0.5 both Q_{TD} and Q_{DA} contribute equally.

The fraction of a branch relative to the total discharge at that moment through both branches can also be an indicator for the partitioning over the bifurcation. The results for this method can be seen in Figures H.3 and H.4.

Time-series of Fractions of instantaneous discharge and sediment load after the bifurcation

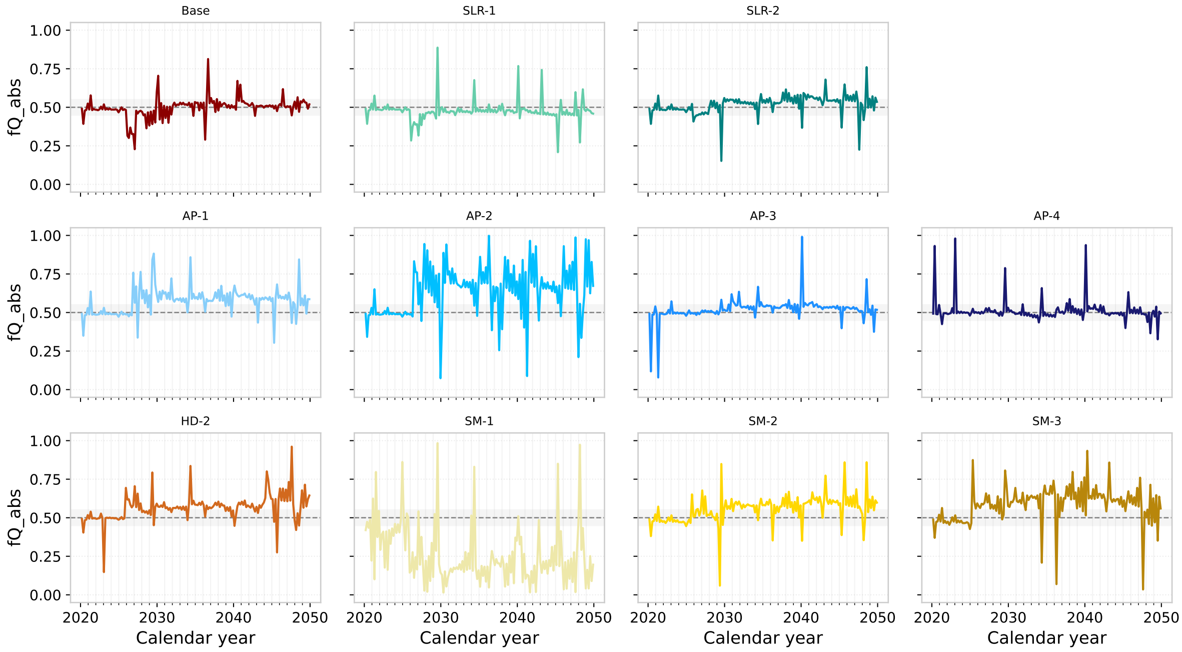

Figure H.3: Fraction of Tran De instantaneous discharge relative to total discharge

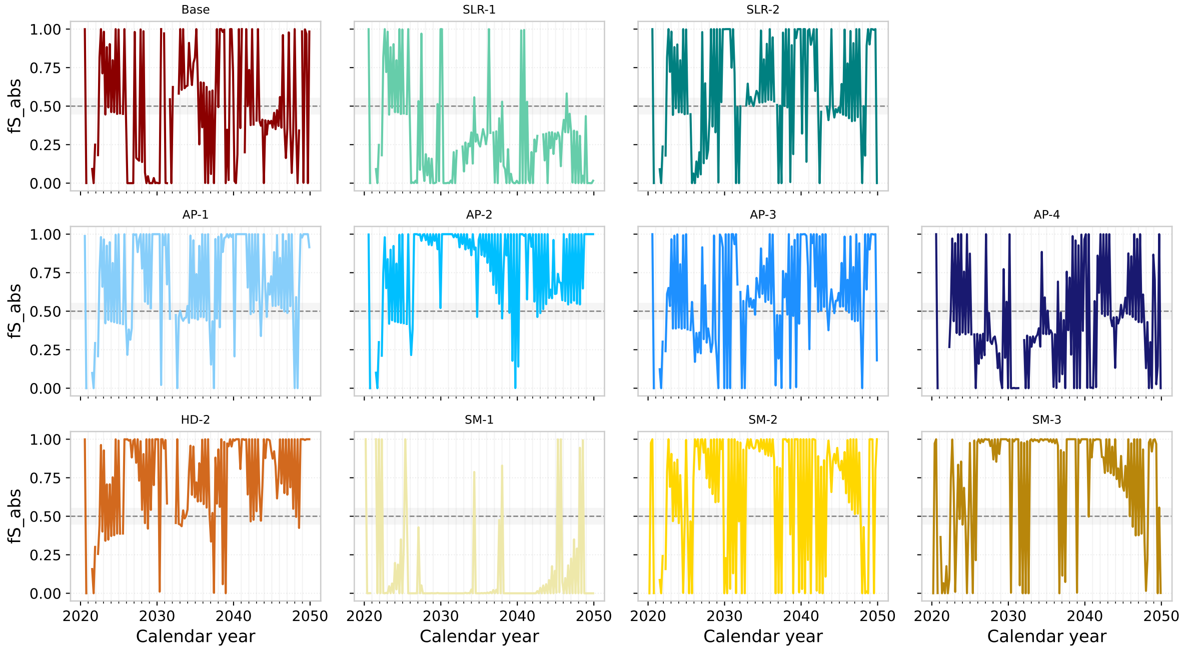

Figure H.4: Fraction of Tran De instantaneous sediment load relative to total sediment load

H.2. Stability bifurcation

H.2.1. Method 1: Normalized Cumulative sediment bias

In order to quantify the long-term routing preference of sediment between the Tran De (TD) and Dinh An (DA) distributary channels, two cumulative quantities over time step i with duration Δt_i (in seconds) are defined. The cumulative difference in sediment load (Eq. H.3) after the bifurcation and the cumulative magnitude of the sediment load (Eq. H.4) are defined.

The Cumulative difference can be defined as follows:

$$\mathrm{cumDiff}_n = \sum_{i=1}^{n} \big(S_{\mathrm{TD},i} - S_{\mathrm{DA},i}\big)\, \Delta t_i, \tag{H.3}$$

where $S_{\mathrm{TD},i}$ and $S_{\mathrm{DA},i}$ denote the instantaneous sediment fluxes into the Tran De and Dinh An branches, respectively.

$$\mathrm{cumMag}_n = \sum_{i=1}^{n} \big(\,|S_{\mathrm{TD},i}| + |S_{\mathrm{DA},i}|\,\big)\, \Delta t_i. \tag{H.4}$$

The Normalized cumulative bias is then defined by dividing the difference by the magnitude, defined as:

$$\mathrm{Bias}_n = \frac{\mathrm{cumDiff}_n}{\mathrm{cumMag}_n} = \frac{\displaystyle\sum_{i=1}^{n} \big(S_{\mathrm{TD},i} - S_{\mathrm{DA},i}\big)\, \Delta t_i}{\displaystyle\sum_{i=1}^{n} \big(|S_{\mathrm{TD},i}| + |S_{\mathrm{DA},i}|\big)\, \Delta t_i}. \tag{H.5}$$

Interpretation:

- $\mathrm{Bias}_n > 0$: cumulative preference toward Tran De.
- $\mathrm{Bias}_n < 0$: cumulative preference toward Dinh An.
- $\mathrm{Bias}_n = 0$: perfectly balanced cumulative routing.

It should be noted that by construction of the normalized cumulative bias ($S_{\mathrm{tot}} = S_{\mathrm{TD}} + S_{\mathrm{DA}}$) the absolute sediment load is not considered but the relative imbalance between the two distributaries.

H.2.2. Method 2: ACF-Method for stability assessment bifurcation

An autocorrelation-based stability assessment of the bifurcation was derived from the temporal dynamics of the symmetry indices. For each scenario, the lag-1 autocorrelation (ρ_1), the integral timescale T_{int}, and the e-folding time T_e from the weekly time series of SI_Q and SI_S were computed. The integral timescale was obtained by summing the autocorrelation function (ACF) across lags until the first zero crossing,

$$T_{\text{int}} = \Delta t \sum_{\tau=1}^{\tau^*} \rho(\tau),$$

where Δt is the sampling interval and τ^* the first non-positive lag. The e-folding time T_e was defined as the lag where the ACF first dropped below $1/e$. In cases where this occurred within the first lag, T_e is undefined and reported as “NaN,” which is interpreted as very fast decay (i.e. stable behaviour).

ACF results

The stability of the sediment and discharge partitioning was evaluated from the temporal autocorrelation of the symmetry indices. The key diagnostic is the integral timescale (T_{int}), which measures how long fluctuations typically remain correlated: short T_{int} values mean quick loss of memory and stable dynamics, while larger T_{int} values indicate that variations last somewhat longer.

Across all scenarios, discharge shows consistently short timescales ($T_{\text{int},Q} \leq 29$ days), confirming that discharge partitioning is stable. Sediment dynamics are slightly more variable: most scenarios give very short timescales ($T_{\text{int},S} \leq 10$ days), while SM-3 shows a somewhat longer response ($T_{\text{int},S} = 42$ days). Overall, these timescales are still small compared to the multi-year simulation, meaning the bifurcation is stable, with only small differences in how long sediment fluctuations last between scenarios.

Table H.1: Autocorrelation-based stability metrics of the bifurcation

	Base	**AP-1**	**AP-2**	**AP-3**	**AP-4**	**HD-2**	**SLR-1**	**SLR-2**	**SM-1**	**SM-2**	**SM-3**
$\rho_{1,Q}$	0.08	0.20	0.12	-0.14	-0.19	0.13	0.09	-0.12	0.16	0.15	0.05
$T_{\text{int},Q}$ (days)	11	19	29	0	0	19	20	0	25	23	29
$T_{e,Q}$ (days)	NaN	NaN	220	NaN	NaN	NaN	NaN	NaN	NaN	NaN	448
$\rho_{1,S}$	0.07	-0.19	-0.04	-0.19	-0.15	0.10	-0.02	-0.02	0.18	0.10	0.27
$T_{\text{int},S}$ (days)	4	0	0	0	0	5	4	4	10	0	42
$T_{e,S}$ (days)	195	895	145	1009	NaN	185	930	980	NaN	1200	1556